Uncertainty in Underwater Acoustic Field Prediction

by

Kevin R. James

A dissertation submitted in partial fulfillment
of the requirements for the degree of
Doctor of Philosophy
(Mechanical Engineering)
in The University of Michigan
2009

Doctoral Committee:

Professor David R. Dowling, Chair
Associate Professor Bogdan Epureanu
Professor Karl Grosh
Associate Professor Divakar Viswanath
Professor Nikolas Vlahopoulos

Table of Contents

List of Figures

Figure

Chapter 1

Introduction

I. Motivation of Research

The accurate prediction of acoustic fields is important in research, as well as commercial and military efforts. For example, Naval sonar applications include detection, localization, tracking, and identification of remote sources, and oceanographic measurements for environmental assessment. The nature of sea water renders useless all terrestrial means for remote sensing except sound. Therefore, an immense amount of research over the past decades has produced robust and successful theories, models, tools, and empirical environmental data for predicting acoustic fields in a wide variety of complex underwater environments. However, rapid means for assessing the uncertainty of acoustic field predictions are lacking. This thesis presents a new and efficient means for acoustic uncertainty assessment in Navy-relevant environments and compares it with traditional and more modern techniques.

Every field prediction requires some modeling of the underwater environment in which the acoustic field is calculated. Advances in propagation simulation techniques have allowed for the accurate predictions of sound fields in environments with range-

dependent features, and even when the ocean's surface, bottom, and/or water column have fluctuating or random parameters. All of these environmental models, however, require environmental data about the ocean. This data is subject to uncertainty not only in local measurements, but in the spatial and temporal variations of parameters far from the measurement point, or long after the data were collected. Thus, all environmental models, and inputs into acoustic propagation calculations, contain a certain amount of uncertainty or error. In essentially all cases, uncertainty in input parameters is the dominant source of error in a predicted underwater sound field, outweighing field model and calculation errors. To illustrate this, consider an idealized 100-m deep sound channel with a free surface, a hard flat bottom, a constant sound speed and a harmonic point source at 500 Hz. Figure 1.1a shows the field amplitude over 15 km, with the cylindrical amplitude decay (proportional to $1/\sqrt{r}$) factored out. Figure 1.1b shows the amplitude error arising from a 1 meter error in the sound channel depth. Even in this ideal sound channel, it is clear that a 1 meter uncertainty in bottom depth produces significant changes to the predicted field that become increasingly more important at longer ranges. (In Figure 1.1, please note the extreme compression of the horizontal axis (range) when compared to the vertical (depth) axis.)

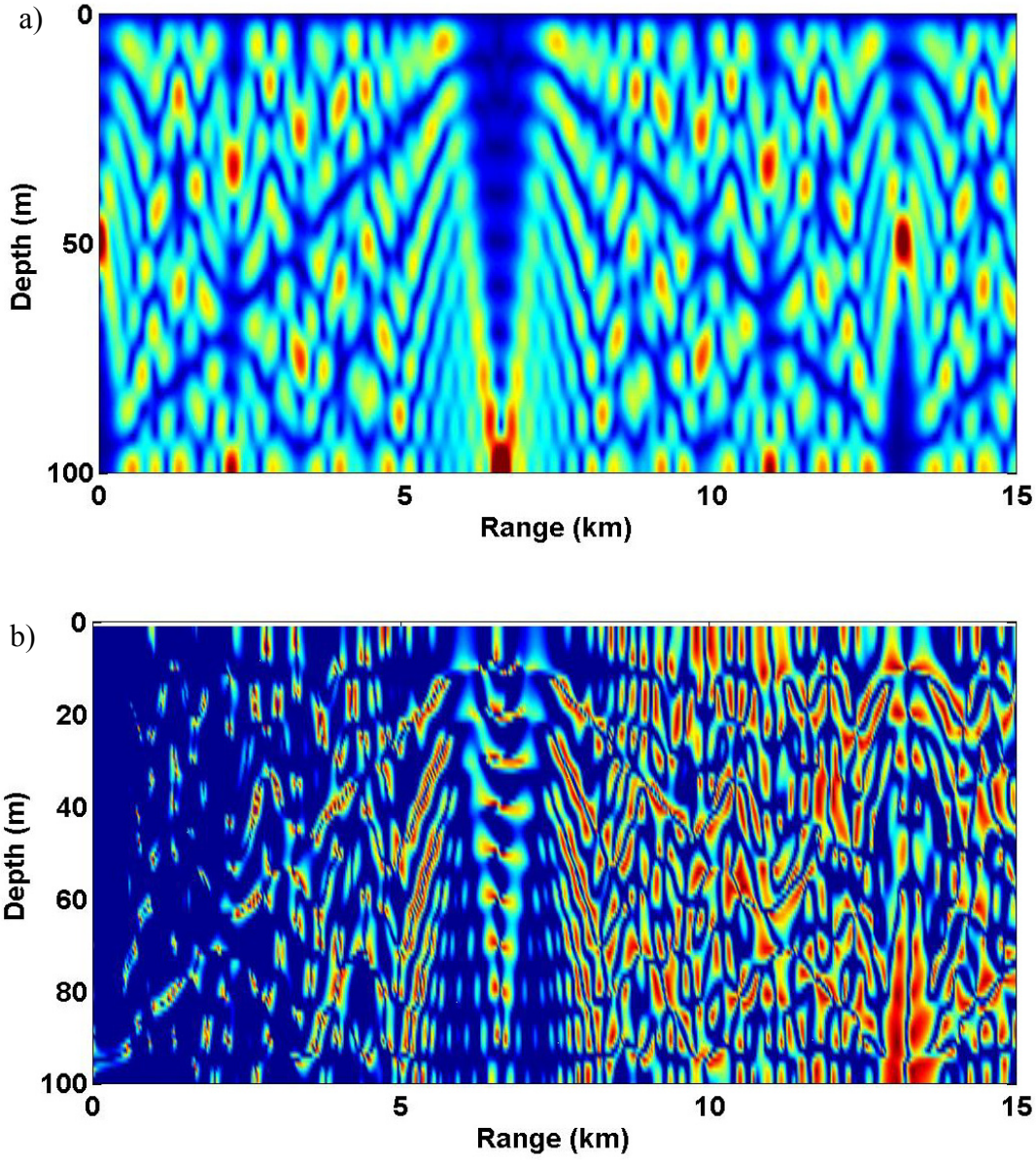

Figure 1.1. Field amplitude (a), and field amplitude error (b) for a 1-m depth error in an ideal sound channel

For standard applications of harmonic acoustic field prediction, a model for acoustic propagation is assumed at the chosen frequency ω, and exact values of all environmental variables are input into the acoustic model, to obtain a complex-valued prediction for the acoustic field at any spatial point. In contrast, the techniques explored in this research treat environmental inputs as random variables, with assumed probability distributions or error bounds. The output of such techniques is a probability distribution for the predicted harmonic acoustic field at any spatial point, rather than a single complex pressure value. Such techniques provide a measurement of accuracy for all applications for which a deterministic field prediction is useful, as well as providing bounds for the possible values of the acoustic field at any point. Broadband acoustic uncertainty calculations for time-dependent waveforms are certainly possible via Fourier superposition of time-harmonic results; however, such broadband uncertainty assessments are beyond the scope of this thesis.

II. Uncertainty and Randomness

It is important to make a distinction between uncertainty in a field calculation, and randomness in the field. Figure 1.2 illustrates the difference in terminology for the case of an underwater sound channel of depth D.

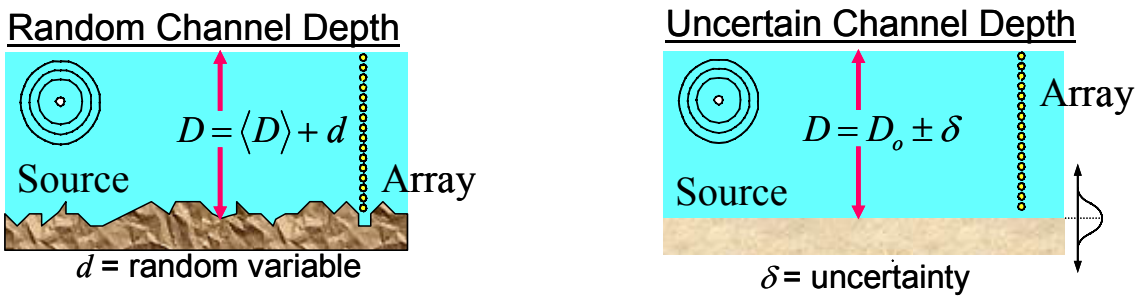

Figure 1.2. Random and uncertain channel depth

For a random channel depth, the local depth varies spatially in an unpredicted manner. This can be incorporated into acoustic prediction models as a roughness parameter for the bottom, or by introducing a random variable d which is added to the mean depth D.

A parameter can be uncertain, however, without exhibiting any spatial or temporal fluctuation. The actual channel depth of the waveguide in Figure 1.2 is a constant value – the uncertainty simply represents the fact that the observer does not know the value of the depth with certainty. As a simple example, this would correspond to the case where the observer knew the channel depth several hours in the past but does not know the progress of the ocean's tides at the location of interest. For the purposes of an acoustic field prediction model for this case, the sound channel bottom can be treated as flat with constant depth, but the uncertainty in depth must somehow be incorporated, and transformed into uncertainty in the predicted harmonic acoustic field.

III. Related Research

While the investigation of uncertainty in acoustic field predictions is a relatively new endeavor, there is much prior work that both motivates the solution and provides

tools to overcome its obstacles. The following is a summary of the existing research in the categories of wave propagation in random media, Probability Density Function methods for turbulent flows, uncertainty in ocean environments, and numerical simulation of uncertainty. This thesis research builds on the successes of all of these fields of inquiry, in order to construct a solution to a problem that none fully address – the prediction of uncertainty in acoustic field calculations.

Wave Propagation in Random Media

The field of wave propagation in random media (WPRM) deals with media having parameters that fluctuate randomly in space and/or time. There is a significant difference between problems involving such "random" variables, which fluctuate over the course of a single calculation, and "uncertain" variables, as discussed above. There are similarities, however, in that both the problems of random and uncertain parameters deal with the propagation of probability in a field, and thus similar tools may be used, with caution.

WPRM is a mature and robust field of research, classic reviews of which can be found in the books by Ishimaru (1978) and Uscinski (1977). Brown (1972) generated partial differential equations for generic moments of a propagating wave distribution. Flatté (1983) outlines advances particular to the field of oceanic acoustics. Successes in WPRM are often limited to specific frequency ranges and media properties, thus the field remains very active today. The journal Waves in Random and Complex Media publishes much of the current research on this and related topics. Recently, Colosi et al. (1999) presented experimental results demonstrating the need for more accurate prediction

techniques for low-frequency acoustic propagation. Kallistratova (2002) provides a review of acoustic propagation research in atmospheric turbulence. This paper outlines the successes based on assumptions of locally homogenous and isotropic turbulence, but highlights the profound effect that departures from this assumption have on acoustic propagation in the real atmosphere.

PDF methods for Turbulent and Reacting Flows

A different approach to the propagation of probability was originally developed in the field of turbulence. Lundgren (1967) introduced a method for developing the governing equations for Probability Density Functions (PDFs) of the variables of interest. Advances in this approach in the area of turbulence over the subsequent four decades are have been summarized by Pope (2004). Many researchers are still expanding on these techniques. Xu and Pope (1999) quantified the accuracy of a PDF/Monte Carlo solution procedure for turbulent reacting flows. Wang et al (2005) applied the PDF technique in conjunction with the most recent physical models for turbulence/radiation interactions in jet flames. Minier and Peirano (2001) applied the PDF method simultaneously to a fluid and particles in turbulent polydispersed two-phase flows. Tsai et al (2002) introduce a finite-mode PDF model for turbulent reacting flows, with results closely matching those of the original PDF method.

While this approach was clearly developed for modeling physical processes in random, not uncertain, media, there is still potential application for acoustic field prediction. By recasting the governing equations of acoustics in terms of PDFs for uncertain variables, governing equations for the propagation of uncertainty PDFs are

obtained. The challenge, however, lies in developing solution techniques and closure models for these equations that do not rely on random behavior of the parameters, as in the field of turbulence. The application of these techniques to acoustic uncertainty prediction is further explored in Chapter 2 of this thesis.

Uncertainty in Ocean Environments and Signal Processing

There is also a growing amount of work in the field of uncertainty in ocean acoustics as a whole. Several researchers have examined the effects of environmental uncertainty on specific underwater sound applications, such as source localization. Shang and Wang (1991) explored the effect of water-depth mismatches on source localization via matched-field processing. Their results showed that the range- and depth-shifting effect of a 3% water-depth mismatch could be adequately predicted analytically in a 100m Pekeris waveguide at 150 Hz. Haralabus et al. (1993) presented an improved algorithm for source localization in acoustic scattering environments, which provides more accurate results with imperfectly known surface statistics than previous methods. Dosso (2003) examined the effect of uncertainties in water depth, sound speed, and bottom characteristics on source localization uncertainties, using Bayesian inference theory. Wang et. al (2004) provide computational examples of the relationship between sensor network topology and localization uncertainty, outlining a method for obtaining a lower bound for the localization error. These papers deal with uncertainty in a specific decision aid developed from acoustic predictions – source localization. While some success is made in predicting bounds for the uncertainty in the outcome, and predicting

the most likely source location taking environmental uncertainties into account, there is no attempt to address the problem of uncertainty in the predicted acoustic field in general.

Other researches have focused on uncertainty only in source detection. Sha and Nolte (2005) show that the optimal sonar detection performance in diffuse noise depends primarily on environmental uncertainties and the signal-to-noise ratio at the receivers. An analytic approximation for detection performance is provided which accounts for environmental uncertainties. Stone and Osborn (2004) incorporate environmental uncertainty in a tracking and detection algorithm, in order to obtain meaningful results even in the presence of large prediction errors. Sibul et. al (2004) use a maximum entropy method to calculate confidence intervals for detection of a high frequency, narrow-band source in an uncertain environment. As with the research on source localization, the work done in detection in uncertain environments may provide guidance for obtaining predictions of the uncertainty in the acoustic field, but does not address the problem directly.

Some researchers, however, are working on the problem of uncertainty in acoustic field propagation using different methods than those outlined in this thesis. Creamer (2006) describes environmental variability in terms of a spectral representation of stochastic processes. Finette (2005, 2006) applies this technique, referred to as Polynomial Chaos Expansion (PCE), to an isospeed waveguide governed by the narrow-angle parabolic equation. These papers address the same general problem of acoustic uncertainty prediction as outlined above, but with a significantly different approach than the field-shifting technique that is described in Chapter 3 of this thesis. However, for completeness, Chapter 4 of this thesis presents the application of polynomial chaos

expansion to a Pekeris waveguide, and compares this technique to the field shifting method.

Numerical Simulation of Uncertainty

Finally, others have addressed the problem of uncertainty with the brute force of repeated numerical calculations that evenly sample the entire space spanned by the uncertain variables, herein referred to as Direct Simulations (DS). This approach is sometimes made more efficient via random sub-sampling of the space spanned by the uncertain variables, a technique commonly referred to as Monte-Carlo calculation. Shorey et al (1994) used Monte-Carlo methods to provide an upper bound on source localization performance in the presence of environmental uncertainty. Gerstoft and Mecklenbräuker (1998) use a directed Monte-Carlo method to provide distributions for estimated ocean parameters. Direct simulations or Monte-Carlo techniques also offer an excellent standard for comparisons, as shown in several of the papers reviewed in previous sections. While these techniques can be used effectively for certain tasks, a goal of this research is to obtain predictions with acceptably similar accuracy to direct simulations or Monte-Carlo methods, for a drastically reduced computational cost, allowing for real-time prediction of uncertainty.

IV. Underwater Acoustic Field Calculation

This section summarizes the basic concepts behind the deterministic calculation of acoustic fields, which is the foundation for the uncertainty prediction techniques explored in this research. For many applications, underwater acoustic propagation along

an azimuth of interest can be considered two-dimensional with range, r, and depth, z, coordinates with local cylindrical symmetry. An underwater sound channel, or waveguide, refers to a two-dimensional slice of the field, varying over range and depth. All underwater sound channels investigated in this research exhibit the basic structure shown in Figure 1.3, with simplifications for some cases.

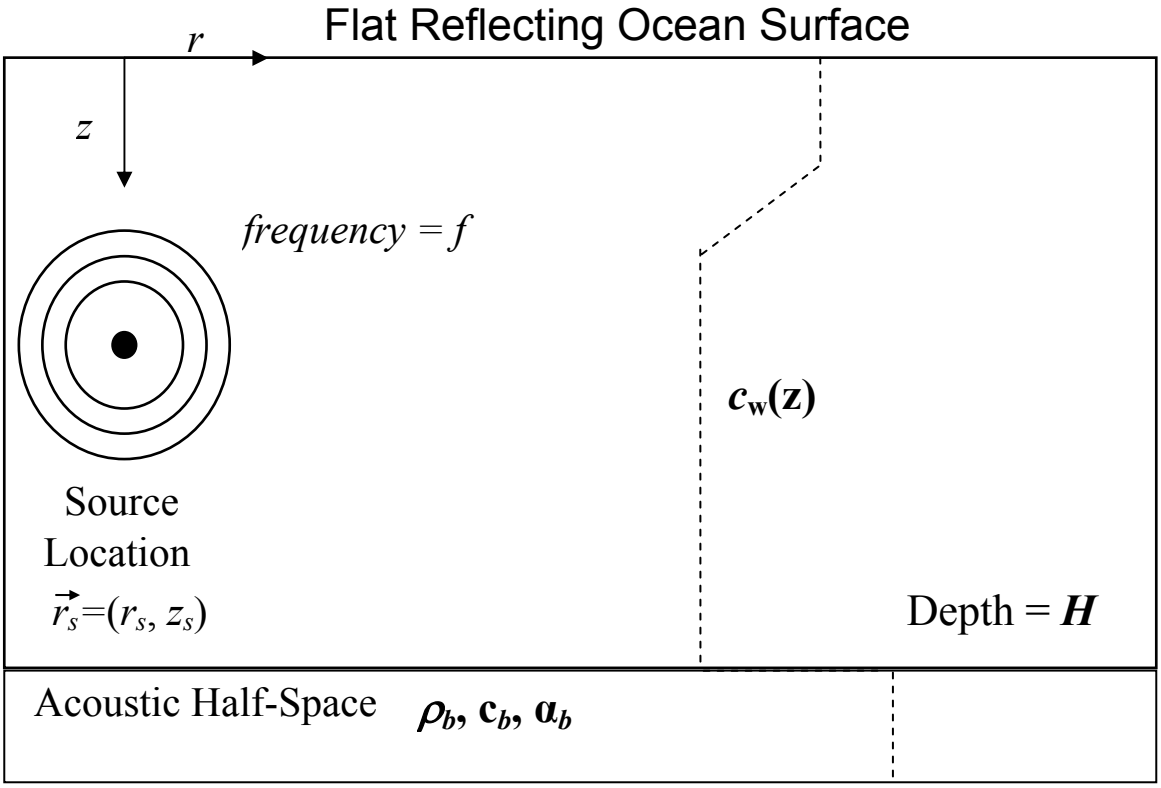

Figure 1.3. A generic underwater sound channel

The surface of the water is assumed flat and perfectly reflecting. The water column is assumed to have a sound speed c_w which may vary with depth, but is independent of range. The bottom interface is located at a depth H below the surface. The bottom is modeled as a half-space of infinite depth, with its own sound speed c_b, an

absorption parameter α_b, and a density ρ_b relative to the ocean density. An acoustic source of cyclic frequency $\omega = 2\pi f$ is located at r_s, z_s.

The acoustic pressure field *P(r,z)* is governed by the Helmholtz equation

$$\left[\frac{1}{r}\frac{\partial}{\partial r}\left(r\frac{\partial}{\partial r}\right)+\frac{\partial^2}{\partial z^2}+k^2\right]P(r,z)=0\,, \tag{1}$$

where the wavenumber k is defined by

$$k=\frac{2\pi f}{c(z)}=\frac{\omega}{c(z)}. \tag{2}$$

In the far field, solutions to the Helmholtz equation can be represented as sums over modes of the form

$$P(r,z)=\sqrt{\frac{2\pi}{r}}e^{-i\frac{\pi}{4}}\sum_{m=1}^{M}\varphi_m(z)\varphi_m(z_s)e^{ik_m r}\,. \tag{3}$$

Here, k_m is a modal wavenumber corresponding to the mth mode, and $\varphi_m(z)$ is the mode shape for that mode. The modal sum must be terminated at some finite mode number M. At far ranges this M is often chosen as the number of so-called "trapped" or "propagating" modes – modes which are fully internally reflected at the bottom interface – as modes of higher order lose their energy rapidly in the bottom. However, M can be chosen at a higher value to incorporate the so-called "leaky" modes, which can still contribute significantly to the pressure field in some environments, especially at short ranges.

It is worth noting that for a modal sum solution technique, calculating the mode shapes and modal wavenumbers allows the pressure at any point in the field to be obtained from a simple summation. Thus, the majority of analytical or computational effort in a modal solution is in obtaining the appropriate wavenumbers and mode shapes.

The above solution assumes that the values of all parameters in Figure 1.3 are known exactly. In practical applications, values for these parameters will only be known to within some specified bounds. Because the relationship between each parameter and the field solution is complicated and nonlinear, it is not transparent how uncertainty in the environmental inputs affects the uncertainty of the final field solution. This lack of transparency in the parameter-field coupling highlights the need for accurate and efficient approximations for the relationship between environmental and field uncertainties.

V. Overview of uncertainty approximation techniques

In this research, four different methods of predicting the uncertainty in an acoustic field arising from uncertain values of environmental inputs are discussed. The first and most straightforward technique is referred to as Direct Simulation (DS). For direct simulation, if the depth is uncertain, the field calculation can simply be performed at many different depth values, over the full range of possible depths. Allowing for an arbitrarily large number of calculations, this technique yields an accurate relationship between acoustic pressure and depth. With the relationship between the pressure and the uncertain depth known, the probability distribution for an uncertain depth can be transformed to a distribution for the pressure through standard techniques. Assuming infinite computational time were available, this technique would represent the complete solution for uncertainty prediction, as the accuracy can be made arbitrarily high with more computations. In practice, field predictions in realistic ocean environments can be computationally expensive, and direct simulation at an acceptable level of accuracy is seldom feasible in real time. Nevertheless, direct simulation is useful as a research tool

because it provides a reference for all other uncertainty assessment techniques. With a sufficient number of field calculations, the distributions generated by direct simulation can be considered exact, for the purposes of determining the approximation errors of other techniques. Closely related to direct simulation are Monte-Carlo techniques. A Monte-Carlo approximation is essentially a direct simulation, where the input states are chosen randomly according to their distributions, instead of uniformly across all possible values of the inputs. This provides an approximation for the probability distribution of the field directly, but does not predict the relationship between the field and its uncertain inputs. Especially in cases involving several uncertain variables, Monte Carlo sampling can drastically reduce the number of field calculations required to obtain the desired level of accuracy, but the number is still many orders of magnitude larger than at least one of the uncertainty approximation techniques discussed below.

The second technique for determining acoustic uncertainty is referred to as PDF propagation. In standard acoustic prediction, the deterministic pressure at the source propagates to the point of interest and the propagation is governed by the Helmholtz equation. In this technique, the pressure at any point is described not as a single value, but by a Probability Density Function (PDF), representing its uncertainty. The governing equation for the field, as well as the boundary and initial conditions, are applied to the PDF, rather than the deterministic pressure. If the resulting differential equations can be solved for a particular sound channel, the uncertain distribution of pressure is known at all locations. The successes and limitations of this technique are explored in James and Dowling (2005), provided herein as Chapter 2.

The third technique is referred to henceforth as Field Shifting (FS). This technique exploits a property exhibited by many underwater sound channels, that small changes in an environmental parameter approximately correspond to small spatial shifts of the field, on a local scale. Thus, the pressure at a point in the field, at different possible values for an uncertain input, can be mapped to the pressure at nearby points in the field. As discussed for direct simulation, once the relationship between pressure and an uncertain variable is determined, the uncertain pressure distribution can be obtained from the distribution of the uncertain input through standard PDF transformation or Monte-Carlo sampling techniques. The formulation and accuracy of this technique are explored in James and Dowling (2008), provided herein as Chapter 3.

The final technique, polynomial chaos expansion, was not developed through this research, but is a technique utilized in several fields of engineering (Field, 2004), such as fluid modeling (Xiu et al., 2002b) and advection/diffusion (Witteveen and Hester, 2008). The polynomial chaos method was first applied to underwater acoustics by Dr. Steve Finette of the Naval Research Laboratory (see Finette 2005, 2006) as discussed above. For this technique, the uncertain pressure is represented as an expansion of known basis functions and unknown uncertainty coefficients, which are calculated for the sound channel of interest. Chapter 4 describes how this technique can be used in a simple range-independent sound channel, and compares the accuracy and efficiency of the PCE technique to field shifting,and direct simulations.

Chapter 2

PDF Propagation

Abstract

Acoustic field predictions, whether analytical or computational, rely on knowledge of the environmental, boundary, and initial conditions. When knowledge of these conditions is uncertain, acoustic field predictions will also be uncertain, even if the techniques for field prediction are perfect. Quantifying acoustic field uncertainty is important for applications that require accurate field amplitude and phase predictions, like matched-field techniques for sonar, non-destructive evaluation, bio-medical ultrasound, and atmospheric remote sensing. Drawing on prior turbulence research, this paper describes how an evolution equation for the probability density function (PDF) of the predicted acoustic field can be derived and used to quantify predicted-acoustic-field

The following chapter was published in 2005 in the Journal of the Acoustical Society of America, Volume 118, pages 2802-2810, with the title "A probability density function method for acoustic field uncertainty analysis."

uncertainties arising from uncertain environmental, boundary, or initial conditions. Example calculations are presented in one and two spatial dimensions for the one-point PDF for the real and imaginary parts of a harmonic field, and show that predicted field uncertainty increases with increasing range and frequency. In particular, at 500 Hz in an ideal 100-m-deep underwater sound channel with a 1-m root-mean-square depth uncertainty, the PDF results presented here indicate that at a range of 5 km, all phases and a 10 dB range of amplitudes will have non-negligible probability. Evolution equations for the two-point PDF are also derived.

I. Introduction

Acoustic predictions can be made using either analytical or numerical means, with the latter continually allowing more complicated environments and geometries to be tackled (see Jensen et al. 1994 for examples in underwater acoustics). However, even if perfect analytical or numerical techniques are used, or model and numerical errors are negligible, the accuracy of either analytic or numerical acoustic field predictions will be limited if the parameters describing the acoustic environment and the boundary or initial conditions used in the solution technique are uncertain. The effects that uncertain environmental, boundary, or initial conditions (hereafter referred to as input parameter uncertainties) have on predicted acoustic fields is not readily ascertained from the field prediction technique itself, and may depend in a complicated and nonlinear manner on the particular input parameters involved.

Quantifying the uncertainty in predicted acoustic fields produced by input parameter uncertainties is potentially important for any application of acoustics that relies on a field

model to generate predictions. Such applications include matched-field techniques in sonar, non-destructive evaluation, bio-medical ultrasound, acoustic holography, and atmospheric and other types of remote sensing. In these applications, mismatch between actual acoustic propagation and predicted acoustic propagation may lead to erroneous results. Plus, recent studies (Sha and Nolte 2005a,b) have determined that sonar detection performance is degraded in uncertain environments. Given the accuracy of modern computational techniques, predicted-field uncertainty may dominate other sources of uncertainty, especially at higher frequencies and longer source-receiver ranges where input parameter uncertainties cause greater predicted-field uncertainties. Thus, an underlying assumption made here is that the interested acoustician has a means for predicting acoustic fields but may not have any means to assess the uncertainty of the predicted fields.

The primary purpose of this paper is to present a potentially useful means for quantifying predicted-field uncertainty arising from input parameter uncertainties. Here, uncertainty is quantified in terms of a probability density function (PDF), and this PDF's evolution equation is derived using mathematical identities developed from the relevant fine-grained PDF (Lundgren 1967) and wave mechanics, in a manner similar to that developed for the study of turbulence (see Pope 2000). This PDF approach is new to acoustics and the examples presented here are meant to be illustrative, not exhaustive. Indeed, analyzing predicted-field uncertainty via PDFs is potentially challenging because the relationship between uncertain-input-parameter PDFs and the predicted-field PDFs may be complicated and nonlinear. Furthermore, the additional and possibly difficult task of determining *a priori* input-parameter PDFs is not addressed here. Thus, future

investigations that surpass the one reported here will be necessary to determine the ultimate utility of these PDF techniques for quantifying predicted acoustic-field uncertainty.

The material presented here is a new application of the PDF transport formalism developed for turbulence and turbulent combustion. However, fundamental differences exist between turbulence PDFs and those in acoustic uncertainty analysis. For example, the turbulent-velocity-fluctuation PDF is intended to statistically describe actual fluid velocity fluctuations. Hence, its form is constrained or limited by the nonlinear physical conservation laws for mass, momentum, and energy. In acoustic uncertainty analysis, the pressure-field PDF is intended to statistically describe the possible acoustic pressure fields that might arise from a set of input parameter uncertainties. In the acoustic case, each possible field obeys linearized versions of the conservation laws, but the input parameter uncertainties themselves are not constrained by conservation laws or other physical limits. Therefore, acoustic-field-uncertainty PDFs are inherently less constrained than turbulence PDFs. Although this may mean that acoustic-field-uncertainty PDFs will be even more elusive than turbulence PDFs, the prospects for developing effective PDF prediction techniques for acoustics might actually be better than that for turbulence because the underlying phenomena in the acoustic case are linear while turbulence is inherently nonlinear.

For the present discussion, random and uncertain acoustic environments are not the same. The goal of the research effort presented here is to quantify acoustic field uncertainties in primarily deterministic environments where one (or perhaps a few) input parameter(s) is (are) uncertain. To this end, one- and two-dimensional cases of ideal

range-independent sound channels, each with a single uncertain scalar parameter, are presented in Sections II and III. Acoustic propagation in random environments is different because it is likely to require many uncertain input parameters. Consider a random-depth range-dependent sound channel with constant average depth. Here, a randomly rough bottom with a finite horizontal correlation length would necessitate the inclusion of an uncertain parameter (depth, slope, etc.) for each range increment – for example, a roughness correlation length – between the source and receiver. Thus, this situation could entail many uncertain input parameters at long ranges. For comparison, the example in Section III involves a sound channel with a constant range-independent depth that is uncertain, a situation described by a single random variable for any source-receiver range.

Wave propagation in random media is commonly analyzed via moments of the acoustic (or electromagnetic) field and an extensive literature exists for field-moment equations for random media (see Uscinski 1977, Ishimaru 1978). It is conjectured that the PDF methods presented here can be formally connected to these established results when the uncertain input parameters are sufficiently numerous and appropriately distributed in space, and moments are extracted from the appropriate PDF evolution equation. However, proof of this conjecture is beyond the scope of this paper.

At least two other means for quantifying predicted-field acoustic uncertainty and its impact on signal processing have recently been reported. Sibul et al. (2004), using maximum entropy methods, discusses how randomness and uncertainty in the environmental, boundary, and source parameters affects the probability of detection of a narrowband sound source. Finette (2005) describes how uncertainty can be imbedded

into ocean acoustic propagation models through expansions of the input parameter uncertainties in orthogonal polynomials. Both of these techniques, and the one described in this paper, hold the promise of significant computational efficiency compared to Monte-Carlo simulations, the common and robust but computationally expensive means for assessing field statistics in uncertain or random media.

For simplicity, this paper only addresses the PDF equations for time harmonic fields at radian frequency ω. Thus, two probability variables must be considered, R and I, the real and imaginary parts of the predicted acoustic field, or A and Θ, the amplitude and phase of the predicted acoustic field. Here the former are emphasized over the later. An advantage of this PDF formulation of the predicted-field uncertainty is that a PDF carries more information than its first few moments alone. This advantage is particularly important because the PDF of R and I may depart drastically from joint-Gaussian even when the input parameter uncertainty is Gaussian distributed. Extension of this effort to broadband time-dependent pressure fields is possible but is not pursued here.

The remainder of this paper is divided into four sections. The next section presents the development of the predicted-field PDF transport equation in one spatial dimension. This equation is then solved for the case of uncertain wave number or sound speed. The third section extends the development to two spatial dimensions and a numerical solution for an ideal waveguide with uncertain depth is presented. The fourth section shows how the techniques presented in the first two sections can be extended to derive an equation for the two-point predicted-field PDF. The final section summarizes this effort, presents its conclusions, and describes possible extensions of this work.

II. PDF Uncertainty Analysis in One Spatial Dimension

The purpose of this section is to illustrate how an evolution equation for the PDF of a predicted acoustic field can be obtained from the fine-grained PDF (Lundgren, 1967) and one-dimensional wave propagation relationships for harmonic waves. The resulting equation is then solved by direct analytical means for the acoustic waves propagating in an ideal duct with uncertain wave number (or sound speed). Here, pressure has a harmonic time dependence with radian frequency ω, $p(x,t) = \mathrm{Re}\{\hat{p}(x)e^{-i\omega t}\}$ where $\hat{p}(x) = p_R(x) + ip_I(x)$, and x is the spatial coordinate. The PDF of interest is the one-point, joint PDF for the real and imaginary parts of the pressure, $f_P(R,I;x)$, where R and I are the probability sample space variables for the real and imaginary parts of the pressure. Throughout this paper the letter f with subscripts will denote a PDF. Capital-letter arguments will refer to probability space variables and lowercase-letter arguments will refer to field variables, spatial coordinates, or other parameters.

The evolution equation for $f_P(R,I;x)$ can be obtained by manipulating its fine-grained PDF, $\not{f}_P$, a function that can be thought of as a single realization in the infinite ensemble of trials represented by $f_P(R,I;x)$ (Lundgren, 1967). In this paper, and in PDF transport work in turbulence (Pope 2001) and turbulent combustion (Dopazo 1994), the fine-grain PDF plays the role of a generating function that can be transformed into $f_P(R,I;x)$ by computing its expected value. Here, the fine-grain PDF is written explicitly as a product of Dirac delta-functions,

$$\not{f}_P = \delta(p_R - R)\delta(p_I - I), \tag{1}$$

and its expected value, denoted $\langle \not{f}_P \rangle$, is

$$\left\langle \mathcal{f}_P \right\rangle = \int_{-\infty}^{+\infty}\int_{-\infty}^{+\infty} \delta\left(\tilde{R}-R\right)\delta\left(\tilde{I}-I\right) f_P\left(\tilde{R},\tilde{I};x\right) d\tilde{R}d\tilde{I} = f_P\left(R,I;x\right) . \qquad (2)$$

The properties of the fine-grained PDF and the structure of its arguments allow it to be the basis for constructing mathematical identities involving its derivatives with respect to the independent spatial and probability-space variables. These identities for $\mathcal{f}_P$ can be converted to identities for $f_P\left(R,I;x\right)$ by computing an expected value. Then, substitution for the pressure-field derivatives appearing in the identity for $f_P\left(R,I;x\right)$ from established wave-physics relationships produces an evolution equation for $f_P\left(R,I;x\right)$. This procedure is illustrated in the next few paragraphs of this section, and in the first few paragraphs of Sections III and IV.

An important identity for the fine-grained PDF can be derived from Bayes' theorem for any function or variable *b* with probability space variable *B*:

$$\left\langle b\mathcal{f}_P \right\rangle = \int_{-\infty}^{+\infty}\int_{-\infty}^{+\infty}\int_{-\infty}^{+\infty} B\,\delta\left(\tilde{R}-R\right)\delta\left(\tilde{I}-I\right) f_{BP}\left(B,\tilde{R},\tilde{I}\right) dB d\tilde{R}d\tilde{I} = \int_{-\infty}^{+\infty} B f_{BP}\left(B,R,I\right) dB$$

$$= f_P\left(R,I\right)\int_{-\infty}^{+\infty} B\,\frac{f_{BP}\left(B,R,I\right)}{f_P\left(R,I\right)}\,dB = f_P\left(R,I\right)\int_{-\infty}^{+\infty} B f_{B|P}\left(B|R,I\right) dB = f_P\left(R,I\right)\left\langle B|R,I\right\rangle \qquad (3)$$

(see Pope 2000) where f_{BP} is the joint PDF of *B*, *R*, and *I*, and $f_{B|P}$ is the conditional PDF for *B* given values of *R* and *I*. Here the vertical bar denotes conditioning, i.e. $\left\langle B|R,I\right\rangle$ is the expected value of *B* given the information $p_R = R$ and $p_I = I$. This use of Bayes' theorem involves the higher-level distributions $f_{BP}\left(B,R,I\right)$ and $f_{B|P}\left(B|R,I\right)$, which may not be available in general. However, construction of these distributions and/or their moments may be possible when an analytical field model exists, as is shown in the remainder of this section. Alternatively, models for the requisite conditional

moment $\langle B|R,I\rangle$ may be developed directly as is done in PDF work in turbulence (Pope 2000, Lou and Miller 2001, Waclawczyk et al. 2004) and turbulent combustion (Dopazo 1994, Pope 2004, James et al. 2005). A general means for determining $f_{BP}(B,R,I)$ or its moments is beyond the scope of this paper.

For acoustic field uncertainty analysis, the most important relationships that can be obtained from the fine-grained PDF involve spatial derivatives. For example, partial differentiation with respect to the independent spatial variable *x* produces

$$\frac{\partial \mathcal{f}_P}{\partial x} = \delta'(p_R - R)\frac{\partial p_R}{\partial x}\delta(p_I - I) + \delta(p_R - R)\delta'(p_I - I)\frac{\partial p_I}{\partial x} = -\frac{\partial \mathcal{f}_P}{\partial R}\frac{\partial p_R}{\partial x} - \frac{\partial \mathcal{f}_P}{\partial I}\frac{\partial p_I}{\partial x}\ , \qquad (4)$$

an identity for $\mathcal{f}_P$. Here the prime denotes differentiation with respect to the argument. Taking the expected value of Eq. (4) and using Eq. (3) produces an identity for $f_P(R,I;x)$:

$$\left\langle \frac{\partial \mathcal{f}_P}{\partial x} \right\rangle = \frac{\partial f_P}{\partial x} = \left\langle -\frac{\partial \mathcal{f}_P}{\partial R}\frac{\partial p_R}{\partial x} - \frac{\partial \mathcal{f}_P}{\partial I}\frac{\partial p_I}{\partial x} \right\rangle$$

$$= -\frac{\partial}{\partial R}\left\langle \mathcal{f}_P \frac{\partial p_R}{\partial x} \right\rangle - \frac{\partial}{\partial I}\left\langle \mathcal{f}_P \frac{\partial p_I}{\partial x} \right\rangle = -\frac{\partial}{\partial R}\left(f_P \left\langle \frac{\partial p_R}{\partial x}\middle| R,I \right\rangle \right) - \frac{\partial}{\partial I}\left(f_P \left\langle \frac{\partial p_I}{\partial x}\middle| R,I \right\rangle \right). \qquad (5)$$

This identity can be converted into an evolution equation for $f_P(R,I;x)$ by introducing wave-propagation physics through the pressure derivatives. Here, unidirectional plane-wave [$\hat{p}(x) \propto e^{+ikx}$] propagation relationships are used: $\partial p_R/\partial x = -kp_I$ and $\partial p_I/\partial x = +kp_R$, where $k = \omega/c$ is an uncertain wave number based on the uncertain speed of sound *c*. These relationships allow the conditional moments in Eq. (5) to be rewritten, $\langle \partial p_R/\partial x|R,I\rangle = \langle -kp_I|R,I\rangle = -I\langle k|R,I\rangle$ and $\langle \partial p_I/\partial x|R,I\rangle = \langle +kp_R|R,I\rangle = R\langle k|R,I\rangle$, so it is converted into an evolution equation for $f_P(R,I;x)$:

$$\frac{\partial f_P}{\partial x} = I\frac{\partial}{\partial R}\left(f_P\left\langle k\middle|R,I\right\rangle\right) - R\frac{\partial}{\partial I}\left(f_P\left\langle k\middle|R,I\right\rangle\right). \tag{6}$$

The remainder of this section presents a solution of Eq. (6) for the simple case of an acoustic source with uncertain amplitude and zero phase at $x = 0$ that radiates plane waves in the positive x-direction along an ideal constant-cross-sectional area duct having a uniform but uncertain speed of sound. The first step is to rewrite the derivatives in Eq. (6) in terms of amplitude, $A = \sqrt{R^2 + I^2}$, and phase Θ ($\tan\Theta = I/R$) using $\partial/\partial R = (R/A)\partial/\partial A - \left(I/A^2\right)\partial/\partial\Theta$ and $\partial/\partial I = (I/A)\partial/\partial A + \left(R/A^2\right)\partial/\partial\Theta$ to find:

$$\frac{\partial f_P}{\partial x} = -\frac{\partial}{\partial\Theta}\left(f_P\left\langle k\middle|R,I\right\rangle\right). \tag{7}$$

For a known input frequency, ω, the solution for $f_P(R,I;x)$ can be obtained in terms of the *a priori* PDFs for the uncertain wave number $f_K(K)$ and the uncertain amplitude $f_A(A)$. The initial condition on f_P is:

$$f_P(x=0) = \frac{1}{A} f_A(A)\delta(\Theta); \tag{8}$$

the factor of $1/A$ in Eq. (8) ensures the normalization: $\int\int f_P(x=0)AdAd\Theta = 1$.

The primary difficulty in solving Eq. (7) comes from relating the conditional expectation $\left\langle k\middle|R,I\right\rangle$ to the other independent or dependent variables. For this simple case, $\left\langle k\middle|R,I\right\rangle$ can be determined analytically in terms of Θ, x, and $f_K(K)$. Here, phases between 0 and $+2\pi$ are considered, and the range of the arctangent is set to $[0,\pi]$. The relationship between wave number and phase is thus

$$\Theta = \begin{Bmatrix} \tan^{-1}(I/R) & \text{for } I > 0 \\ \tan^{-1}(I/R) + \pi & \text{for } I < 0 \end{Bmatrix} = \text{mod}(kx, 2\pi) \tag{9}$$

Thus, for a given R and I, k must take one of the discrete values:

$$K_n = \frac{\Theta - 2\pi n}{x}\ ,\ n = 0, \pm 1, \pm 2, \ldots \tag{10}$$

so the conditional PDF of k, $f_{K|P}$, is a sum of δ-functions appropriately weighted by $f_K(K)$:

$$f_{K|P}(K|R,I) = \frac{\sum_n \delta(K - K_n) f_K(K_n)}{\sum_n f_K(K_n)}\ , \tag{11}$$

where the denominator factor merely provides the requisite normalization. The conditional expectation in Eq. (7) can be evaluated in terms of K_n and f_K using Eq. (11):

$$\langle k|R,I\rangle = \int_{-\infty}^{+\infty} K f_{K|P}(K|R,I)\,dK = \frac{\sum_n K_n f_K(K_n)}{\sum_n f_K(K_n)} \tag{12}$$

Formally, the summation is over all possible n; however, only a finite number of the K_n occur where f_K is nonzero and this set of n is used in the summations.

The form of Eq. (12), with K_n providing the dominant combination of the independent variables x and Θ, motivates a solution to Eq. (7) based on the K_n as separate variables:

$$f_P = g(A,x)\sum_n h(K_n)\ . \tag{13}$$

Here, g and h are unknown functions, and, as a recap: $A = \sqrt{R^2 + I^2}$ is the pressure field amplitude, x is the lone spatial coordinate, and K_n is the n^{th} possible wave number value at location x for a given value of R and I. Using Eqs. (12) and (13), Eq. (7) becomes

$$\frac{\partial g}{\partial x}\sum_n h - \frac{g}{x}\sum_n K_n h' = -g\frac{\partial}{\partial \Theta}\left(\langle k|R,I\rangle \sum_n h\right) = -\frac{g}{x}\frac{\partial}{\partial K_n}\left(\langle k|R,I\rangle \sum_n h\right), \tag{14}$$

where derivative relationships, $\partial K_n/\partial x = -K_n/x$ and $\partial K_n/\partial \Theta = -1/x$, from Eq. (10) have been used as well. In Eq. (14), the unspecified dependence of $\langle k|R,I\rangle$ and the argument of h are both K_n, and $\partial/\partial K_n$ implies term by term differentiation of the sums that form $\langle k|R,I\rangle \sum_n h$. The two ends of Eq. (14) can be used to find:

$$-\frac{x}{g}\frac{\partial g}{\partial x} = \left[\frac{\partial}{\partial K_n}\left(\langle k|R,I\rangle \sum_n h\right) - \sum_n K_n h'\right] \Big/ \sum_n h \tag{15}$$

The left side of Eq. (15) depends only on A and x, while the right side depends only on K_n. Thus, both sides must equal a constant yielding two equations:

$$-\frac{x}{g}\frac{\partial g}{\partial x} = \alpha, \text{ and } \; 1 + \left[\frac{\partial}{\partial K_n}\left(\langle k|R,I\rangle \sum_n h - \sum_n K_n h\right)\right] \Big/ \sum_n h = \alpha, \tag{16),(17}$$

where α is the separation constant, and the derivative relationship $(\partial/\partial K_n)(\Sigma K_n h) = \Sigma K_n h' + \Sigma h$ has been used to expand the K_n-derivative in Eq. (15) to fill the [,]-brackets. Equations (12) and (17) produce an equation for h:

$$\frac{\partial}{\partial K_n}\left(\frac{\Sigma K_n f_K}{\Sigma f_K}\Sigma h - \Sigma K_n h\right) = (\alpha - 1)\Sigma h, \tag{18}$$

where the n-designation has been dropped from the summations to save space. The value of α can be determined by considering the form of the solution for x approaching zero. Here, the pressure PDF must match the conditions at the source where the phase is deterministic. Thus, as $x \to 0$ only one value of n can contribute to the various sums, so the terms in parentheses in Eq. (18) become: $\frac{K_n f_K}{f_K} h - K_n h = 0$ which means that $\alpha = 1$, and more generally that:

$$\Sigma K_n f_K \Sigma h - \Sigma K_n h \Sigma f_K = 0, \tag{19}$$

which is solved by simply setting $h = f_K$. Returning to Eq. (16), α = 1 implies $\partial g/\partial x = -g/x$, which has the simple solution $g(A,x) = \tilde{g}(A)/x$ where $\tilde{g}$ is an undetermined function of A alone.

Thus, the solution for the pressure field PDF is

$$f_P = \frac{\tilde{g}(A)}{x} \sum_n f_K\left(\frac{\Theta - 2\pi n}{x}\right) \tag{20}$$

Applying the initial condition, Eq. (8), while recognizing that for any distribution f_K that goes to zero when its argument goes to infinity,

$$\lim_{x\to 0}\left\{\frac{1}{x}\sum_n f_K\left(\frac{\Theta - 2\pi n}{x}\right)\right\} = \delta(\Theta)\,, \tag{21}$$

allows the identification $\tilde{g} = f_A/A$, so that the final solution for this example is:

$$f_p(R,I;x) = \frac{f_A\left(\sqrt{R^2+I^2}\right)}{x\sqrt{R^2+I^2}} \sum_n f_K\left(\frac{\tan^{-1}(I/R) - 2\pi n}{x}\right) \quad \text{for } I > 0 \tag{22}$$

where $2\pi n$ in the argument of f_K should be replaced by $2\pi(n+1/2)$ when $I < 0$.

The evolution of f_P based on Eq. (22) for increasing x is shown in the four parts of Figure 2.1 for known amplitude A_o, i.e. $f_A(A) = \delta(A - A_o)$, and Gaussian wave number distribution centered on $2\pi/\lambda$ with a standard deviation of $0.01(2\pi/\lambda)$ for $x = \lambda/3$, $10\lambda/3$, $58\lambda/3$, and $178\lambda/3$, where λ is the average acoustic wavelength. The figure renders f_P in an isometric view with the independent R and I axes lying in a horizontal plane. The predicted-field amplitude is independent of x, a direct consequence of the plane wave assumption, while f_P spreads in phase x increases. The phase starts out known, but as x increases, the uncertainty in wave number results in a growing uncertainty in phase. This phase uncertainty growth eventually saturates so that sufficiently far from the source all

phases are essentially equally likely. At such distances, the value of the acoustic field calculations for a coherent signal processing application would be severely degraded. Thus, if more realism can be included, the type of analysis presented here could lead to guidelines for knowing when acoustic-field phase predictions are likely to useful.

Interestingly, the solution to this example problem, Eq. (22), could have been obtained by direct PDF transformations (see Papoulis 1965) using known analytical results for one-dimensional acoustic waves. Thus, the value of the preceding derivation lies in its illustration of the procedure for generating and solving an equation for the evolution of f_P. In more complicated uncertain acoustic environments, direct PDF transformation techniques may not be feasible, but methods paralleling this one-dimensional example may still be possible when exact or approximate values for the conditional moments can be found. In particular, recent PDF-method calculations of turbulence (Lou and Miller 2001, Waclawczyk et al. 2004) and turbulent combustion (Pope 2004, James et al. 2005) follow such an approach using approximate models for the conditional moments.

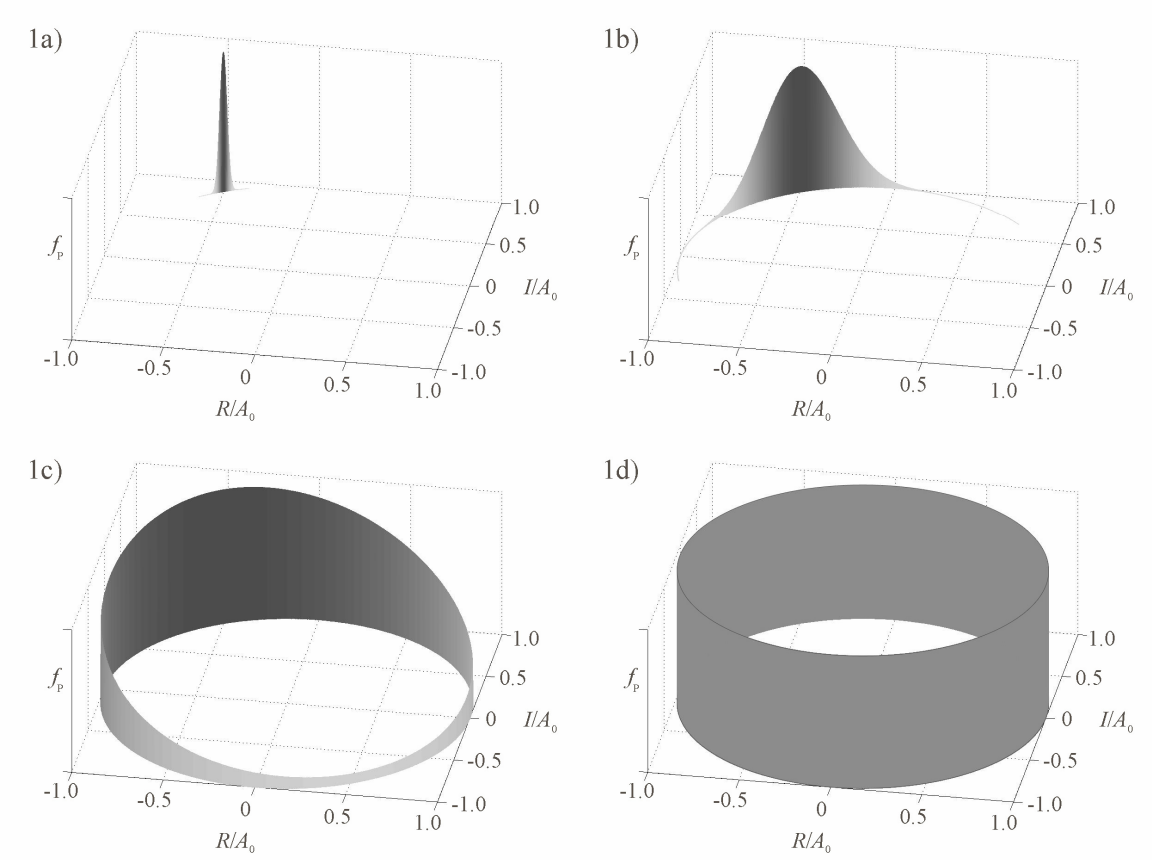

Figure 2.1. Isometric views of the probability density function, f_P, for the real, R, and imaginary, I, parts of a unidirectional acoustic plane wave propagating in an ideal duct with an uncertain wave number at four distances from the sound source. These results are based on Eq. (22). Here the wave number uncertainty has a standard deviation of 1% of the average wave number and A_o is the sound amplitude produced by the zero-phase plane wave source at x=0. The four distances from the source are: (a) $x=\lambda/3$, (b) $x=10\lambda/3$, (c) $x=58\lambda/3$, and (d) $x=178\lambda/3$, where λ is the average acoustic wavelength. The vertical axis is linear not logarithmic.

III. PDF Uncertainty Analysis in Two or More Spatial Dimensions

An equation for the evolution of f_P in two or more spatial dimensions can be found in a manner similar to that given in the previous section where differentiation of Eq. (1) is used to produce Eqs. (5) and (6), except here the Laplacian of the fine-grained PDF in Eq. (1),

$$\nabla^2 f_P = -\frac{\partial f_P}{\partial R}\nabla^2 p_R - \frac{\partial f_P}{\partial I}\nabla^2 p_I + \frac{\partial^2 f_P}{\partial R^2}\left|\nabla p_R\right|^2 + \frac{\partial^2 f_P}{\partial I^2}\left|\nabla p_I\right|^2 + 2 + \frac{\partial^2 f_P}{\partial R \partial I}\nabla p_R \cdot \nabla p_R \quad (23)$$

is needed to create the appropriate mathematical identity for f_P,

$$\nabla^2 f_P = -\frac{\partial}{\partial R}\left(f_P\left\langle \nabla^2 p_R \middle| R,I\right\rangle\right) - \frac{\partial}{\partial I}\left(f_P\left\langle \nabla^2 p_I \middle| R,I\right\rangle\right) + \frac{\partial^2}{\partial R^2}\left(f_P\left\langle \left|\nabla p_R\right|^2 \middle| R,I\right\rangle\right)$$

$$+ \frac{\partial^2}{\partial I^2}\left(f_P\left\langle \left|\nabla p_I\right|^2 \middle| R,I\right\rangle\right) + 2\frac{\partial^2}{\partial R \partial I}\left(f_P\left\langle \nabla p_R \cdot \nabla p_I \middle| R,I\right\rangle\right), \qquad (24)$$

and the Helmholtz equation, $\nabla^2 \hat{p} = -k^2 \hat{p}$ is used to convert this identity [Eq. (24)] into an evolution equation for f_P.

$$\nabla^2 f_P = 2 f_P\left\langle k^2 \middle| R,I\right\rangle + R\frac{\partial}{\partial R}\left(f_P\left\langle k^2 \middle| R,I\right\rangle\right) + I\frac{\partial}{\partial I}\left(f_P\left\langle k^2 \middle| R,I\right\rangle\right)$$

$$+ \frac{\partial^2}{\partial R^2}\left(f_P\left\langle \left|\nabla p_R\right|^2 \middle| R,I\right\rangle\right) + \frac{\partial^2}{\partial I^2}\left(f_P\left\langle \left|\nabla p_I\right|^2 \middle| R,I\right\rangle\right) + 2\frac{\partial^2}{\partial R \partial I}\left(f_P\left\langle \nabla p_R \cdot \nabla p_I \middle| R,I\right\rangle\right) \qquad (25)$$

This is a general evolution equation for the PDF of acoustic pressure when the wave number is uncertain; it is the three-dimensional extension of Eq. (6). It is derived solely from identities and the Helmholtz equation, so it is applicable to all geometries. Unfortunately, it contains four conditional expectations and three terms involving acoustic pressure gradients. These terms prevent a direct solution of Eq. (25) because they cannot be readily determined from the other dependent and independent variables.

Without attempting to approximate or model the conditional expectations, their effect on PDF evolution can be illustrated by examining a solution to Eq. (25) based on direct PDF transformation between the PDF of the uncertain input parameter (an *a priori* PDF) and f_P. In this example, a deterministic acoustic point source radiates sound into an isospeed, uniform-density sound channel having uncertain channel depth *D*, a situation that has been the subject of a prior study on environmental mismatch and matched-field processing (Shang and Wang, 1991).. The solution is constructed directly from the functional dependence of $\hat{p}$ on *D*.

$$f_P(R,I;r,z)=\int_{-\infty}^{+\infty}\delta\left(p_R(r,z,D)-R\right)\delta\left(p_I(r,z,D)-I\right)f_D(D)dD \tag{26}$$

Here, r and z are the usual range and depth coordinates used in underwater acoustics, the source is located at $r = 0$ and $z = z_s$, f_D is the *a priori* PDF of the depth, and $\hat{p}(r,z,D)=p_R+ip_I$ is given by

$$\hat{p}(r,z;D)=iS\sqrt{\frac{8\pi}{r}}\exp\left(-i\frac{\pi}{4}\right)\sum_m\frac{\sin\left(k_{zm}(D)z_s\right)\sin\left(k_{zm}(D)z\right)}{D\sqrt{k_{zm}(D)}}\exp\left(ik_m(D)r\right) \tag{27}$$

(see Kinsler et al. 2000) where S sets the source strength, k_m is the m^{th} mode's horizontal wave number, and k_{zm} is the m^{th} mode's vertical wave number. The sound channel geometry and parameters are provided on Figure 2.2.

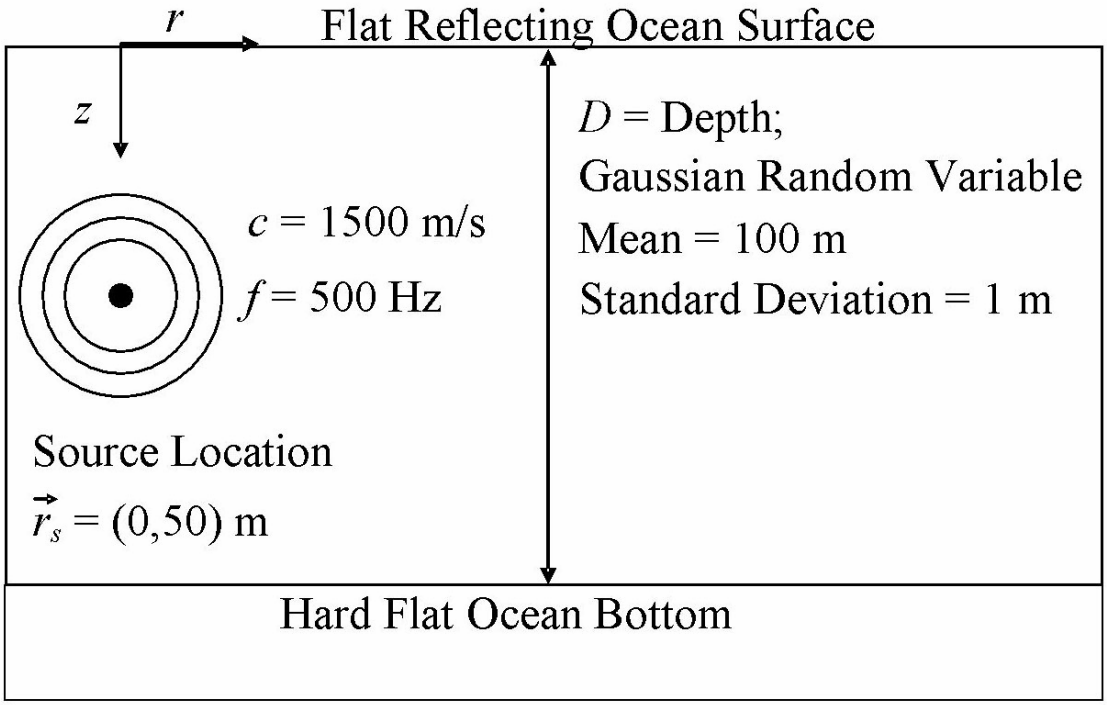

Figure 2.2. The ideal range-independent sound channel and coordinate system.

The primary difficulty in evaluating of Eq. (26) arises from the delta functions which set $f_P(R,I;r,z)$ to zero at nearly all points in the *R-I* plane. Thus, for a chosen spatial location (*r*,*z*), the evaluation of Eq. (26) was done numerically by first finding the locus of points in the *R-I* plane where $f_P(R,I;r,z)$ is nonzero. This locus traces a contour in the *R-I* plane determined by $\hat{p}(r,z;D) = R + iI$ as D is varied from its lower to its upper extreme value. Nonzero, relative values of $f_P(R,I;r,z)$ were then computed by assigning the appropriate value of f_D on this locus of points. The discontinuities where the contour crosses itself were ignored. This simple approach is computationally tractable for a single uncertain parameter, but its computational effort grows exponentially with the number of uncertain parameters, as the PDF will no longer correspond to a single curve in the *R-I* plane.

Sample results are presented in Figure 2.3 for a source with acoustic frequency of 500 Hz, a sound speed of 1500 m/s, a Gaussian distribution of depth having a mean of 100 m and a standard deviation of 1 m, and source and receiver depths of $z_s = z = 50$ m at nominal ranges of 200 m, 1 km, 5 km, and 20 km. In addition, only the first ten propagating modes were included in the sum specified in Eq. (27) as a crude means of modeling real-ocean bottom losses that preferentially attenuate higher-order propagating modes.

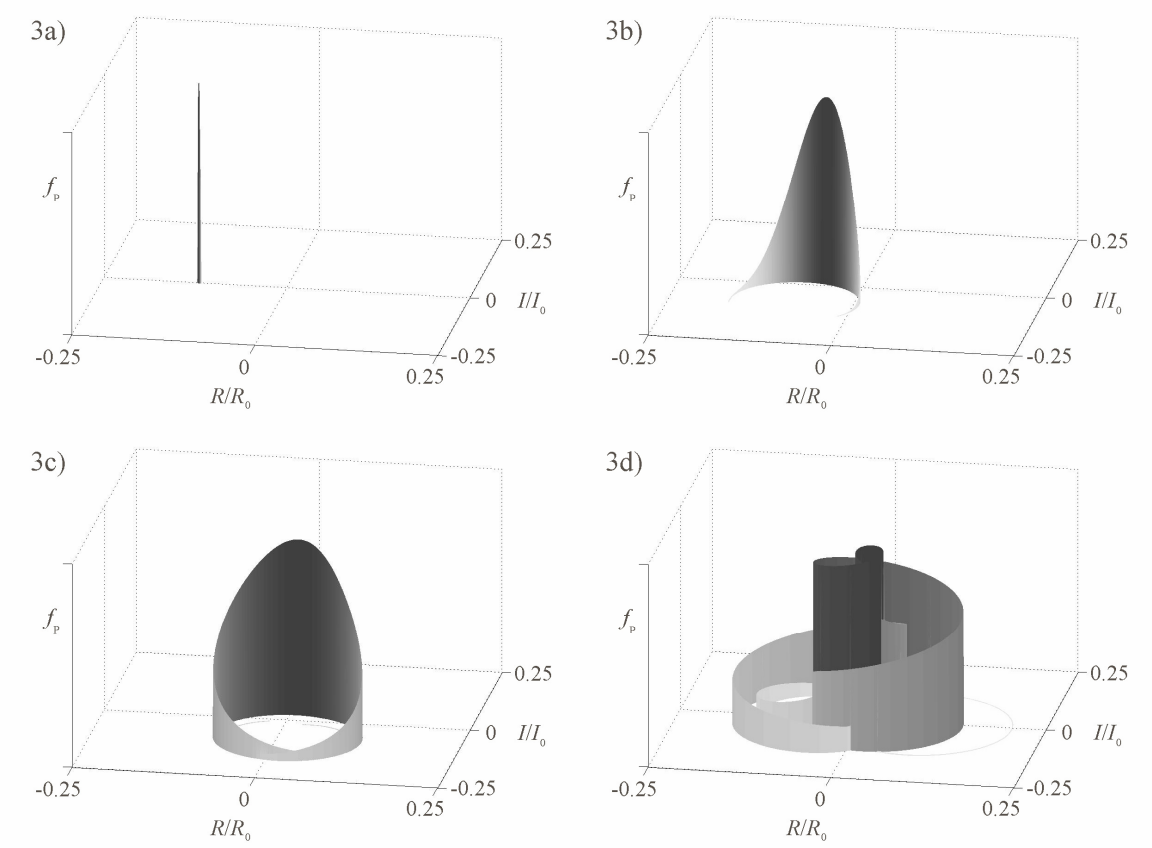

Figure 2.3. Isometric views of the probability density function, f_P, for the real, R, and imaginary, I, parts of the acoustic field propagating in the ideal range-independent sound channel of Fig. 2.2 with an uncertain depth at four distances from a 500 Hz sound source. These results are based numerical evaluation of Eqs. (26) and (27). Here the depth uncertainty has a standard deviation of 1 m, the average depth is 100 m, the source and receiver depths are the same (50 m), and $R_0 = I_0 = S\sqrt{8\pi/r}$ [see Eq. (27)]. The four nominal source-receiver ranges are: a) r = 200 m, b) r = 1 km, c) r = 5 km, and d) r = 20 km. As in Fig. 2.1, the vertical axis is linear not logarithmic and darker shades imply higher probability.

The down-range evolution of f_P shown on Fig. 2.3 has several interesting features. Near the source, the field uncertainty is low and f_P resembles a delta-function spike in the R-I plane, but it spreads along a thin curve as the range increases. This curve is shown in Figure 2.4 as an overhead view of Figure 2.3 d). In this example, unlike in the one-dimensional one, the spreading curve is neither circular nor centered at the origin,

and changes shape with range, so acoustic field uncertainty occurs in both amplitude and phase. Furthermore, the shape of f_P, most noticeably at the three longer ranges, is quite different from the familiar bell-shaped distribution of a joint Gaussian, indicating that an assumption of Gaussian field statistics may be very inaccurate. Furthermore, for ranges greater than 5 km or so, all acoustic-field phases have a non-negligible probability of occurring, and there exists at least a 10 dB range of probable amplitudes, so acoustic field predictions at a single point at such distances might be considered too uncertain to be useful. Increasing the frequency causes the PDF to exhibit similar levels of uncertainty at even shorter ranges.

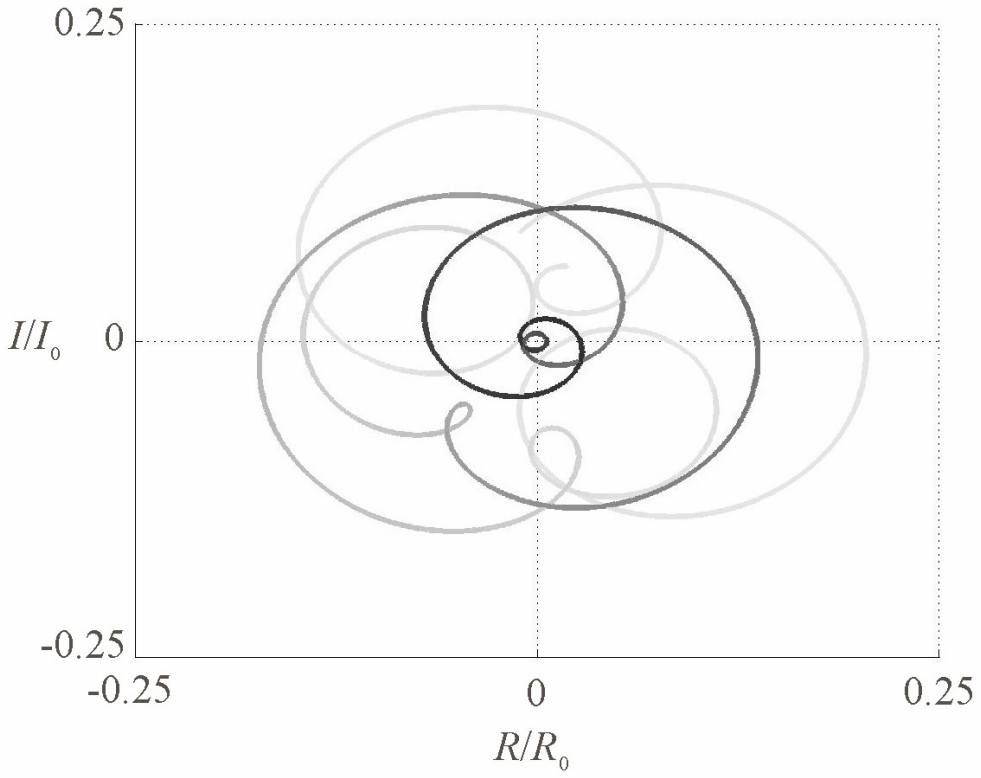

Figure 2.4. Overhead view of Fig. 2.3 d). The spread of f_P is non-Gaussian even though the *a priori* input PDF, f_D, for the uncertain channel depth was Gaussian. As in Figs. 1 and 3, darker shades imply higher probability

Revisiting Eq. (25) in light of the Fig. 2.3 results, it is seen that this complicated behavior must arise from the character of the conditional expectations, so any simplification or approximation to these expectations must keep this character intact. However, if manageable expressions can be developed for these expressions, then PDF evolution analysis has potential as a useful tool for acoustic uncertainty analysis. Such expressions have been developed in other fields where PDF analysis has been applied (see Dopazo 1994, Pope 2000, James et al 2005).

IV. Multipoint PDF Uncertainty Analysis in Two or More Spatial Dimensions

In acoustic array signal processing, the spatial structure of the acoustic field may be as or more important than the phase and amplitude of the field at any particular point. Thus, the two-point PDF of acoustic pressure might also be of interest in uncertain acoustic environments. The following short derivation presents the two-point version of Eq. (25). Generalization to *n*-point PDF equations can be obtained by appropriate extension of the following steps.

Following Lundgren (1967), the equation for the two-point acoustic field PDF, f_{12}, can be built from the two-point fine-grained PDF,

$$f_{12} = \delta(p_{R1} - R)\delta(p_{I1} - I)\delta(p_{R2} - R)\delta(p_{I2} - I) \tag{28}$$

where the extra numerical subscripts throughout this section refer to the two field points, $\vec{x}_1$ and $\vec{x}_2$. Computing the Laplacians of this equation with respect to the first and second field points produces two equations like Eq. (23) with "1" and "2" subscripts. Taking the expected value of these two equations and substituting from the Helmholtz equation

results in two equations for f_{12} with conditional moments that depend on the complex pressure at $\vec{x}_1$ and $\vec{x}_2$. The first of these equations is

$$\nabla_1^2 f_{12} = 2 f_{12}\left\langle k^2 \middle| 1,2 \right\rangle + R_1 \frac{\partial}{\partial R_1}\left(f_{12}\left\langle k^2 \middle| 1,2 \right\rangle \right) + I_1 \frac{\partial}{\partial I_1}\left(f_{12}\left\langle k^2 \middle| 1,2 \right\rangle \right)$$

$$+ \frac{\partial^2}{\partial R_1^2}\left(f_{12}\left\langle \left|\nabla_1 p_{R1}\right|^2 \middle| 1,2 \right\rangle \right) + \frac{\partial^2}{\partial I_1^2}\left(f_{12}\left\langle \left|\nabla_1 p_{I1}\right|^2 \middle| 1,2 \right\rangle \right) + 2\frac{\partial^2}{\partial R_1 \partial I_1}\left(f_{12}\left\langle \nabla_1 p_{R1} \cdot \nabla_1 p_{I1} \middle| 1,2 \right\rangle \right) \qquad (29)$$

where $\left\langle ... \middle| R_1, R_2, I_1, I_2 \right\rangle$ has been abbreviated as $\left\langle ... \middle| 1,2 \right\rangle$. The second equation is identical to Eq. (29) with the "1"-subscripts on ∇, p_R, p_I, R, and I replaced by "2"-subscripts.

For an N-dimensional geometry, the two-point PDF exists in a $2N$-dimensional space consisting of all possible locations of both points (where the value of f_{12} at each point is a function of R_1, I_1, R_2, and I_2). The two equations for f_{12} describe its evolution in this space. For an n-point joint PDF, there would be n such equations, with the expectations conditioned on the pressure values at all n points.

V. Summary and Conclusions

This paper has presented a technique for constructing the evolution equation for the probability density function (PDF) of an uncertain harmonic acoustic field in an uncertain environment. The technique was illustrated through examples involving one and two independent spatial dimensions. One-point and multi-point PDFs and their equations were considered. It has been assumed throughout this research effort that the PDFs of uncertain acoustic fields contain information that may be valuable in applications of acoustics. The following three conclusions can be drawn from this effort.

First, the wavelength scaling for distances, or ranges, that arises in both examples suggests that the behavior of the acoustic-field PDF for fixed frequency and increasing range – as investigated here – will be essentially the same for fixed ranges and increasing frequencies. Thus, even for small input parameter uncertainties, there will be a range at any fixed frequency, or a frequency at any fixed range, beyond or above which the use of a perfect acoustic field model may no longer be useful for predicting the phase of the acoustic field. Thus, the present harmonic-field results provide some insight into broadband-sound acoustic uncertainty, even though it was not explicitly addressed.

Second, uncertain wave propagation involving one or more independent spatial dimensions may not be adequately described by an expected value and a variance (the first two moments of a PDF). In the two-dimensional example provided in Fig. 2.3, the resulting PDF is far from joint-Gaussian, even when the only uncertain input parameter is Gaussian. Although this effect may be less pronounced if a larger number of uncertain input parameters is considered, it prevents an immediate retreat to field-moment-based techniques, like those used for wave propagation in random media, for acoustic uncertainty analysis. Additional investigation could determine if the predicted-field PDF approaches Gaussian behavior when more input parameters are uncertain.

Third, the PDF equations derived here contain complications that were partially overcome in the two examples through the existence of an analytical field model. In the one-dimensional case, for example, the conditional expectation was replaced by the simple relationship between wavenumber, phase, and distance for one-dimensional propagation. Significant complications arise, however, in realistic geometries where, at best, a computational field model is available. When there is no invertible, analytic

relationship between the uncertain parameters and the pressure, the PDF evolution equations contain terms that cannot be explicitly evaluated. If tractable and robust expressions can be found for these terms, the methods described here may become useful tools in acoustic uncertainty analysis.

As a final note, the equations presented herein are not the only candidates for describing the evolution of acoustic-field PDFs. For example, when the acoustic waves travel in nearly the same direction, a PDF equation could be developed from the parabolic approximation to the Helmholtz equation instead of from the Helmholtz equation itself. The different conditional expectations that arise in such an effort may prove to be more or less tractable in certain situations. Uncertainty in acoustic-ray equations could also be analyzed by the PDF-equation construction approach described here. In addition, this approach might be successfully applied to other fields where physical laws are stated via partial differential equations for relevant field quantities such as electricity and magnetism, wave propagation in solids and other media, or physical systems involving thermal or species diffusion. In general, not all PDF equations so generated can be applied to boundary value problems, but they might still provide insight into the origins and propagation of uncertainty in a variety of physical systems.

Chapter 3

The Field Shifting Approximation

Abstract

In underwater acoustics, the accuracy of computational field predictions is commonly limited by uncertainty in environmental parameters. An approximate technique for determining the probability density function (PDF) of computed field amplitude, A, from known environmental uncertainties is presented here. The technique can be applied to several, N, uncertain parameters simultaneously, requires N+1 field calculations, and can be used with any acoustic field model. The technique implicitly assumes independent input parameters and is based on finding the optimum spatial shift between field calculations completed at two different values of each uncertain parameter. This shift information is used to convert uncertain-environmental-parameter distributions

The following chapter was published in 2008 in the Journal of the Acoustical Society of America, Volume 124, pages 1465-1476, with the title "A method for approximating acoustic-field-amplitude uncertainty caused by environmental uncertainties."

into PDF(A). The technique's accuracy is good when the shifted fields match well. Its accuracy is evaluated in range-independent underwater sound channels via an L_1 error-norm defined between approximate and numerically converged results for PDF(A). In 50-m- and 100-m-deep sound channels with 0.5% uncertainty in depth (N=1) at frequencies between 100 and 800 Hz, and for ranges from 1 km to 8 km, 95% of the approximate field-amplitude distributions generated L_1 values less than 0.52 using only two field calculations. Obtaining comparable accuracy from traditional methods requires of order 10 field calculations, and up to 10^N when N>1.

I. Introduction

The solutions to the partial differential equations governing many areas of science and engineering are often highly sensitive to changes in the boundary conditions. Thus, errors or uncertainties in boundary conditions produce corresponding errors and uncertainties in the predicted-field solutions that often overshadow all other sources of error. Since a direct relationship between boundary condition parameters and predicted field values is rarely analytical and invertible, standard error propagation techniques cannot be applied to determine predicted-field uncertainties. Thus, the task of determining predicted-field uncertainty from boundary-condition uncertainty must be application specific and must utilize the unique properties of the particular partial differential equations, boundary conditions, and field solutions of interest. The established approaches for this uncertainty-determination task, Monte-Carlo and direct numerical sampling methods, typically involve a computational burden that increases exponentially with the number of uncertain parameters. This paper describes a technique

to approximately determine the effect of environmental uncertainty on predicted-acoustic-field amplitudes in underwater sound channels that is more efficient.

It is important to make a distinction between uncertain environmental parameters, which produce uncertain field predictions, and randomly-fluctuating environmental parameters, which produce random field solutions. The present work focuses only on the former, while the field of wave propagation in random media addresses the latter; a recent deep-water review can be found in Colosi et al. (1999). Uncertainty in shallow-ocean acoustics has received increased attention in recent years (see Livingston et al. 2006 and references therein). Much of this research can be classified into three categories: determination of environmental parameter uncertainty, prediction of acoustic decision aid uncertainty, and prediction of acoustic field uncertainty. For example, in the first category, Gerstoft and Mecklenbräuker (1998) and Lin et al. (2006) address the problem of assessing uncertainty in environmental parameter inversion, when the input measurements occur in an uncertain environment. The technique described in this paper addresses the reverse question; what is the impact of environmental parameter uncertainty on the prediction of acoustic field amplitude?

In the second category, assessments of uncertainty in various sonar-based tactical decision aids for source detection and localization have also been completed. In Gerstoft et al. (2006), geoacoustic inversion data from the first category of research is used to estimate transmission loss in an uncertain field. A Monte-Carlo approach to estimating the uncertainty of several relevant acoustic observables is outlined in Heaney and Cox (2006), and an application of Monte-Carlo to matched-field processing can be found in Shorey et al. (1994). A maximum entropy method to calculate confidence intervals for

detection of a high-frequency narrow-band source in an uncertain environment is given in Sibul et al. (2004). In addition, environmental uncertainty has been incorporated in a tracking and detection algorithm in order to obtain meaningful results even in the presence of large prediction errors (Stone and Osborn 2004). Similarly, optimal sonar detection performance in diffuse noise has been found to depend primarily on environmental uncertainties and the signal-to-noise ratio at the receivers (Sha and Nolte 2005). The effect of water-depth mismatches on source localization via matched-field processing is explored in Shang and Wang (1991) and D'Spain et al. (1999). An improved source localization algorithm that provides more accurate results with imperfectly known surface statistics than previous methods is described in Haralabus et al. (1993). The effect of uncertainties in water depth, sound speed, and bottom characteristics on source localization uncertainties, using Bayesian inference theory is examined in Dosso (2003) and Dosso et al. (2007a). Even if the field's distribution cannot be determined completely, upper or lower bounds for the uncertainty in various decision aids are highly useful in many applications. A method for obtaining a lower bound for the localization error in a sensor network is provided in Wang et al. (2004). In LePage and McDonald (2006), a lower limit is calculated for the deterioration of performance of time reversal in the presence of sound speed uncertainties. A common feature of a large portion of the work referenced above is the reliance on either Monte-Carlo or direct numerical sampling techniques to explicitly link environmental and acoustic-field uncertainties in the scenario(s) of interest.

In contrast, research efforts in the third category – where the present work belongs – focus on determining the uncertainty in acoustic field propagation calculations that

arises from uncertainty in or imperfect knowledge of the acoustic environment without continuing on to assess how such uncertainties impact sonar performance. Here, the broadly applicable and mathematically-sophisticated technique of polynomial chaos has been applied to sound propagation in uncertain ocean waveguides (Finette 2005 and 2006, Creamer 2006). The polynomial chaos technique is able to provide uncertainty predictions throughout a spatial field for spatially varying uncertain parameters and its convergence criteria are best met when the uncertain spatially varying parameters have finite correlation length. The field-uncertainty prediction technique described in this paper differs from the polynomial chaos work in that it uses simpler mathematics, it provides uncertainty predictions at a selected point in space, and it addresses environmental parameters with infinite correlation length.

The goal of the present work is to produce an acoustic uncertainty determination scheme that is simple (and fast) enough to be used in real time in sonar applications. To this end, the technique has only been developed for approximate determination of the probability density function (PDF) of the predicted-acoustic-field amplitude, A; phase uncertainty is not addressed. As shown herein, the technique may be readily applied to a countable number, N, of uncertain environmental parameters while only requiring N+1 field calculations. In addition, the technique is compatible with any type of acoustic propagation model, analytical or computational. The technique is found to work well when the changes in an uncertain parameter primarily lead to a spatial shift in the predicted acoustic field. Fortunately, such spatial field shifts can often be found (Dosso et al. 2007b). In addition, optimum spatial shifting may provide the basis for a higher-moment model that closes acoustic-PDF transport equations (James and Dowling 2005).

The remainder of the paper is divided into three sections. Section II describes the method when applied to one or more uncertain environmental parameters to produce a prediction for the resulting uncertainty in acoustic amplitude at a point in the field. Section III introduces an L_1 error-norm as a metric for evaluating the accuracy of approximate PDFs. Using this error norm, the success of the approximate technique is reported for a variety of sound channels, of various dimensions, bottom properties, water column properties, and source frequencies. The accuracy of the proposed method is then compared to a simple linear approximation technique that utilizes the same number of field calculations, and to the more-computationally-intense direct numerical sampling method. Section IV summarizes the findings, including the successes and limitations of the approximate technique, and also states the conclusions drawn from this study.

II. Acoustic Amplitude PDF Prediction from Optimum Spatial Shifts

This section describes an approximate technique for determining the PDF of acoustic amplitude for N uncertain environmental parameters based on $N + 1$ acoustic field calculations. The inputs are an acoustic-field calculation routine, the environmental parameters necessary for completing a field calculation, and the PDFs for the uncertain environmental parameters. First, the technique is illustrated via an example calculation conducted at the range-depth location (r,z) for a single uncertain parameter. Instructions and formulae for extending the technique to multiple uncertain parameters follow.

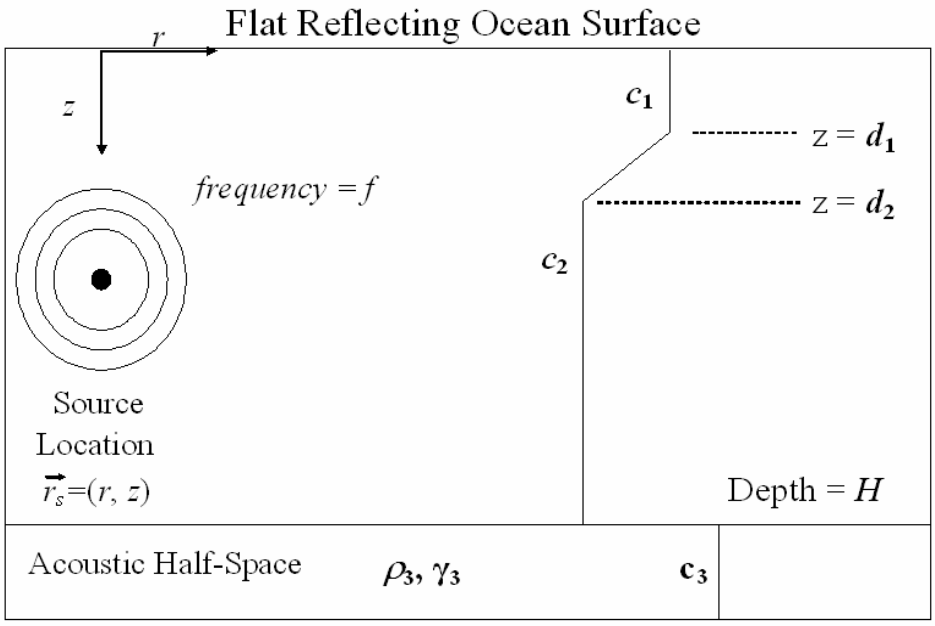

Figure 3.1. Schematic of a generic range-independent sound channel that is described by eight parameters: overall depth H, mixed layer depth d_1, thermocline lower limit d_2, mixed layer sound speed c_1, deep water-column sound speed c_2, bottom sound speed c_3, bottom density ρ_3, and bottom absorption coefficient γ_3. Here mean water column depths of 50 m and 100 m are considered along with bottom types typical of sand, silt, and gravel.

For one uncertain environmental parameter, an approximate field-amplitude PDF at any point can be computed using two range-depth acoustic-field calculations. The examples shown here are from range-independent sound channels, and rely on KRAKEN (Porter and Reiss, 1984) for the field calculations with a unity strength source. The basic idealized range-independent sound channel used in this study is shown in Figure 3.1. It is specified by eight parameters: overall sound channel depth H, mixed layer depth d_1, mixed layer sound speed c_1, thermocline lower limit d_2, deep water-column sound speed c_2, bottom sound speed c_3, bottom density ρ_3, and bottom absorption coefficient γ_3. Of course more sophisticated sound channel parameterizations that include multiple bottom layers, for example, are possible but were not pursued here. For the current example, the

water column depth, H, is presumed uncertain but the distribution of possible H values, PDF(H), is presumed known. The first step is to perform two field calculations at differing values of the uncertain parameter. Here, this means one field calculation with $H = \langle H \rangle$ (the reference calculation) and a second with $H = \overline{H}$ (the sensitivity-assessment calculation). Setting $\overline{H} = \langle H \rangle + \sigma_H$ is recommended, where $\langle H \rangle$ and σ_H are the expected value and standard deviation of H, respectively. Throughout this manuscript uncertain input parameters are assumed to be Gaussian-distributed, reference and sensitivity-assessment calculations are taken one standard deviation apart, $\langle\ \rangle$-brackets indicate an expected value, and $\sigma_{(\ )}$ is the standard deviation of ( ). In the present example with uncertain H, the lower portion of the sound channel is merely extended for the sensitivity-assessment calculation; the channel was not uniformly stretched.

The second step involves selecting the range, R, and depth, Z, dimensions of windows in the computed fields that will be used to determine the optimal spatial shift. Smaller windows allow for better local approximations, however the window must also be large enough to contain the approximate spatial shift corresponding to the $\overline{H} - \langle H \rangle$ change in uncertain input. It is possible to optimize the window size choice via an iterative scheme but results from such an approach are not reported here. In the present effort, the following formulae were used:

$$Z = 2.0 c_2 / f \quad , \text{ and } \quad R = 0.15 Z \left(r / \langle H \rangle \right) \tan \theta_c \qquad \text{(1a,b)}$$

where f is the acoustic frequency (in Hz), $\theta_c = \sin^{-1}\left(c_2 / c_3\right)$ is the critical angle for penetration into the bottom of the idealized sound channel. The approximate PDF results were only mildly sensitive to the constants, 2.0 and 0.15, in the window-size formula;

changing them by ±30% only caused mild degradation of the approximate field-shifting technique's accuracy.

The third step involves finding the optimum spatial shifts, Δr_o and Δz_o, that minimize the normalized root-mean-square amplitude difference, D, between the two windowed sound fields:

$$D\left(r,z,\langle H\rangle;\Delta r,\Delta z,\overline{H}-\langle H\rangle\right)=$$

$$\left[\frac{1}{(Z-\Delta z)(R-\Delta r)}\int_{r+\Delta r-R/2}^{r+R/2}\int_{z+\Delta z-Z/2}^{z+Z/2}\left|\frac{A\left(r'-\Delta r,z'-\Delta z,\overline{H}\right)}{\hat{A}\left(r-\Delta r,z-\Delta z,\Delta r,\Delta z,\overline{H}\right)}-\frac{A\left(r',z',\langle H\rangle\right)}{\hat{A}\left(r,z,\Delta r,\Delta z,\langle H\rangle\right)}\right|^2 dr'dz'\right]^{1/2}, \quad (2a)$$

$$\text{where}\quad \hat{A}\left(r,z,\Delta r,\Delta z,H\right)=\frac{1}{(Z-\Delta z)(R-\Delta r)}\int_{r+\Delta r-R/2}^{r+R/2}\int_{z+\Delta z-Z/2}^{z+Z/2}A\left(r',z',H\right)dr'dz', \quad (2b)$$

$A(r,z,H)$ is the field amplitude at (r,z) when the water column depth is H, and the integration takes place in the region of the overlap between the two field windows. Here, $\hat{A}\left(r,z,\Delta r,\Delta z,H\right)$ is the average amplitude in the overlap region for the field calculated at water column depth H. The limits of integration pre-factors shown in (2a,b) presume Δr and Δz to both be positive. When Δr is negative the upper and lower range-integration limits change to $r+\Delta r+R/2$ and $r-R/2$, respectively, and the range-integration pre-factor becomes $1/(R+\Delta r)$. Similarly, when Δz is negative the upper and lower depth-integration limits change to $z+\Delta z+Z/2$ and $z-Z/2$, respectively, and the depth-integration pre-factor becomes $1/(Z+\Delta z)$.. Since the field amplitudes in each shifted window are divided by the mean amplitude in the window, D is a dimensionless measure of the accuracy of each possible shift. Figure 3.2 shows contour plots of two amplitude fields at f = 400 Hz centered on (r,z) = (3.0 km, 25 m) when $\overline{H}-\langle H\rangle$ = σ_H = 0.25 m,

$H = \langle H \rangle$ = 50 m, $c_1 = \langle c_1 \rangle$ = 1500 m/s, $d_1 = \langle d_1 \rangle$ = 10 m, $c_2 = \langle c_2 \rangle$ = 1450 m/s, $d_2 = \langle d_2 \rangle$ = 20 m, $c_3 = \langle c_3 \rangle$ = 1575 m/s, $\rho_3 = \langle \rho_3 \rangle$ = 1700 kg/m^3 and $\gamma_3 = \langle \gamma_3 \rangle$ = 1.0 dB/wavelength. Nominal bottom properties throughout this manuscript are taken from Table 1.3 in Jensen et al. (1994). Here the optimum shifts are Δr_o = 26.12 m in range and Δz_o = 0.13 m in depth. These optimum spatial shifts approximately quantify the effect of changing H from $\langle H \rangle$ to $\overline{H}$.

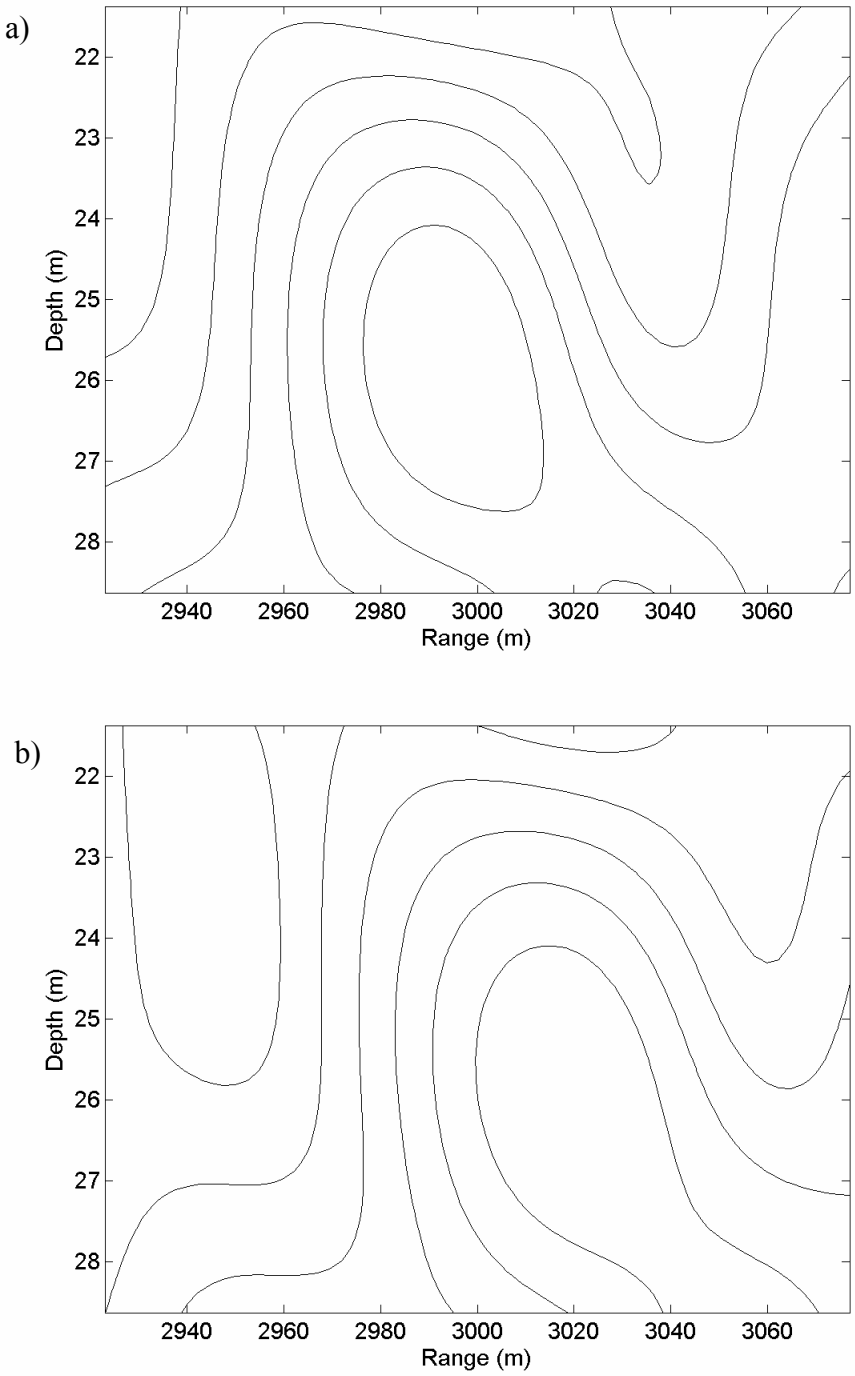

Figure 3.2. Representative contour plots of small sections of an acoustic field at $f = 400$ Hz centered on $(r,z) = (3.0 \text{ km}, 25 \text{ m})$ in a sound channel when the channel depth is $\langle H \rangle = 50$ m (a), and when it is $\langle H \rangle + \sigma_H = 50.25$ m (b).

The fourth step involves extending the approximate-shift relationship to larger or smaller changes in the uncertain parameter. To accomplish this, the optimum spatial shifts are used to determine constants in assumed proportionalities between changes in uncertain parameters and shifts in the spatial coordinates. For the present example involving uncertain channel depth, H, these proportionalities are:

$$\frac{\Delta r}{r} = \alpha \frac{\left(H - \langle H \rangle\right)}{\langle H \rangle}, \quad \text{and} \quad \frac{\Delta z}{z} = \beta \frac{\left(H - \langle H \rangle\right)}{\langle H \rangle}. \tag{3a,b}$$

The proportionality constants α and β are determined from the optimum shift information. These relationships are inspired by the form of the waveguide invariant (Brekhovskikh and Lysanov 1991, D'Spain and Kuperman 1999), and the observation that small mismatches or changes in environmental parameters often lead to spatial shifts in matched field source location (D'Spain et al. 1999), and in measured and computed acoustic fields (Kim et al. 2003, Dosso et al. 2007b). Naturally, (3) provides just one simple parameterization; other choices are possible. Thus, the calculations for the fourth step merely involve inverting (3) with $H = \overline{H}$ to find the constants:

$$\alpha = \left(\frac{\Delta r_o}{r}\right) \Bigg/ \left(\frac{\overline{H} - \langle H \rangle}{\langle H \rangle}\right), \quad \text{and} \quad \beta = \left(\frac{\Delta z_o}{z}\right) \Bigg/ \left(\frac{\overline{H} - \langle H \rangle}{\langle H \rangle}\right). \tag{4a,b}$$

For the example fields shown in Figure 3.2, α = 1.74, and β = 1.04. It is important to note that α and β are only locally constant - appropriate values must be recalculated at each point of interest. With these two constants determined, the field amplitude at the point of interest (r,z) for an arbitrary water column depth, H, can be approximated by the field amplitude at a shifted location in the field calculated at $H = \langle H \rangle$. Since the acoustic field was also calculated at $H = \overline{H}$, the arbitrary-water-column depth field

amplitude can also be approximated via spatial shifting in this second field calculation. These shifts are of the same form as (3):

$$\frac{\Delta\bar{r}}{r} = \bar{\alpha}\frac{\left(H-\overline{H}\right)}{\overline{H}}, \quad \text{and} \quad \frac{\Delta\bar{z}}{z} = \bar{\beta}\frac{\left(H-\overline{H}\right)}{\overline{H}}, \tag{5a,b}$$

where $\bar{\alpha}$ and $\bar{\beta}$ are found via an algebraic inversions similar to (4)

$$\bar{\alpha} = \left(\frac{-\Delta r_o}{r}\right) \Bigg/ \left(\frac{\langle H\rangle - \overline{H}}{\overline{H}}\right), \quad \text{and} \quad \bar{\beta} = \left(\frac{-\Delta z_o}{z}\right) \Bigg/ \left(\frac{\langle H\rangle - \overline{H}}{\overline{H}}\right). \tag{6a,b}$$

Linear interpolation between the two approximations yields a final weighted approximation for $A(r,z,H)$,

$$A(r,z,H) \approx$$

$$A\left(r-\Delta r, z-\Delta z, \langle H\rangle\right) + \left(\frac{H-\langle H\rangle}{\overline{H}-\langle H\rangle}\right)\left[A\left(r-\Delta\bar{r}, z-\Delta\bar{z}, \overline{H}\right) - A\left(r-\Delta r, z-\Delta z, \langle H\rangle\right)\right]. \tag{7}$$

Equation (6) provides the fundamental simplification of the approximate field shifting technique. The advantage lies in the fact that $A\left(r,z,\langle H\rangle\right)$ and $A\left(r,z,\overline{H}\right)$ have been calculated in the first step while $A(r,z,H)$ has not. Thus, (6) allows many field calculations at different *H*-values to be bypassed. However, it is approximate as shown in Figure 3.3(a) where amplitude vs. water column depth sensitivity curves are plotted at a receiver range of 6.0 km and depth of 25 m. The two curves in Fig. 3.3(a) are similar but not identical. The dashed curve from (6) is based on two field calculations while the solid curve was obtained from 41 field calculations at *H*-values spanning $\langle H\rangle \pm 3\sigma_H$. The straight dotted line in Fig. 3.3(a) is a simple two-point linear fit to the values of $A\left(r,z,\langle H\rangle\right)$ and $A\left(r,z,\overline{H}\right)$ at the spatial location of interest:

$$A(r,z,H) \approx A\left(r,z,\langle H\rangle\right)+\left(\frac{A\left(r,z,\overline{H}\right)-A\left(r,z,\langle H\rangle\right)}{\overline{H}-\langle H\rangle}\right)\left(H-\langle H\rangle\right). \tag{8}$$

The remaining frames of Fig. 3.3 show approximate field-shift sensitivity curves obtained from (7) when the various environmental parameters of the Fig. 3.1 sound channel are individually uncertain. The line types in Fig. 3.3(a) are followed in the subsequent frames of Fig. 3.3. These calculations were performed for the same frequency, geometry, and environmental parameters as Fig. 3.2. The standard deviations of the various input parameters are listed in the Fig. 3.3 caption. In this case, the various results show good agreement between the results of (6), when applied to each environmental parameter, and direct calculations, even though the various sensitivity curves are clearly nonlinear.

Figure 3.3. Sensitivity curve comparisons at f = 400 Hz and (r,z) = (6.0 km, 25 m) between approximate results from (7) (dashed curve) and (8) (dotted line) using field computations similar to that shown in Fig. 3.2 and numerically converged results (solid curve) based on 41 field computations for each of the eight parameters that specify the Fig. 3.1 sound channel: (a) uncertain depth with $\langle H \rangle$ = 50 m, and $\sigma_H / \langle H \rangle$ = 0.005, (b) uncertain mixed layer sound speed with $\langle c_1 \rangle$ = 1500 m/s, and $\sigma_{c_1} / \langle c_1 \rangle$ = 0.001, (c) uncertain deep-channel sound speed with $\langle c_2 \rangle$ = 1450 m/s, and $\sigma_{c_2} / \langle c_2 \rangle$ = 0.0001, (d) uncertain mixed layer depth with $\langle d_1 \rangle$ = 10 m, and $\sigma_{d_1} / \langle d_1 \rangle$ = 0.01, (e) uncertain depth to the bottom of the thermocline with $\langle d_2 \rangle$ = 20 m, and $\sigma_{d_2} / \langle d_2 \rangle$ = 0.005, (f) uncertain bottom sound speed with $\langle c_3 \rangle$ = 1575 m/s, and $\sigma_{c_3} / \langle c_3 \rangle$ = 0.005, (g) uncertain bottom density with $\langle \rho_3 \rangle$ = 1700 kg/m^3, and $\sigma_{\rho_3} / \langle \rho_3 \rangle$ = 0.05, and (h) uncertain bottom sound absorption coefficient with $\langle \gamma_3 \rangle$ = 1.0 dB/wavelength, and $\sigma_{\gamma_3} / \langle \gamma_3 \rangle$ = 0.10 (note that the dashed and dotted curves overlap for this case). In each plot, the horizontal axis spans three standard deviations of the uncertain parameter.

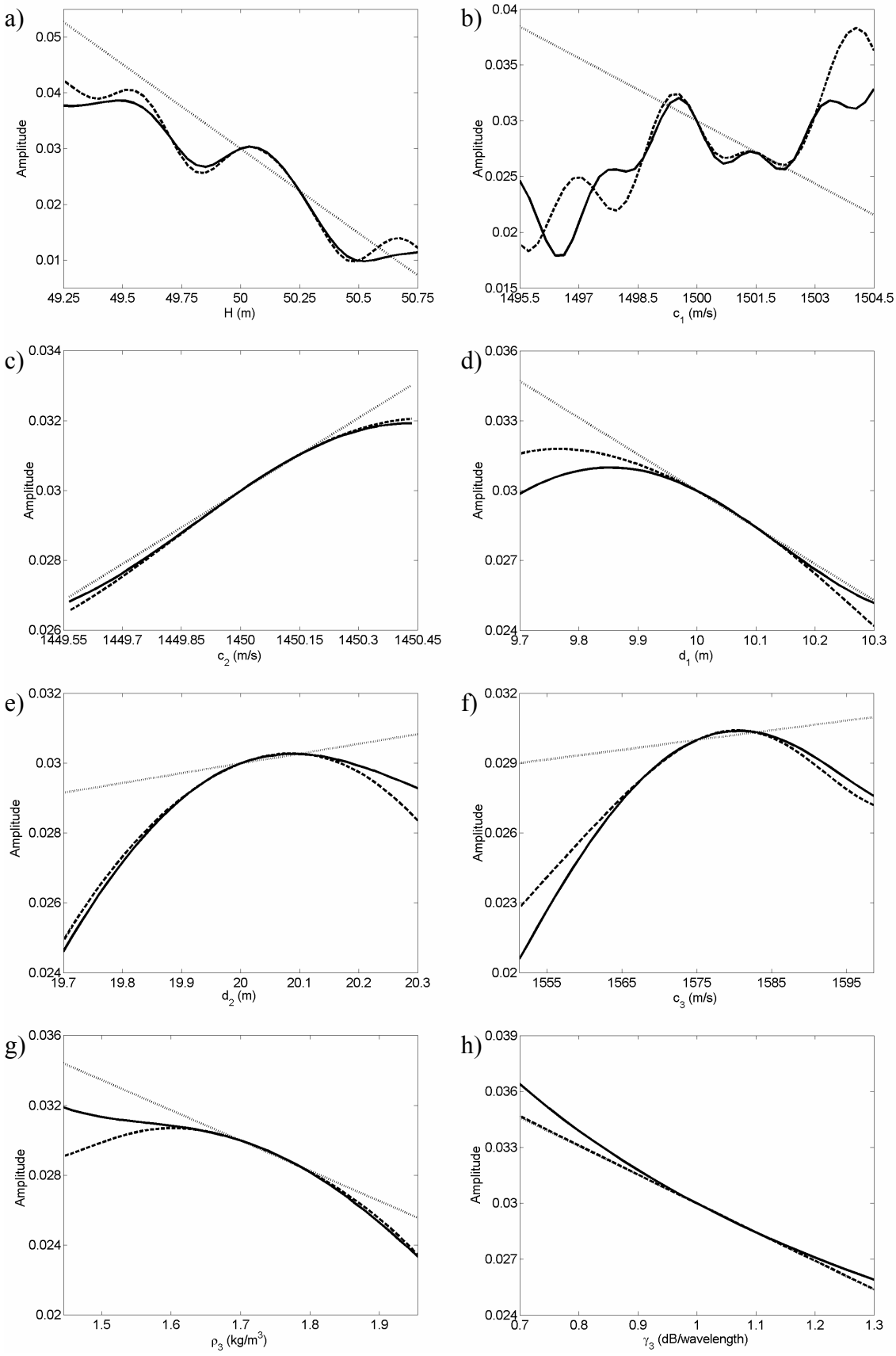
a)
Amplitude
H (m)
b)
Amplitude
c_1 (m/s)
c)
Amplitude
c_2 (m/s)
d)
Amplitude
d_1 (m)
e)
Amplitude
d_2 (m)
f)
Amplitude
c_3 (m/s)
g)
Amplitude
ρ_3 (kg/m^3)
h)
Amplitude
γ_3 (dB/wavelength)

The fifth and final step of the technique is to generate an approximate field-amplitude PDF from the sensitivity data using standard transformation techniques (see Papoulis 1965) and the known input uncertain-parameter distribution, PDF(H) in this example. Figure 3.4(a) shows both the approximate and numerically-converged PDFs obtained from the sensitivity curves in Figure 3.3(a), when the input water column depth distribution has σ_H = 0.25 m. Note that the amplitude PDF is approximated well by the technique described here. Furthermore, the actual amplitude PDF is clearly non-Gaussian even though the uncertainty is only 0.5% of the mean depth, and the input PDF is Gaussian. This happens because the acoustic amplitude depends on water depth in a nonlinear manner, and, in this case, values of H above and below $\langle H \rangle$ can produce acoustic amplitudes that are below that produced by $H \approx \langle H \rangle$. The remaining frames of Figure 3.4 show PDF(A) obtained from numerically-converged direct-sampling calculations, the field shifting technique, and simple linear fitting when the various environmental parameters of the Fig. 3.1 sound channel are individually uncertain. In Fig. 3.4 the line types, frequency, geometry, and environmental parameters and their uncertainties are the same as those in Fig. 3.3. In each case, the field-shift-produced PDF(A) show better agreement with the numerically-converged PDF(A) than the PDF(A) developed from simple linear fitting. However, the two approximate approaches will perform similarly when the relevant amplitude sensitivity curve is linear, such as in Figs. 3(h) and 4(h).

Figure 3.4. Same as Fig. 3.3, except here the acoustic-field amplitude PDFs are plotted for the case when each of the eight parameters that specify the Fig. 3.1 sound channel is uncertain.

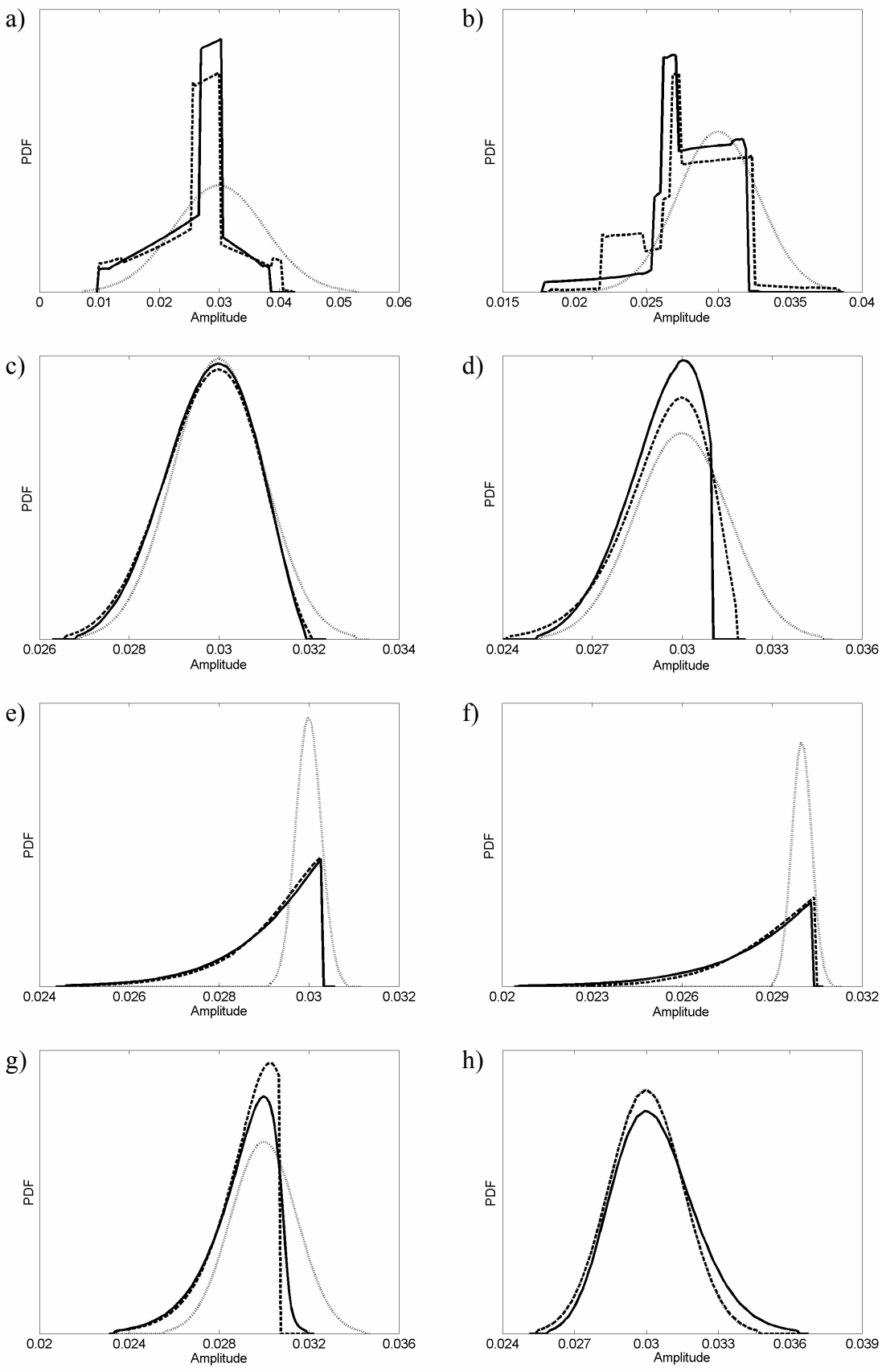
a)
PDF
0
0.01
0.02
0.03
0.04
0.05
0.06
Amplitude
b)
PDF
0.015
0.02
0.025
0.03
0.035
0.04
Amplitude
c)
PDF
0.026
0.028
0.03
0.032
0.034
Amplitude
d)
PDF
0.024
0.027
0.03
0.033
0.036
Amplitude
e)
PDF
0.024
0.026
0.028
0.03
0.032
Amplitude
f)
PDF
0.02
0.023
0.026
0.029
0.032
Amplitude
g)
PDF
0.02
0.024
0.028
0.032
0.036
Amplitude
h)
PDF
0.024
0.027
0.03
0.033
0.036
0.039
Amplitude

The field shifting technique can be readily extended to multiple uncertain input parameters with a few modifications to the five steps enumerated above. Here, for simplicity, independence of the input uncertain parameters is assumed as well. Incorporation of dependencies between uncertain inputs, while not inconsistent with the proposed approximation method, was beyond the scope of this effort.

For multiple uncertain parameters, the first four steps of the single-parameter method are performed independently for each uncertain input parameter, ψ_i, $1 \le i \le N$. This involves one reference calculation and N sensitivity-assessment field calculations. The N-uncertain-parameter extension of (3) can be readily formulated:

$$\frac{\Delta r}{r} = \sum_{i=1}^{N} \alpha_i \frac{\left(\psi_i - \langle \psi_i \rangle\right)}{\langle \psi_i \rangle}, \quad \text{and} \quad \frac{\Delta z}{z} = \sum_{i=1}^{N} \beta_i \frac{\left(\psi_i - \langle \psi_i \rangle\right)}{\langle \psi_i \rangle}, \tag{9a,b}$$

where the α_i and β_i are determined from:

$$\alpha_i = \left(\frac{(\Delta r_o)_i}{r}\right) \Bigg/ \left(\frac{\overline{\psi}_i - \langle \psi_i \rangle}{\langle \psi_i \rangle}\right), \quad \text{and} \quad \beta_i = \left(\frac{(\Delta z_o)_i}{z}\right) \Bigg/ \left(\frac{\overline{\psi}_i - \langle \psi_i \rangle}{\langle \psi_i \rangle}\right). \tag{10a,b}$$

where $(\Delta r_o)_i$ and $(\Delta z_o)_i$ are the optimum range and depth shifts for variations in ψ_i. The N-uncertain-parameter extensions of (5) and (6) follow from (9) and (10). The N-uncertain-parameter extension of (7) is:

$$A(r, z, \psi_1, \psi_2, ..., \psi_N) \approx A_0 + \sum_{i=1}^{N} \left(\frac{\psi_i - \langle \psi_i \rangle}{\overline{\psi}_i - \langle \psi_i \rangle} \right) \left[A_i - A_0 \right] \tag{11}$$

where $A_0 = A\left(r - \Delta r, z - \Delta z, \langle \psi_1 \rangle, \langle \psi_2 \rangle, ..., \langle \psi_N \rangle\right)$ is the reference field calculation evaluated at the appropriate shift location, and the $A_i = A\left(r - (\Delta \bar{r})_i, z - (\Delta \bar{z})_i, \langle \psi_1 \rangle, \langle \psi_2 \rangle, ..., \langle \psi_{i-1} \rangle, \overline{\psi}_i, \langle \psi_{i+1} \rangle, ..., \langle \psi_N \rangle\right)$ are the N sensitivity-

assessment calculations, each evaluated at its appropriate-shift location. Similarly, the *N*-uncertain-parameter extension of (8), the simple linear approximation, is:

$$A(r,z,\psi_1,\psi_2,...,\psi_N) = A\left(r,z,\langle\psi_1\rangle,\langle\psi_2\rangle,...,\langle\psi_N\rangle\right)+$$

$$\sum_{i=1}^{N}\left(\frac{\psi_i-\langle\psi_i\rangle}{\overline{\psi}_i-\langle\psi_i\rangle}\right)\left[A\left(r,z,\langle\psi_1\rangle,\langle\psi_2\rangle,...,\langle\psi_{i-1}\rangle,\overline{\psi}_i,\langle\psi_{i+1}\rangle,...,\langle\psi_N\rangle\right)-A\left(r,z,\langle\psi_1\rangle,\langle\psi_2\rangle,...,\langle\psi_N\rangle\right)\right] \quad (12)$$

To illustrate these formulae, consider the Fig. 3.1 sound channel with uncertain depth H and mixed-layer sound speed c_1 at f = 250 Hz and r = 4.0 km, with all other parameters evaluated at the mean values given in Fig. 3.3. Here, three field calculations were performed for the field shifting and simple linear techniques – the reference calculation at $\langle H\rangle$ and $\langle c_1\rangle$, the depth sensitivity assessment calculation at $\overline{H} = \langle H\rangle + \sigma_H$ and $\langle c_1\rangle$, and the mixed-layer sound-speed sensitivity assessment calculation at $\langle H\rangle$ and $\overline{c}_1 = \langle c_1\rangle + \sigma_{c_1}$. Figure 3.5 shows the amplitude PDF results from the approximate field-shifting technique (dashed curve), numerically converged direct sampling (solid curve), and simple linear fitting (dotted curve) for $\sigma_H/\langle H\rangle$ = 0.005, and $\sigma_{c_1}/\langle c_1\rangle$ = 0.001. In this case, the field-shifting PDF is clearly more accurate than the one obtained from simple linear fitting. For reference, the direct sampling PDF shown in Figure 3.5 required more than 400 field calculations.

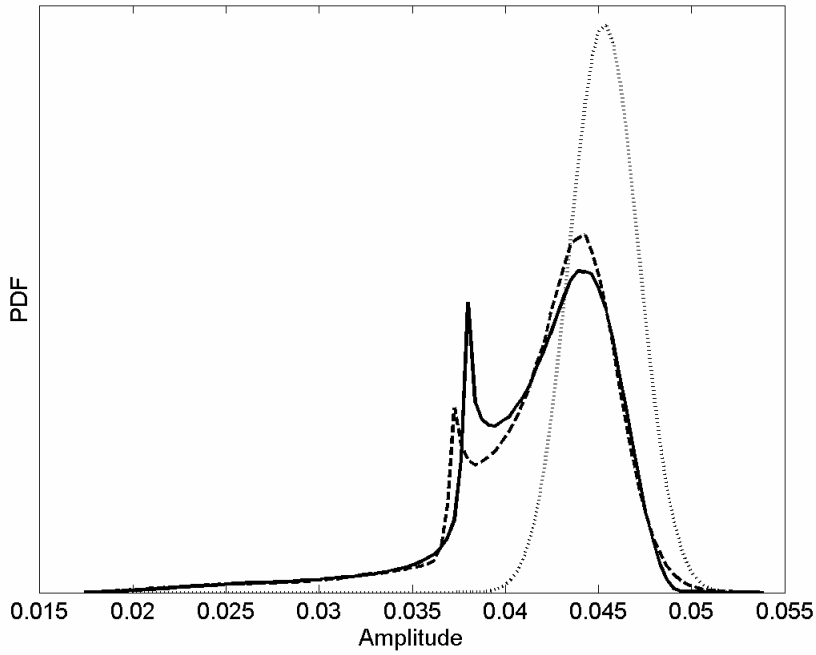

Figure 3.5. Approximate and numerically converged PDFs of the acoustic field amplitude for two uncertain parameters: depth, H, and mixed layer sound speed, c_1, at $f = 250$ Hz and $r = 4.0$ km with all other parameters, including line types, the same as for Fig. 3.3. The numerically converged PDF comes from more than 400 field calculations.

When multiple parameters are uncertain, the proportionality constants, α_i and β_i, may depend slightly on the values of the other uncertain parameters, ψ_j for $j \neq i$. However, anticipated applications of the approximate field-shifting technique are likely to involve only small relative changes in the uncertain parameters, so any dependence of the proportionality constants on the other environmental parameters is suppressed. Although this suppression reduces accuracy, this accuracy reduction primarily occurs in cases where the uncertain input parameters have relatively wide distributions and the utility of acoustic field predictions may have been lost because the final amplitude uncertainties are many decibels.

A comparison of numerically converged and approximate PDFs is shown in Figure 3.6 when three environmental parameters are uncertain. The line types and parameters are the same as in Figs. 3-5, except that for this example f = 600 Hz and r = 1.0 km with $\sigma_{d_1} / \langle d_1 \rangle$ = 0.01. Again the field-shifting PDF is closer to the direct sampling result than the one obtained from simple linear fitting. Here, the direct sampling PDF shown in Fig. 3.6 required more than 9,000 field calculations.

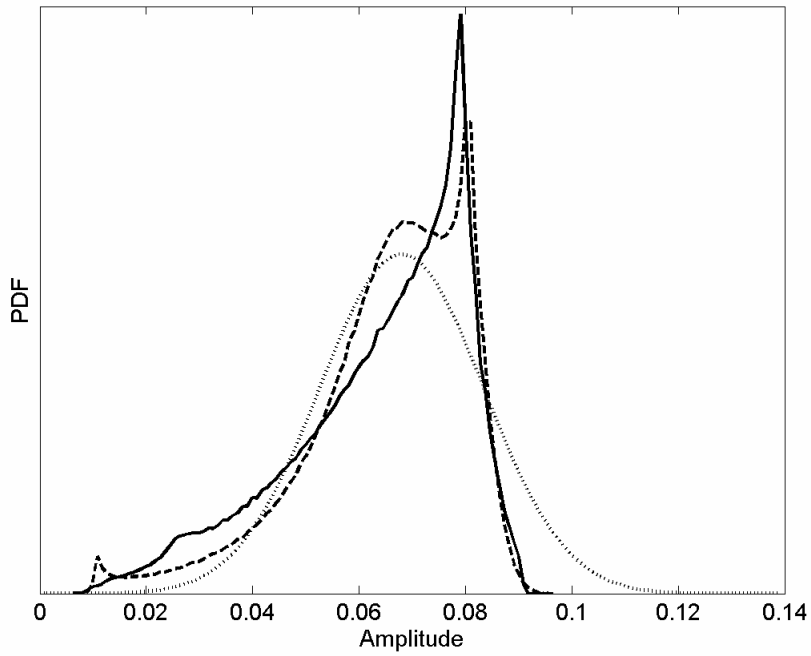

Figure 3.6. Approximate and numerically converged PDFs of the acoustic field amplitude for three uncertain parameters: depth, H, mixed layer sound speed, c_1, and mixed layer depth, d_1, at f = 600 Hz and r = 1.0 km with all other parameters, including line types, the same as for Fig. 3.3. The numerically converged PDF comes from more than 9,000 field calculations.

As might be expected, when uncertainties in the input parameters and the number of uncertain input parameters both increase, larger discrepancies are possible between the approximate and numerically converged distributions. In practice, however, this loss of accuracy is balanced by the fact that as the input parameters, and thus the acoustic

amplitude, become more uncertain, precise information about the amplitude distribution becomes less important for the anticipated applications of this technique. For example, a prediction of 12 dB of amplitude uncertainty may have the same impact on a sonar decision aid as 10 dB or 15 dB of uncertainty.

III. Assessment of Accuracy

The examples in the previous section demonstrate that it is possible to apply the approximate-PDF technique with great computational savings, but they do not provide a statistically compelling indication of the reliability or the accuracy of the technique. In this section, the accuracy of this technique is explored over variations in sound channel parameters. This technique's accuracy is then compared to simple linear PDF transformation using the same number, N+1, of field calculations, and to the direct numerical sampling method, which has a computational burden that increases exponentially with N.

Although the accuracy of an approximate PDF can be reported by comparing its moments to those determined from an exact distribution, approximate PDF accuracy is quantified here via an L_1 error norm:

$$L_1 = \int_o^\infty \left| \mathrm{PDF}_a(A) - \mathrm{PDF}_c(A) \right| dA \ , \tag{13}$$

where PDF_a and PDF_c are approximate and numerically converged PDFs, respectively. This choice was made because L_1 provides a dimensionless single-number overall evaluation of PDF matching, and because it has a simple geometric interpretation as the non-overlapping area of PDF_a and PDF_c. in plots like Figs. 4-6. The more common L_2 error norm, which would have $\left| \mathrm{PDF}_a(A) - \mathrm{PDF}_c(A) \right|^2$ as the integrand, was bypassed for

accuracy assessments because it is not dimensionless. The lowest possible value for L_1 is zero, indicating a perfect match between the two PDFs (perfect accuracy), while the highest possible value for the L_1 is two, indicating no overlap between the two PDFs (complete inaccuracy).

For the L_1-calculations, the numerically converged PDF in (13) was obtained from direct numerical sampling. For each uncertain parameter – for example H – direct numerical sampling involves K equally-spaced-in-H computations of $A(r,z,H)$ that span the range of possible H values. For N uncertain parameters, this corresponds to K^N field calculations. Interpolation in the resulting data yields an acoustic-amplitude sensitivity curve (or surface) for changes in all uncertain inputs. This sensitivity data, combined with the distributions for all the uncertain inputs, yields a numerically converged amplitude PDF via standard PDF transformation techniques, as noted for the field-shifting technique. The value of K required to generate smooth $A(r,z,H)$ and PDF(A) curves varies with the complexity of the sensitivity curves; values between 11 and 41 were used for the calculations presented here.

The L_1 values found in this investigation varied from less than 0.001 to more than 1.0. For the PDFs shown in Figs. 4(a)-(h), 5, and 6, the L_1 values are 0.26, 0.42, 0.03, 0.23, 0.06, 0.15, 0.16, .015, 0.13, and 0.20, respectively, for the field-shifting-technique PDFs, and are 0.71, 0.52, 0.12, 0.52, 1.06, 1.25, 0.49, 0.16, 0.88, and 0.37, respectively, for the simple-linear-fit PDFs. Furthermore, the means and standard deviations of the field-shifting-technique PDFs are within 2% and 20%, respectively, of the numerically converged values. Such L_1 and moment-difference errors are presumed to be small

enough for successful use of the approximate field-shifting PDF technique in many applications for uncertainty analysis.

The overall accuracy of the approximate-PDF technique for a single uncertain parameter – the sound channel depth H – in the idealized Fig. 3.1 sound channel was assessed by performing many calculations at several receiver locations (r = 1 km, 2 km, 4 km, 6 km, 8 km, z = $\left(\langle d_1\rangle + \langle d_2\rangle\right)/2$, $\langle H\rangle/2$, and $3\langle H\rangle/4$) for a variety of environmental parameters to obtain a broad sample of L_1 values. The source was always located at $r = 0$ and $z = \langle H\rangle/2$, and the input channel-depth distribution, PDF(H), had standard deviation of $\sigma_H/\langle H\rangle$ = 0.005. This input uncertainty level was chosen to incorporate cases of high and low amplitude uncertainty, as well as high and low approximation accuracy. The results of this study are shown in Figure 3.7 which provides two scatter plots of L_1 vs. the number of propagating modes for sound frequencies between 100 Hz and 800 Hz and bottom properties of soft silt (c_3 = 1575 m/s, ρ_3 = 1700 kg/m^3, γ_3 = 1.0 dB/wavelength), sand (c_3 = 1650 m/s, ρ_3 = 1900 kg/m^3, γ_3 = 0.8 dB/wavelength), and gravel (c_3 = 1800 m/s, ρ_3 = 2000 kg/m^3, γ_3 = 0.6 dB/wavelength) when $\langle H\rangle$ = 100 m [Fig. 3.7(a)] and when $\langle H\rangle$ = 50 m [Fig. 3.7(b)]. The other water column properties were not altered from their Fig. 3.2 values.

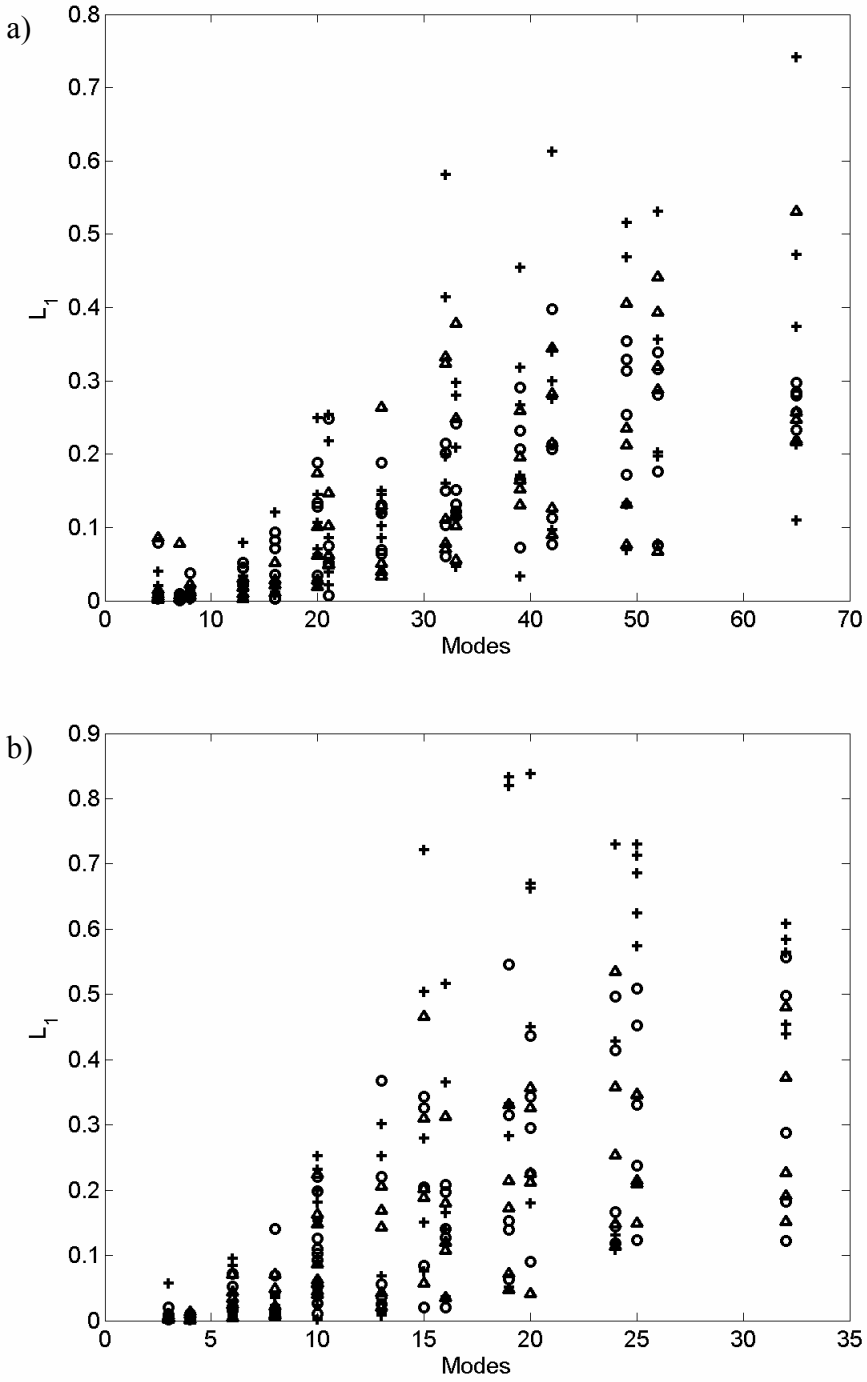

Figure 3.7. Scatter plots of L_1-values vs. the number of propagating modes in the sound channel for frequencies from 100 Hz to 800 Hz and source receiver ranges from 1 km to 8 km: (a) 100-m-deep channel with receiver depths of 15 m (pluses), 50 m (circles), and 75 m (triangles), and (b) 50-m-deep channel with receiver depths of 15 m (pluses), 25 m (circles), and 37.5 m (triangles). All other parameters are as specified in Fig. 3.3.

The primary finding is that the number of modes in the sound channel and the quality of initial shifted-field matching (the third step in the technique's basic procedure) were the best indicators for the potentially high L_1 values for a single uncertain variable. Here, the number of propagating modes was determined directly from the KRAKEN output and it is used as a surrogate for the complexity of acoustic propagation in the idealized sound channels. Comparisons of the panels of Fig. 3.7 show that L_1 increases when the sound channel is shallower and the sound speed's depth dependence occupies a larger fraction the channel depth. However, the overall assessment of the approximate field-shifting technique is positive, as 95% of all the cases investigated with a 0.5% uncertainty in channel depth return L_1 values less than 0.52 even though 26% of the points in Figure 3.7 have $\sigma_A / \langle A \rangle$ greater than 0.4.

The outlying high-L_1 points occur when the difference between $A\left(r,z,\langle H \rangle\right)$ and $A\left(r,z,\overline{H}\right)$ in the local region around (r,z) is not readily described by a spatial shift. As Figure 3.7 illustrates, this can occur as the number of propagating modes in the field increases, but for an arbitrary uncertain input parameter there may exist conditions for which small changes do not correspond to spatial shifts. However, the occurrence of high-L_1 values can be anticipated without knowing $\mathrm{PDF}_c(A)$. Figure 3.8 shows a log-log scatter plot of all the Fig. 3.7 L_1 data vs. $D_{\min} = D\left(r,z,\langle H \rangle;\Delta r_o,\Delta z_o,\sigma_h\right)$. Although the L_1 points are scattered, the trend of increasing L_1 with increasing $D_{\min}$ is clear; when $D_{\min}$ is less than 0.25, 95% of the approximate field-shift-produced PDFs generated L_1 values below 0.35. Higher values of $D_{\min}$ indicate that changes in the uncertain parameter at the point of interest do not produce simple spatial shifts of the field, and the resulting field-shift-produced PDFs may have higher L_1 errors. Hence, these D_{min} calculations, which do

not require knowledge of PDF$_c$(A) and are already part of the approximate field-shift PDF technique, can indicate, at least approximately, when the final approximate PDF(A) result for that (r,z) location may be inaccurate.

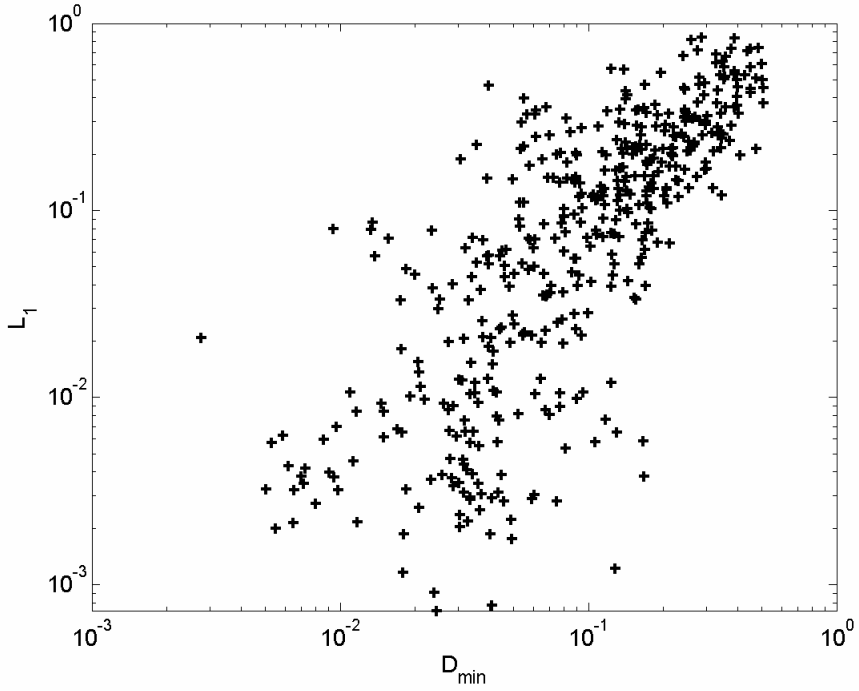

Figure 3.8. Log-log plot of L_1 vs. the normalized root-mean-square amplitude difference at the optimum field shift, $D_{\min}$, for the calculations shown in Fig. 3.7. Although there is scatter, increasing L_1 is clearly correlated with increasing $D_{\min}$.

Similar L_1 accuracy assessments were conducted for two uncertain parameters, channel depth H and water column sound speed c_1, using the idealized Fig. 3.1 sound channel. Figure 3.9 displays L_1 vs. number of modes for the same frequencies, ranges, and parameters used for Fig. 3.7 with $\langle H \rangle$ = 50 m, $\sigma_H / \langle H \rangle$ = 0.005, $\langle c_1 \rangle$ = 1500 m/s, $\sigma_{c_1} / \langle c_1 \rangle$ = 0.001, and a receiver depth of 25 m. Here, 95% of the cases investigated yielded L_1 below 0.57. Again, high-L_1 outliers can exist where changes in one or both uncertain parameters do not directly correspond to a spatial shift in the field, but these

can be anticipated from their associated $D_{\min}$ values, as was illustrated for one uncertain parameter in Fig. 3.8.

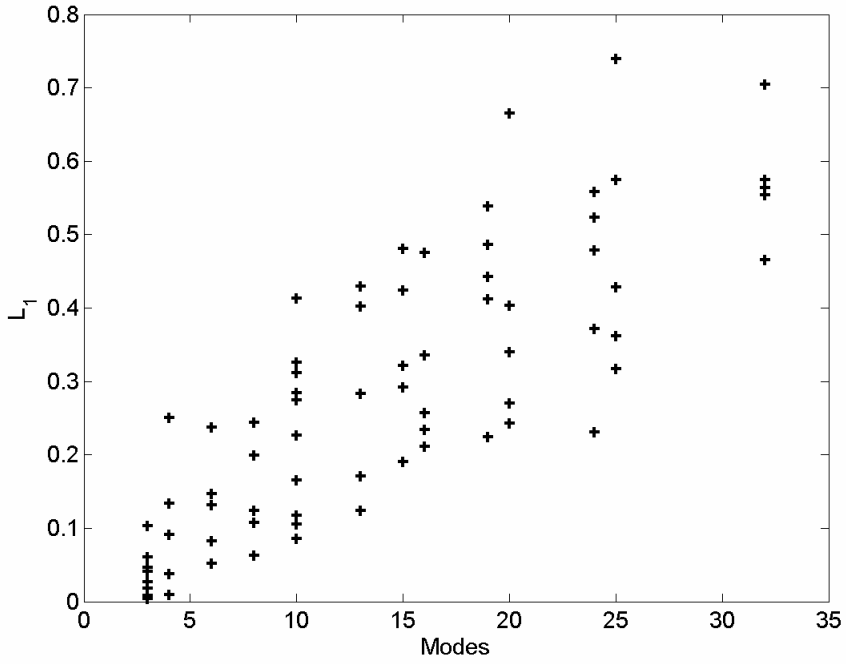

Figure 3.9. . L_1 vs. the number of propagating modes in the Fig. 3.1 sound channels where the channel depth, H, and surface sound speed, c_1, are uncertain with $\langle H \rangle$ = 50 m, $\sigma_H / \langle H \rangle$ = 0.005, $\langle c_1 \rangle$ = 1500 m/s and $\sigma_{c_1} / \langle c_1 \rangle$ = 0.001. All other parameters are as specified in Fig. 3.3.

A sample of three-uncertain-parameter L_1-results is shown in Figure 3.10 for channels having the same uncertainties as in Fig. 3.9, but including the mixed layer depth, d_1, as an additional uncertain parameter with $\langle d_1 \rangle$ = 10 m, and $\sigma_{d_1} / \langle d_1 \rangle$ = 0.01. The frequencies, ranges and receiver depth are identical to Fig. 3.7, and the bottom types are silt and sand with the same properties.

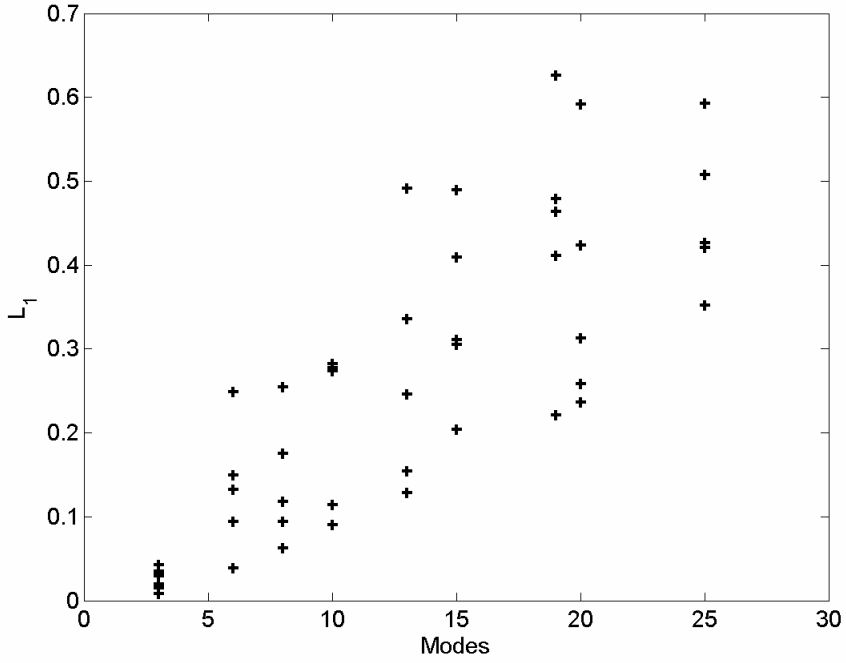

Figure 3.10. Same as Fig. 3.9 except the mixed layer depth, d_1, is also uncertain with $\langle d_1 \rangle$ = 10 m, and $\sigma_{d_1} / \langle d_1 \rangle$ = 0.01. All other parameters are as specified in Fig. 3.3.

The results shown in Figs. 7, 9, and 10 can be condensed to show the overall accuracy of the field shifting technique compared to the simple linear approximation by plotting L_1 from the field shifting technique vs. the L_1 from simple linear fitting. This plot is provided with logarithmic axes as Fig. 3.11 where results from one, two and three uncertain parameters are plotted as pluses, circles, and triangles, respectively. The diagonal line has a slope of unity and indicates where field shifting and simple linear fitting are equally accurate (i.e. they produce equal L_1 values). Results that fall below and to the right of this diagonal line indicate that the field-shifting technique is superior to simple linear fitting. Of the 600 cases plotted in Fig. 11, only 3% are better handled by the simple linear approximation, and for these cases the average difference in L_1 is 0.1.

These results indicate that the spatial-shift-based approximate-PDF technique performs well in an idealized sound channel when compared to the simple linear approximation.

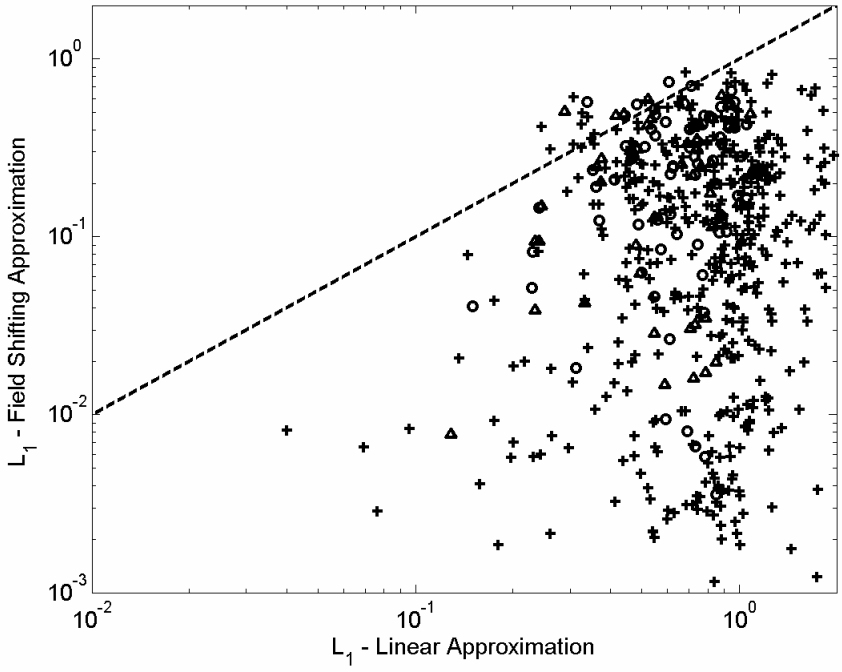

Figure 3.11. Log-log plot of L_1 from the field shifting technique vs. L_1 from simple linear fitting. All previous results from one, two and three uncertain parameters are plotted as pluses, circles, and triangles, respectively. The diagonal line has a slope of one and falls where the field-shifting and linear fitting PDF results are equal. Points below and to the right of this line indicate that the field-shifting technique is superior to simple linear fitting.

The final quantitative comparison provided in Fig. 3.12 is merely a demonstration that the field shifting technique can be successfully applied when all eight parameters specifying the Fig. 3.1 sound channel are uncertain. Here, the sound channel parameters have the same expected values and uncertainties as in Fig. 3.3, except $\sigma_H / \langle H \rangle = 0.0025$, $\sigma_{c_1} / \langle c_1 \rangle = 0.0001$. These two uncertainties were lowered so that all eight parameters contribute significantly to the final amplitude PDF. The L_1 values for the two approximate distributions shown in Fig. 3.12 are 0.12 for the field shifting technique

(dashed curve), and 0.45 for simple linear fitting (dotted curve). The field shifting technique yields errors of 0.4% and 2% for the amplitude mean and standard deviation, respectively, while the linear approximation yields errors of 8% and 19%. Both approximate PDFs are based on nine field calculations while the numerically-converged distribution (solid curve) to which they are compared is based on one million.

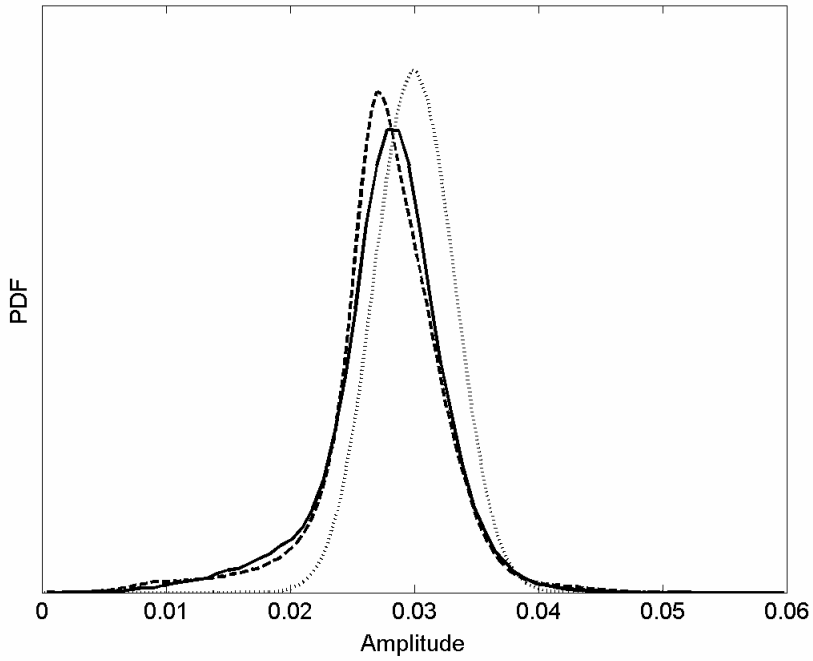

Figure 3.12. Comparison of acoustic amplitude PDFs from field-shifting (dashed line), simple linear fitting (dotted line), and numerically converged direct sampling (solid line) for f = 400 Hz at (r,z) = (6.0 km, 25 m) when all eight parameters of the Fig. 3.1 sound channel are uncertain. All other parameters and uncertainties are as specified in Fig. 3.3, except $\sigma_H / \langle H \rangle$ = 0.0025 and $\sigma_{c_1} / \langle c_1 \rangle$ = 0.0001.

IV. Summary and Conclusions

This paper describes an approximate technique for determining the probability density function (PDF) of acoustic amplitude (A) when the acoustic amplitude is calculated from an acoustic field model having one or more uncertain environmental

parameters as inputs. For N uncertain parameters, the inputs to the technique are the uncertain-parameter PDFs, and N+1 field calculations: one reference calculation without parametric variation and N sensitivity-assessment calculations at close-by values of each uncertain parameter. The technique is based on finding locally optimum spatial shifts between the calculated reference field and each sensitivity-assessment field so that the effects of arbitrary variations in uncertain input parameters can be approximated by easily calculated spatial shifts in the N+1 field calculations. The technique can be used with any suitable acoustic propagation model. It addresses the problem of quantifying acoustic field uncertainty in computational underwater acoustics and offers a less computationally demanding approach than direct numerical sampling or more sophisticated polynomial chaos techniques. This optimum-shift-based approximate-PDF technique was numerically tested in a variety of idealized range-independent shallow-water sound channels, and it appears to be potentially useful based on its relatively high accuracy from relatively few field calculations.

The following (enumerated) conclusions are drawn from this research effort. (1) Given that real time uncertainty analysis may be a valuable asset for sonar-based tactical decision aids, the approximate-PDF technique described here may be fast and accurate enough to be implemented in real time sonar applications. Furthermore, its simplicity may allow it or the optimum-shift concept to be utilized to save computational effort in environmental inversion, especially when nonlinear parametric sensitivity is needed for multiple parameters. (2) When interpreted properly, the L_1 error norm is a useful overall indication of approximate PDF accuracy. Here, L_1 values up to 0.5 indicate converged-to-approximate PDF matching within engineering accuracy; L_1 of 0.5 typically implies up

to two dB error for the standard deviation. (3) The primary limitation of the technique is that at some locations within a sound channel the field variations produced by changes in environmental parameters are not well described by a spatial shift, as stated in Dosso et al. (2007b). However, calculations completed as part of the field shifting technique can reveal when high L_1 is likely. Extension of the field shifting technique to acoustic phase and more geometrically complex environments awaits future research effort.

And, as a final comment, it must be noted that the parameter uncertainties for which the field shifting technique has been developed and tested are relatively small in absolute terms, yet such uncertainties are large enough to produce nonlinearity in the acoustic amplitude vs. uncertain parameter curves. Thus, the lasting contribution from this work may be (7) or (11), the formulae for estimating nonlinear sensitivity to 1 or N parameters from only 2 or $N + 1$ field calculations, respectively. The actual PDF production part of the technique may be less valuable because any acoustic uncertainty calculation that starts from typical ocean environmental parameter uncertainties may return a PDF(A) that is too broad to justify further use of a high-fidelity propagation code. In this circumstance where environmental uncertainties are high, environmental assessment and inversion to reduce the input parameter uncertainties is likely a requisite first step.

Chapter 4

Comparisons of Polynomial Chaos and Field Shifting in a Pekeris Waveguide

I. Introduction

Polynomial Chaos Expansion is a general technique for approximating stochastic processes (Field, 2004) which has been utilized in various fields of engineering research, such as fluid mechanics (Xiu et al., 2002a and 2002b), and heat transfer (Witteveen and Hester, 2008). This technique was first applied to acoustic uncertainty approximation by Steve Finette and other researchers at the Naval Research Laboratory in Washington, D.C. (Finette, 2005, Creamer, 2006). In Finette (2006), this technique is used in an ideal isospeed sound channel with a hard bottom where acoustic propagation is governed by the narrow-angle parabolic approximation to the wave equation to generate moments for the probability of the field. In this chapter, this work is extended to the case of a Pekeris waveguide having a penetrable bottom where acoustic propagation is governed by the Helmholtz equation, to generate approximate field amplitude PDFs. The accuracy and

computational efficiency of these PDF approximations are compared to that of the Field Shifting technique presented in Chaper 3.

II. Deterministic Solution and Direct Simulation

For the Pekeris waveguide shown in Figure 4.1, the deterministic field amplitude can be calculated analytically by solving the Helmholtz equation. Here, only the far-field result will be considered, but leaky modes will be included. For all results in this chapter, a harmonic source of known frequency is assumed.

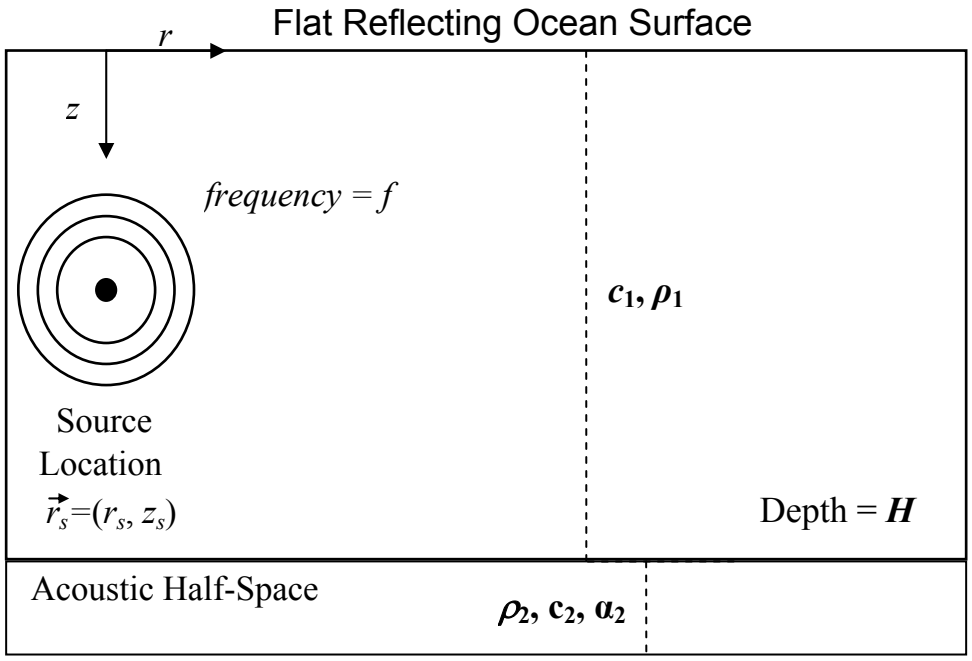

Figure 4.1 – The Pekeris waveguide

The Helmholtz equation governing the acoustic pressure in the sound channel is

$$\left[\frac{1}{r}\frac{\partial}{\partial r}\left(r\frac{\partial}{\partial r}\right)+\frac{\partial^2}{\partial z^2}+k^2\right]P(r,z)=0\,, \tag{1}$$

where $k = k_1$ in the water column, and $k = k_2$ in the bottom. As shown in Kinsler et al. (2000), applying the boundary conditions leads to a transcendental equation for the vertical wavenumbers k_{zm}

$$\tan(k_{zm}H)+\frac{\rho_2}{\rho_1}\frac{k_{zm}}{\sqrt{k_1^2-k_2^2-k_{zm}^2}}=0\,. \tag{2}$$

Using the method of complex effective depth as shown in Zhang and Tindle (1993), the wavenumbers for both propagating and leaky modes in the presence of bottom absorption can be computed analytically. After obtaining the wavenumbers, the pressure field in the water column is given explicitly by

$$P(r,z)=\sqrt{\frac{2\pi}{r}}e^{-i\frac{\pi}{4}}\sum_{m=1}^{M}\frac{1}{\sqrt{k_m}}A_m^2\sin(k_{zm}z)\sin(k_{zm}z_0)e^{ik_m r}\,, \tag{3a}$$

for $k_m r >> 1$ where

$$k_m=\sqrt{k_1^2-k_{zm}^2}\,, \tag{3b}$$

$$A_m^{-2}=\frac{1}{2k_{zm}}\left[k_{zm}H-\cos(k_{zm}H)\sin(k_{zm}H)-\left(\frac{\rho_1^2}{\rho_2^2}\right)\sin^2(k_{zm}H)\tan(k_{zm}H)\right]. \tag{3c}$$

The number of calculated modes used in all subsequent results was set at the lowest M for which $\left|e^{ik_M r}\right|<10^{-3}$. Modes with a higher mode number are assumed to contribute insignificantly to the solution.

The most straightforward technique for obtaining distributions of uncertain field amplitude in the presence of an uncertain sound speed is direct simulation. In this

technique, the deterministic field amplitude (the absolute value of equation 3) is calculated at N_{DS} discrete values of the sound speed, over the range of possible values. In this paper, only sound speeds up to 3 standard deviations lower or higher than the mean are considered. For the reference direct simulation calculations, which represent the nearly exact solution to which other approximation techniques are compared, an N_{DS} of 101 was chosen. The computational cost of direct simulation for one uncertain variable is directly proportional to N_{DS}.

The sensitivity curves vary dramatically in complexity over the range of environments considered. For low frequencies, soft bottoms, short ranges, and small uncertainties in the sound speed, the sensitivity curves are very linear. Figure 4.2 shows the sensitivity curve, and resulting probability density function, for the case of a 100 Hz source, a silt bottom, a sound speed uncertainty of 1 m/s, a receiver range of 4 km, and a receiver depth of 50 m.

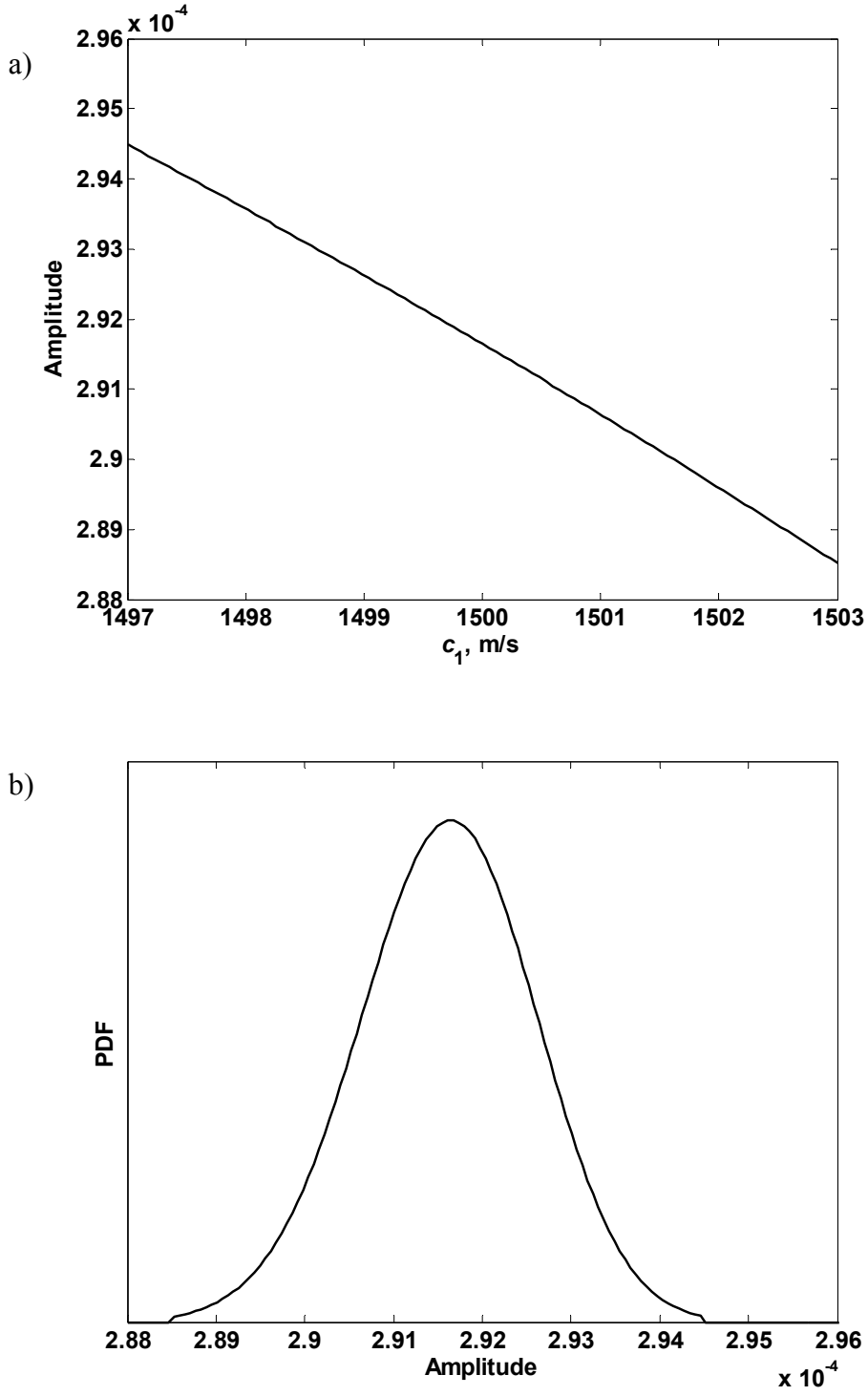

Figure 4.2 Direct Simulation sensitivity curve (a), and PDF (b), for a case with 4 propagating modes and a 1 m/s sound speed uncertainty

Figure 4.3 is the sensitivity curve and corresponding PDF for the case of a 1000 Hz source, a gravel bottom, a sound speed uncertainty of 10 m/s, a receiver range of 10 km, and a receiver depth of 50 m. This curve is notably more complex than its linear counterpart in Figure 4.2, and illustrates the difficulties of accurate sensitivity approximation in cases of long range, high number of propagating modes, and high parameter uncertainty. In practice, however, in situations where the amplitude is as uncertain as in Figure 4.3, precise knowledge of the probability density function may be less necessary or useful, as field predictions in such an environment will be known ahead of time to be highly uncertain.

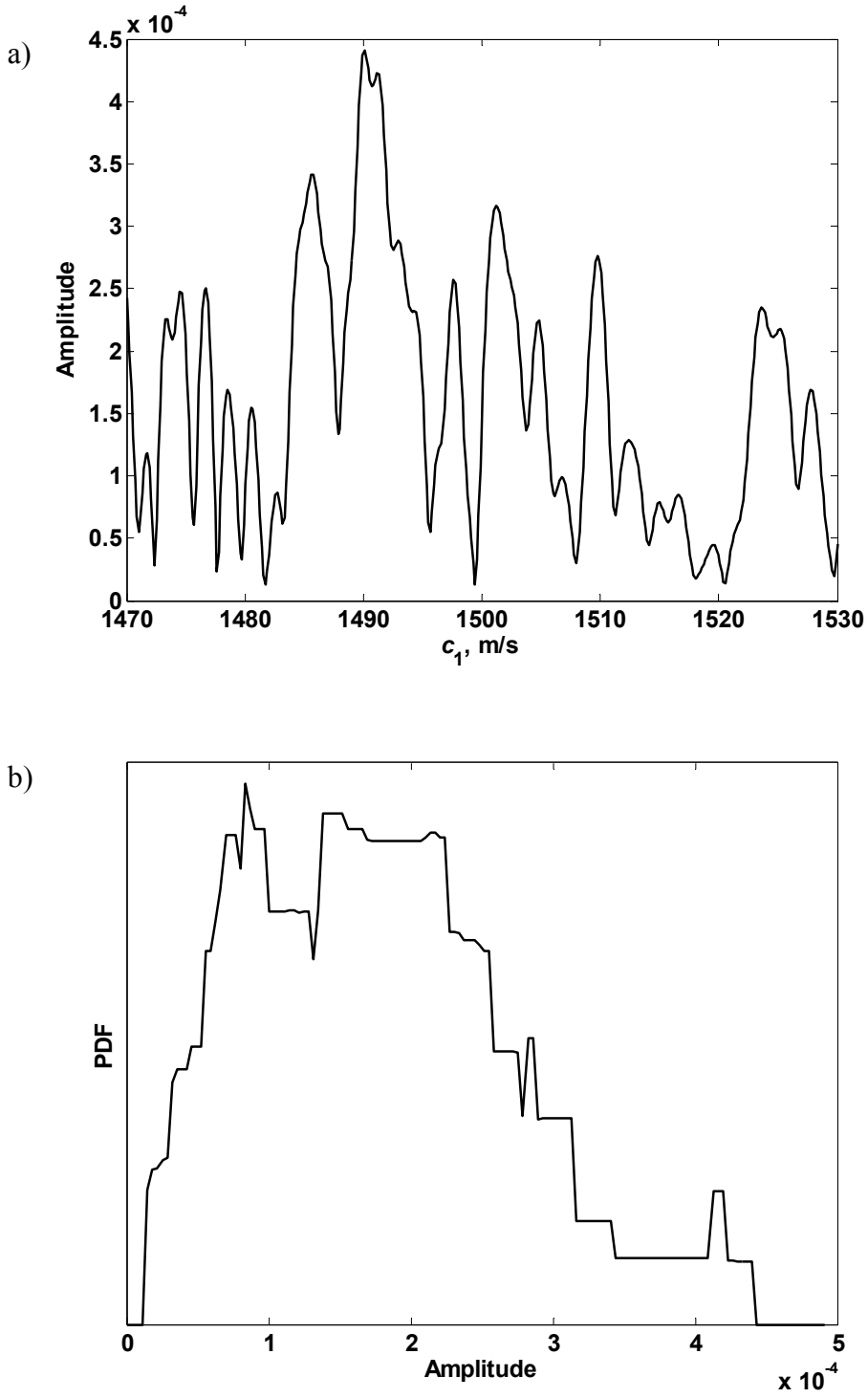

Figure 4.3 Direct Simulation sensitivity curve (a), and PDF (b), for a case with 74 propagating modes and a 10 m/s sound speed uncertainty.

III. Overview of Field Shifting

The field shifting technique utilized here for amplitude approximation in an underwater sound channel is described in detail in Chapter 3. Application to the Pekeris waveguide is straightforward, as the technique is independent of model or sound channel.

The accuracy of the field shifting approximation depends on the accuracy of its assumptions in the sound channel of interest. The accuracy of the first assumption, that changes in the uncertain variable correspond to spatial shifts of the field, can be measured with the mean square error of the optimum shift. This means that when a field shifting approximation is inaccurate due to a failure of this assumption, it is apparent through a calculated quantity, without need to check the accuracy by performing a direct simulation.

The second assumption of field shifting, that spatial shifts are linear with respect to varying sound speed, has no direct test for accuracy within the technique itself. This is a limitation of the fact that only two field calculations are performed to obtain the field shifting solution. Fitting a nonlinear dependence of spatial shift on uncertain input would simply require more field calculations. It will be shown in section V that for a wide range of cases in the sound channel described in Figure 4.1, the assumption of linear shifts yields approximations of acceptable accuracy. It is however worth noting that in certain cases characterized by a low number of propagating modes (3-10), there are receiver locations where spatial shifts with a low mean square error (and thus a high prediction of accuracy) are observed, but the shift varies nonlinearly with c_1, resulting in a poor field shifting approximation to the PDF of acoustic amplitude. For field shifting to be applied robustly to all low-mode cases, more than 2 field calculations may be required.

IV. Overview of Polynomial Chaos Expansion

The application of polynomial chaos expansion for underwater acoustic uncertainty approximation is provided by Finette (2006). Finette also outlines the solution in an ideal waveguide with a constant sound speed and perfectly hard bottom, for a field described by the narrow-angle parabolic approximation to the Helmholtz equation. This technique is modified here for the Pekeris waveguide in Figure 4.1, governed by the exact Helmholtz equation.

As shown in the paper by Finette, the stochastic pressure field in a waveguide with a Gaussian uncertainty in sound speed can be approximated by a weighted sum of scaled Hermite polynomials:

$$P(r,z;\theta) = \sqrt{\frac{2}{\pi r}} e^{-\pi/4} \sum_{q=0}^{\infty} \gamma_q(r,z) He_q(\xi), \tag{4a}$$

$$\xi = \frac{c_1 - \bar{c}_1}{\sigma}. \tag{4b}$$

Here, θ represents a possible outcome in the uncertainty problem, ξ is a zero-mean, Gaussian random variable with unit variance, $\bar{c}_1$ is the mean sound speed in the water column, σ is the standard deviation of c_1, the γ_q are the uncertainty coefficients to be solved for, and the scaled Hermite polynomials *He* are given explicitly by the recursion relation

$$\xi He_n(\xi) = \sqrt{n+1} He_{n+1}(\xi) + \sqrt{n} He_{n-1}(\xi), \qquad He_{-1} = 0, \qquad He_0 = 1 \tag{5}$$

Thus, for the uncertainty problem outlined above, the complete polynomial chaos approximation to the stochastic pressure field amounts to a solution for the coefficients γ_q at some truncated order Q.

Substituting the polynomial chaos expansion for the pressure (equation 4) into the Helmholtz equation, multiplying the result by He_l, and ensemble averaging yields a set of coupled differential equations for the uncertainty coefficients

$$\left[\frac{1}{r}\frac{\partial}{\partial r}\left(r\frac{\partial}{\partial r}\right)+\frac{\partial^2}{\partial z^2}+\left(\frac{\omega}{\bar{c}_1}\right)^2\right]\gamma_l(r,z)-\frac{2\omega^2\sigma}{\bar{c}^3\left\langle He_l^2\right\rangle}\sum_{q=0}^{Q}\gamma_q(r,z)\left\langle He_q\xi He_l\right\rangle=0\,. \tag{6}$$

Using the formulae for the scaled Hermite polynomials in equation 5, and applying the orthogonality condition, the ensemble averages in equation 6 can be computed explicitly, yielding a partial differential recursion equation for the uncertainty coefficients γ

$$\left[\frac{1}{r}\frac{\partial}{\partial r}\left(r\frac{\partial}{\partial r}\right)+\frac{\partial^2}{\partial z^2}+\bar{k}_1^2\right]\gamma_l(r,z)-2\bar{k}^2\frac{\sigma}{\bar{c}}\sqrt{l}\,\gamma_{l-1}(r,z)-2\bar{k}^2\frac{\sigma}{\bar{c}}\sqrt{l+1}\,\gamma_{l+1}(r,z)=0\,, \tag{7}$$

which can be expressed in vector-matrix form as

$$\left[\frac{1}{r}\frac{\partial}{\partial r}\left(r\frac{\partial}{\partial r}\right)+\frac{\partial^2}{\partial z^2}+[A]\right]\boldsymbol{\gamma}(r,z)=0\,. \tag{8}$$

Mirroring Finette's solution for the ideal waveguide, this equation can be solved by diagonalizing the coupling matrix [A]. Define the eigenvector matrix associated with [A] as $[G]=[\{\mathbf{g_1}\},\{\mathbf{g_2}\}...]$. Multiplying equation 8 by [G]$^{-1}$ yields an uncoupled differential equation for the transformed uncertainty coefficients $\hat{\boldsymbol{\gamma}}=[G]^{-1}\boldsymbol{\gamma}$

$$\left[\frac{1}{r}\frac{\partial}{\partial r}\left(r\frac{\partial}{\partial r}\right)+\frac{\partial^2}{\partial z^2}+[G]^{-1}[A][G]\right]\hat{\boldsymbol{\gamma}}(r,z)=0\,. \tag{9}$$

The diagonal matrix $[G]^{-1}[A][G]$ contains the eigenvalues λ_l of [A]. Thus the lth transformed uncertainty coefficient satisfies a differential equation of the form

$$\left[\frac{1}{r}\frac{\partial}{\partial r}\left(r\frac{\partial}{\partial r}\right)+\frac{\partial^2}{\partial z^2}+\lambda_l\right]\hat{\gamma}_l(r,z)=0\,. \tag{10}$$

This is simply the familiar deterministic Helmholtz equation, with λ_l taking the place of k^2. Furthermore, by the properties of the coupling matrix [A] in this sound channel, the eigenvalues λ_l are actually centered about the mean value of k_1^2. The solution for each coefficient mirrors the deterministic solution provided in equation 3:

$$\hat{\gamma}_l(r,z)=C_l\sum_{m=1}^{M}A_{ml}^2\sin(k_{zml}z)\sin(k_{zml}z_0)e^{ir\sqrt{\lambda_l-k_{zml}^2}}\,. \tag{11}$$

The coefficient C_l is determined from the initial condition, by first multiplying equation 11 by the eigenvector matrix G, and inserting this into the expression for $P(0,z)$:

$$\sum_{l=1}^{Q}He_l(\xi)\left[\sum_{u=1}^{Q}g_{lu}\left\{C_u\sum_{m=1}^{M}A_{mu}^2\sin(k_{zmu}z)\sin(k_{zmu}z_0)\right\}\right]=\delta(z-z_0)\,. \tag{12}$$

Multiplying the equation by He_r and ensemble averaging yields

$$\sum_{u=1}^{Q}g_{ru}C_u\sum_{m=1}^{M}A_{mu}^2\sin(k_{zmu}z)\sin(k_{zmu}z_0)=\delta(z-z_0)\delta_{r0}\,. \tag{13}$$

Here, δ_{r0} is unity when index r = 0, and zero otherwise. Integrating over the waveguide depth, and applying the orthonormality of the modes yields

$$\sum_{u=1}^{Q}g_{ru}C_u=\delta_{r0}\,. \tag{14}$$

Multiplying this by the inverse eigenvector matrix yields the coefficients C_u in closed form

$$C_u=a_{u1}\,, \tag{15}$$

where a_{u1} is the uth element of the inverse of the first eigenvector. Thus, the full solution for the transformed uncertainty coefficient is

$$\hat{\gamma}_l(r,z) = a_{l1}\sum_{m=1}^{M} A_{mu}^2 \sin(k_{zmu} z)\sin(k_{zmu} z_0) e^{ir\sqrt{\lambda_l - k_{zml}^2}} \tag{16}$$

For this sound channel, each transformed uncertainty coefficient is equivalent to the deterministic pressure when $k_1 = \sqrt{\lambda_l}$, scaled by the quantity $a_{l1}\sqrt{\frac{r}{2\pi}}e^{i\frac{\pi}{4}}$. The amplitudes of these transformed uncertainty coefficients are plotted as circles vs. $\omega/\sqrt{\lambda_l}$ for an example case of Q = 40 in Figure 4.4, with a_{l1} divided out. The solid line is the exact sensitivity curve for field amplitude with respect to sound speed, scaled by $\sqrt{\frac{r}{2\pi}}$. It is clear that each transformed uncertainty coefficient of index l corresponds to a sample of the sensitivity curve. The further weighting of each coefficient by a_{l1} effectively lowers the relative contribution of coefficients corresponding to k_1 values further from the mean.

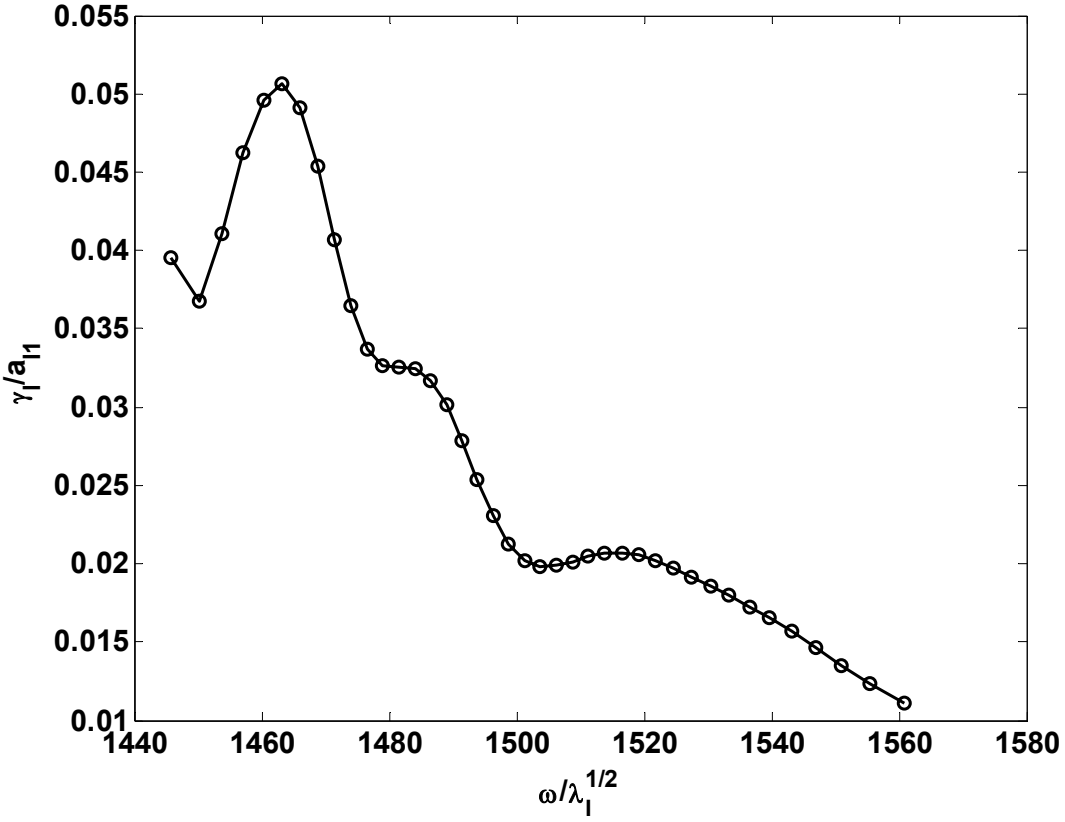

Figure 4.4. Scaled transformed uncertainty coefficients vs. $\omega/\sqrt{\lambda_l}$

Multiplying these transformed coefficients by the eigenvector matrix and inserting the result into equation 4, the full stochastic pressure field is given by

$$P(r,z;\theta) = \sqrt{\frac{2}{\pi r}} e^{-\pi/4} \sum_{q=0}^{Q} \left[\sum_{l=0}^{Q} g_{ql} \hat{\gamma}_l(r,z) \right] He_q(\xi). \tag{17}$$

Using the definition of ξ as a normal random variable representing the uncertainty in sound speed, we can obtain an explicit expression for $P(r, z; c_1)$ – the pressure field as a function of the uncertain sound speed:

$$P(r,z;c_1) = \sqrt{\frac{2}{\pi r}} e^{-\pi/4} \sum_{q=0}^{Q} \left[\sum_{l=0}^{Q} g_{ql} \hat{\gamma}_l(r,z) \right] He_q\left(\frac{c_1 - \bar{c}_1}{\sigma} \right). \tag{18}$$

The polynomial chaos expansion is truncated at a finite order, Q. The accuracy of the solution is highly dependent on the chosen Q, and does not increase monotonically with increasing Q. To illustrate the relationship between accuracy and Q, Figure 4.5 shows two plots of the uncertainty coefficients $|\gamma_l|$ vs. l in an example sound channel for two different values of Q. Figure 4.6 shows the corresponding sensitivity curves for each value of Q, generated using equation 18, as well as the direct simulation result for comparison. The coefficients have a peak magnitude at some l, and decrease in magnitude as l increases or decreases. The accuracy of the approximation corresponding to each Q increases as the magnitude of the highest order uncertainty coefficient decreases with respect to the peak value.

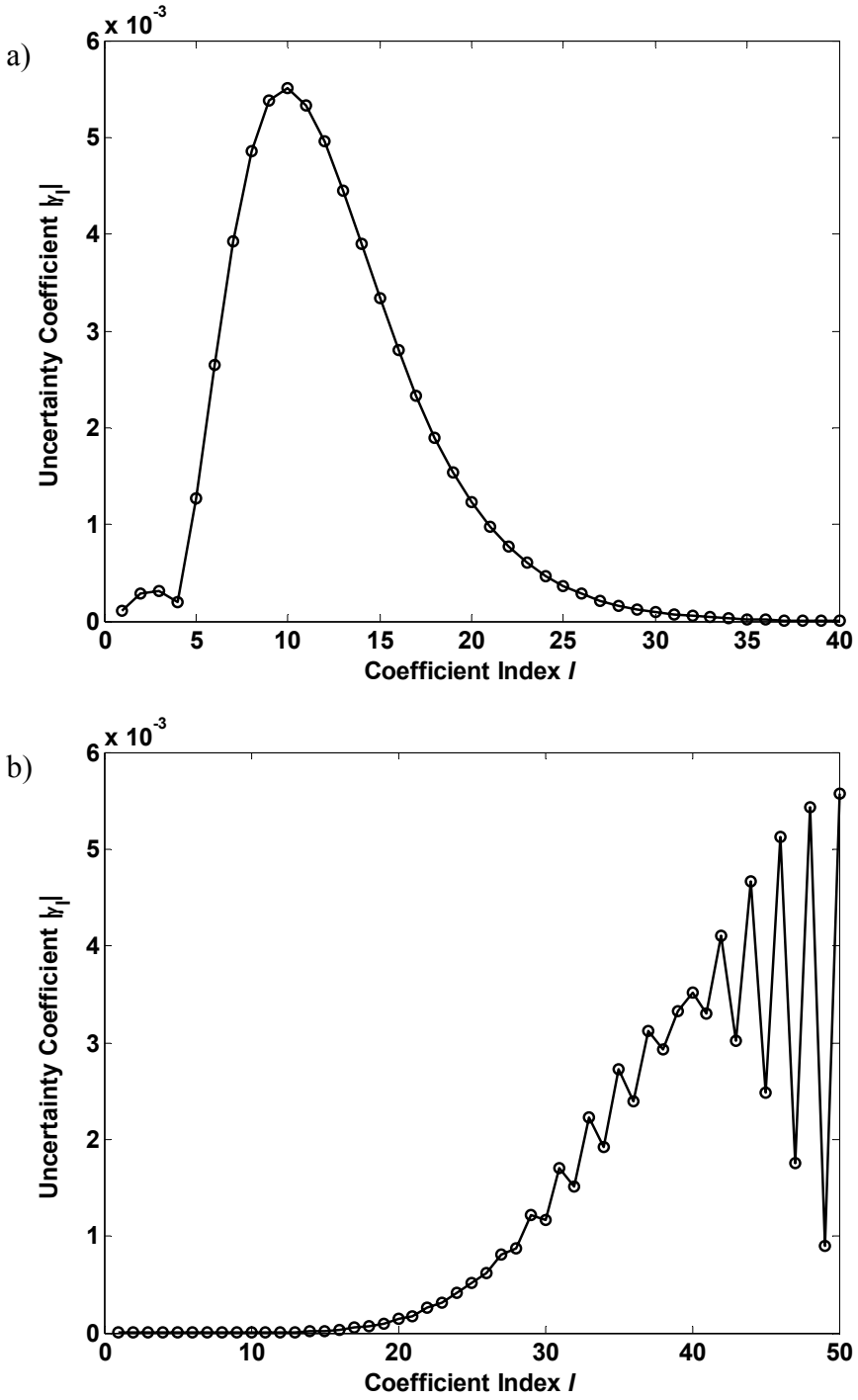

Figure 4.5 – Uncertainty coefficients vs. coefficient index *l* for a) Q = 40, b) Q= 50

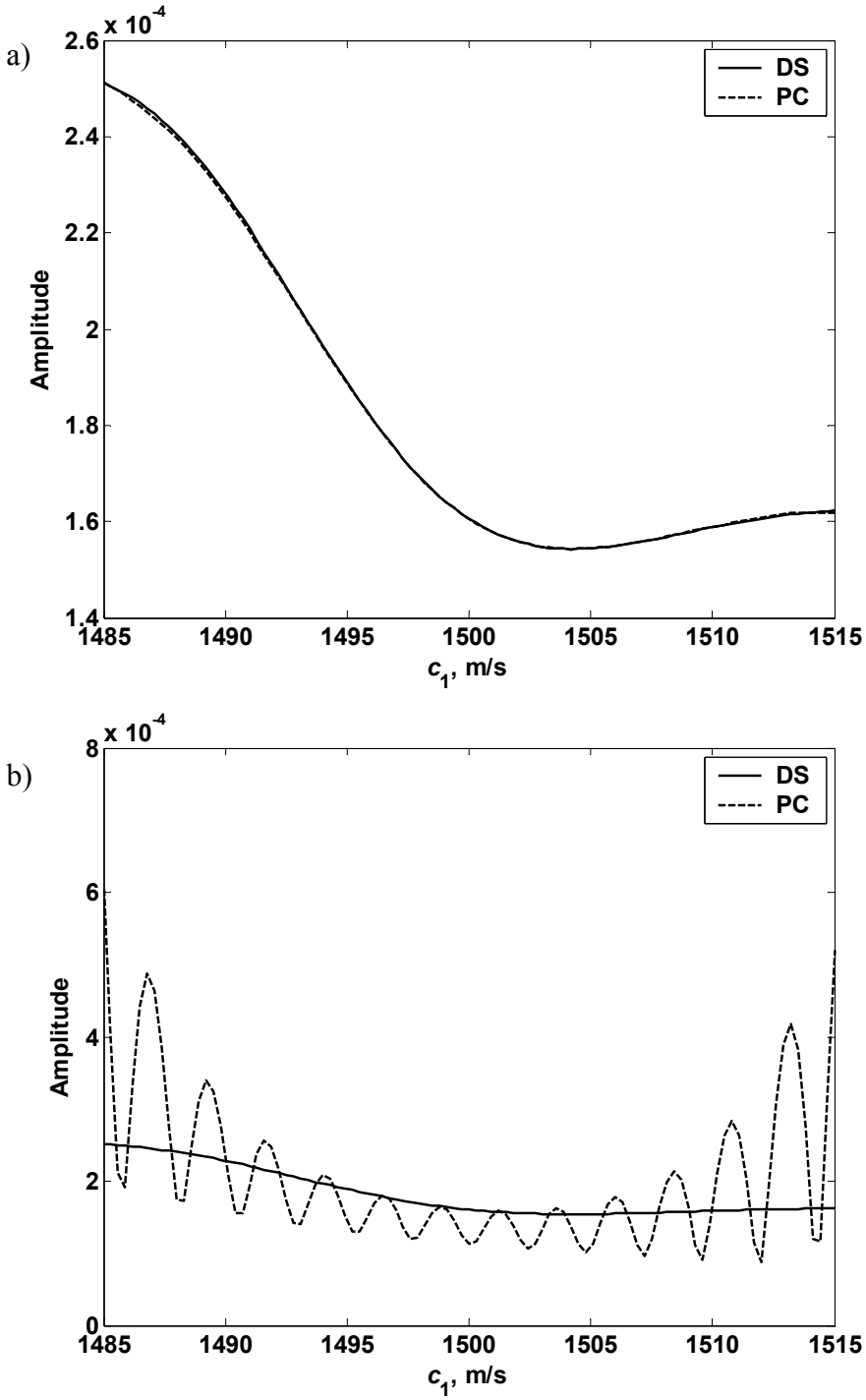

Figure 4.6 – Amplitude sensitivity curves for polynomial chaos (dashed) and direct simulation (solid), for a) Q = 40, b) Q= 50

This can be quantified by defining a quantity β,

$$\beta = \frac{\left|\gamma_Q\right|}{\left|\gamma_l\right|_{\max}}, \tag{19}$$

as the ratio of the magnitude of the highest order uncertainty coefficient (order Q) to the magnitude of the largest uncertainty coefficient. When this value approaches unity, the resulting approximation is highly inaccurate, and can contain many oscillatory artifacts. As this value decreases, the accuracy of the approximation increases.

This measure of accuracy is plotted vs. Q for an example case, shown in Figure 4.7. There is an oscillatory dependence of accuracy on Q. The exact behavior of this curve depends on all of the environmental inputs, as well as the receiver location. Thus, for a given sound channel, there is no fixed value of Q which ensures accuracy for all receiver locations; rather it is necessary to select an appropriate value of Q for each situation.

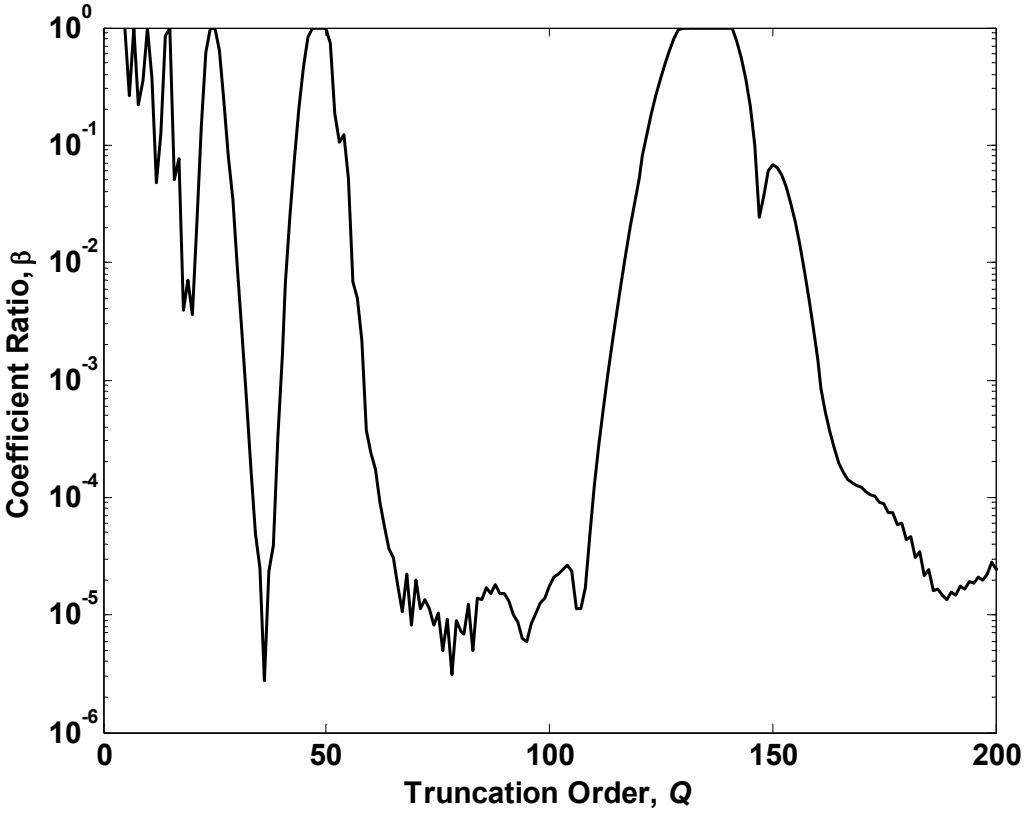

Figure 4.7 Coefficient ratio β vs. truncation order Q.

It is worth mentioning that this parameter β is useful as an internal predictor of accuracy for the polynomial chaos technique with regards to truncation error. If Q has been chosen poorly for a particular problem, such that truncation error is high, this is immediately apparent in the high value of the quantity β, which comes directly from quantities computed within the polynomial chaos technique.

V. Comparisons of Accuracy and Efficiency

The previous sections outlined the procedure for obtaining field amplitude as a function of sound speed in the water column for the direct simulation, field shifting, and polynomial chaos techniques. As described in Chapter 3, such sensitivity curves can be transformed to PDFs, and the accuracy of the approximate PDFs measured with respect to the reference PDF (obtained by direct simulation) with the L_1 error norm. The lower the value of L_1, the higher the accuracy of the PDF approximation, with values of L_1 below 0.5 corresponding to an acceptable degree of accuracy for many applications.

For comparison, results are first presented for the case of a direct simulation approximation. This approximation is obtained by using a smaller number of field calculations than the reference curve, and interpolating linearly to generate an approximate PDF. Figures 4.8 through 4.10 display the L_1 error of a direct simulation approximation using 21 field calculations, over a wide range of environmental inputs and receiver locations. The three bottom types considered are silt, sand, and gravel, with sound speed, density, and absorptivity values obtained from Table 1.3 in Jensen et al. (1994). The frequency is varied from 100 Hz to 1 kHz, receiver range from 1 km to 10 km, and receiver depths of 30 m, 50 m, and 80 m. The mean water column sound speed

for all cases is 1500 m/s, with a standard deviation of 1 m/s in Figure 4.8, 5 m/s in Figure 4.9, and 10 m/s in Figure 4.10.

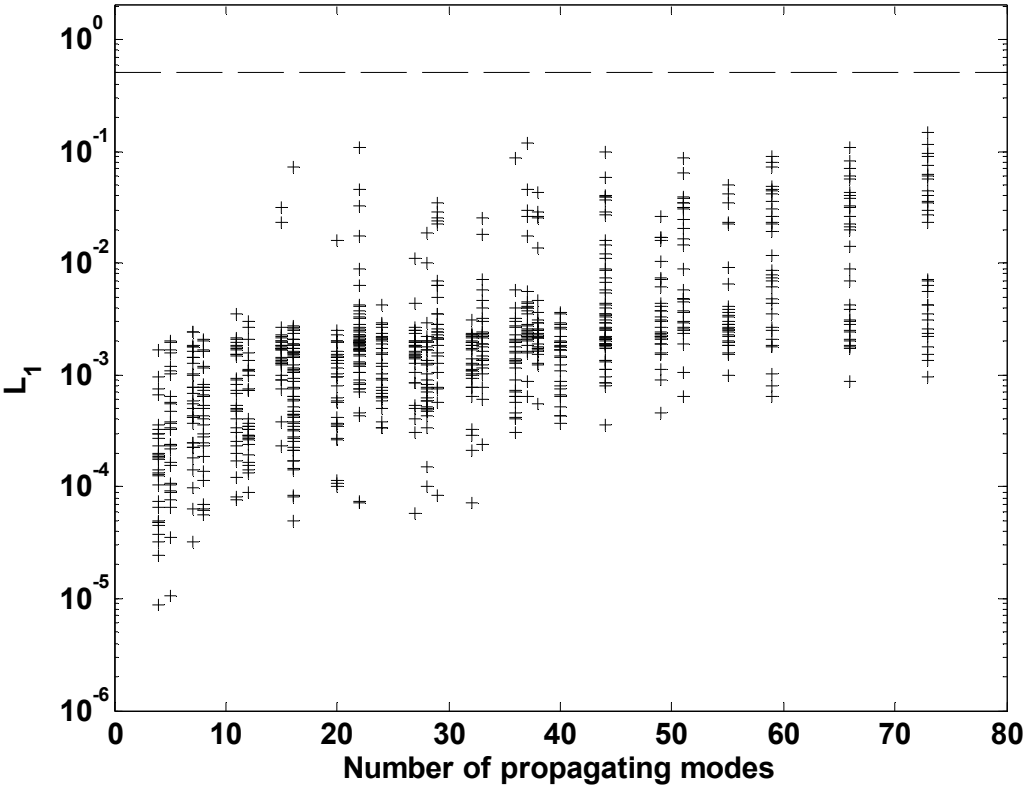

Figure 4.8. L_1 values for direct simulation at 1 m/s sound speed uncertainty. 21 field calculations were used in the approximation. The dashed line corresponds to an L_1 of 0.5. The reference PDF in each case involves 101 field calculations.

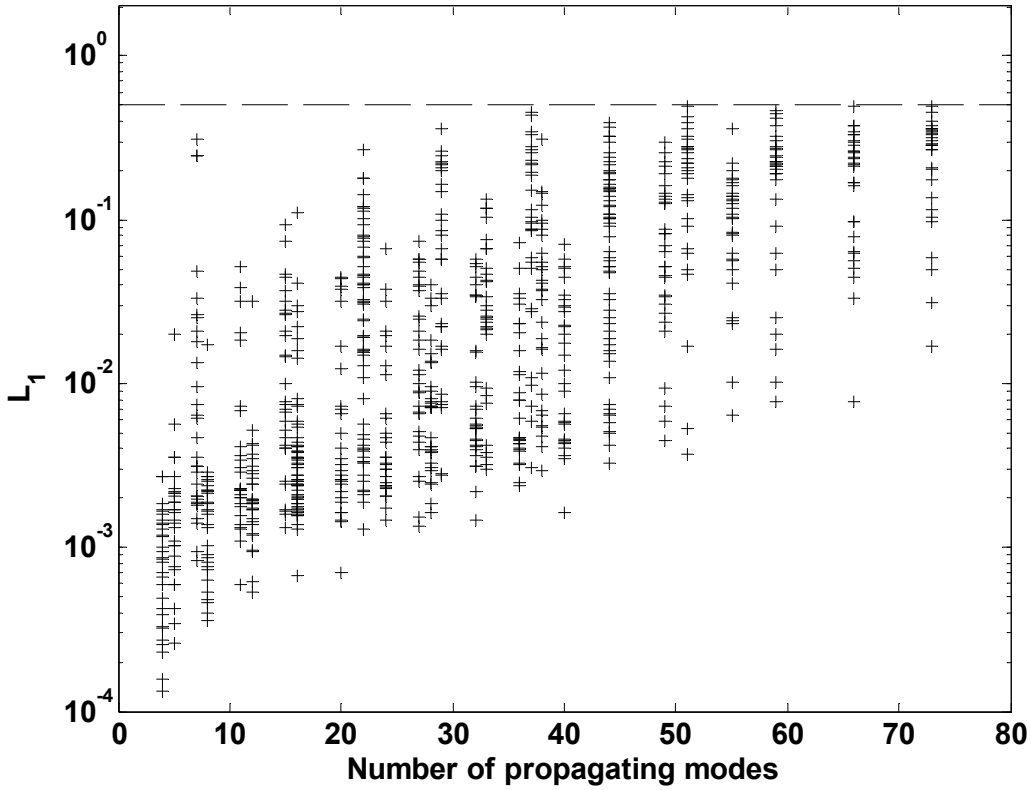

Figure 4.9. L_1 values for direct simulation at 5 m/s sound speed uncertainty. Again 21 field calculations were used in the approximation. The dashed line corresponds to an L_1 of 0.5.

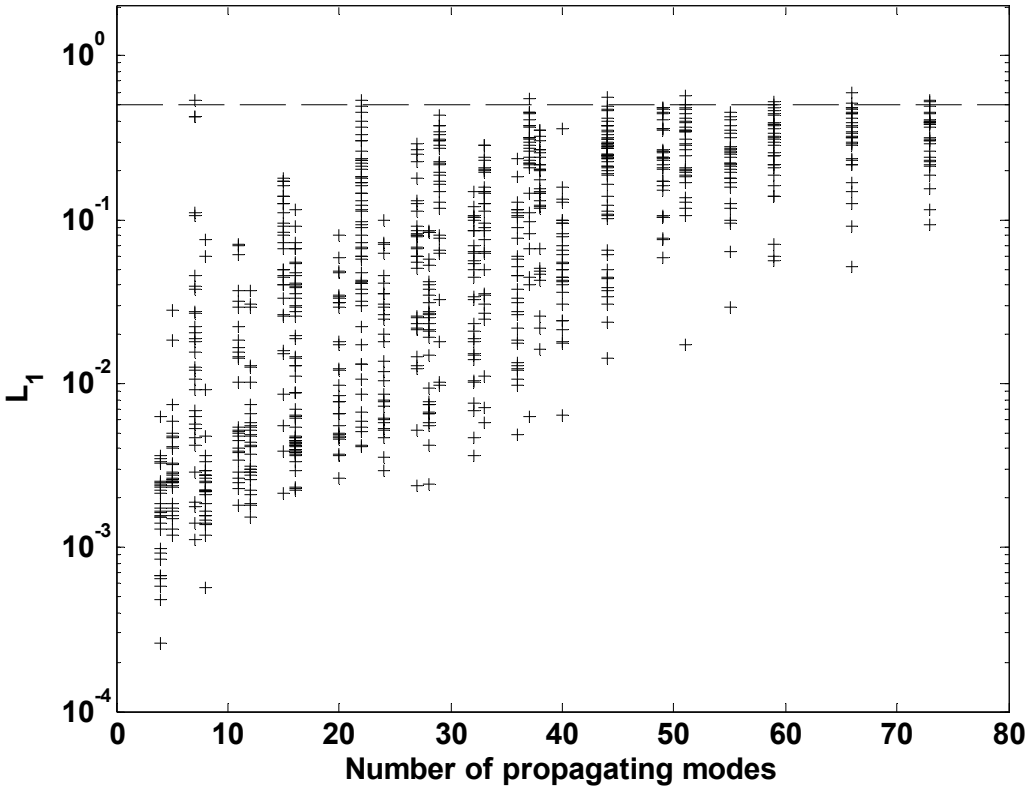

Figure 4.10. L_1 values for direct simulation at 10 m/s sound speed uncertainty. Again 21 field calculations were used in the approximation. The dashed line corresponds to an L_1 of 0.5.

As seen in the figures above, as the number of propagating modes increases, or the uncertainty in sound speed increases, the lower limit of the L_1 error increases as well. This is due to the fact that as the sensitivity curve becomes more complicated 21 sample points yields a less accurate approximation of the relationship between amplitude and sound speed. This is also apparent from Figures 4.2 and 4.3, where linear interpolation between 21 sample points would provide a far more accurate approximation to the curve corresponding to 4 propagating modes and a 1 m/s sound speed uncertainty (Figure 4.2) than the case of 74 propagating modes and 10 m/s sound speed uncertainty (Figure 4.3).

L_1 values for the field shifting technique, over the same range of environmental inputs and receiver locations used in Figures 4.8 though 4.10, are provided in Figures 4.11 through 4.13. As noted in Chapter 3, these field shifting approximations utilize only 2 field calculations, in contrast to the 21 field calculations of the direct simulation approximation above, or the 101 field calculations of the direct simulation reference curves.

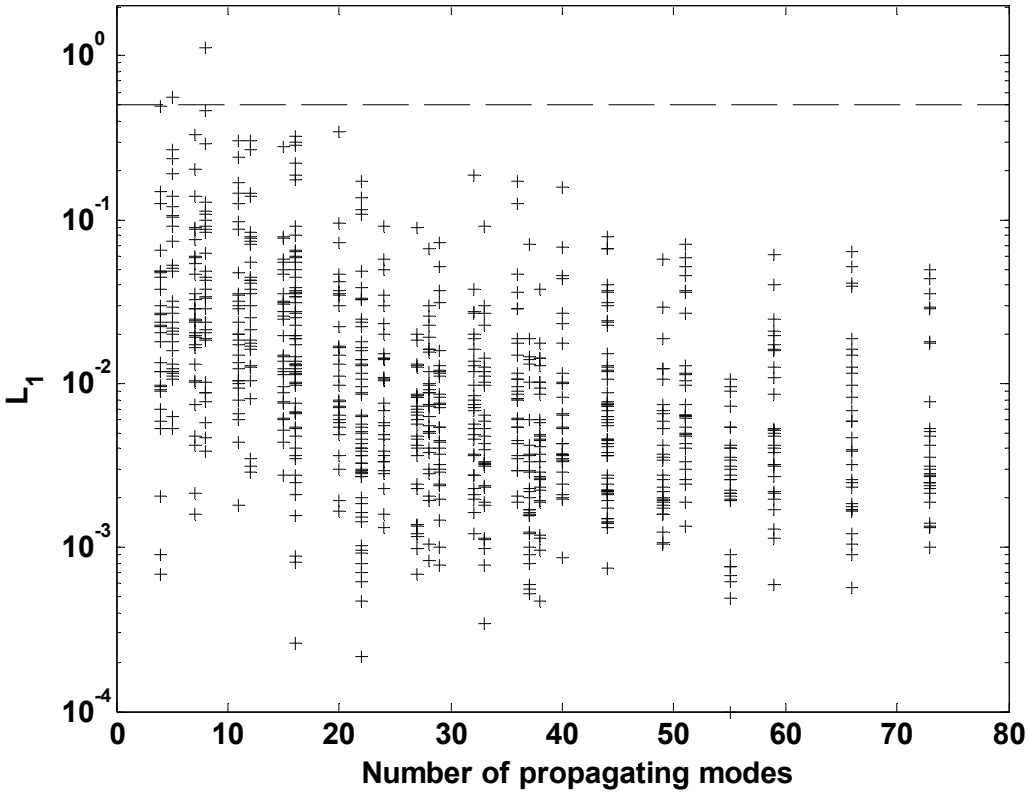

Figure 4.11. L_1 values for Field Shifting, 1 m/s sound speed uncertainty. The dashed line corresponds to an L_1 of 0.5.

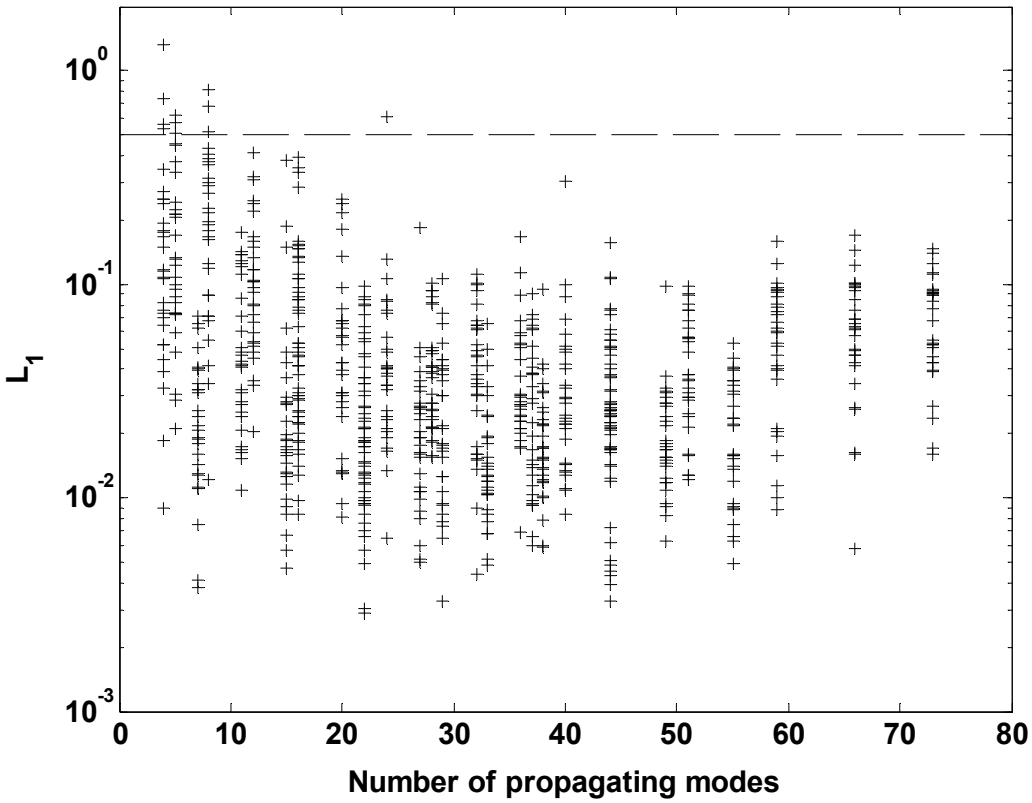

Figure 4.12. L_1 values for Field Shifting, 5 m/s sound speed uncertainty. The dashed line corresponds to an L_1 of 0.5.

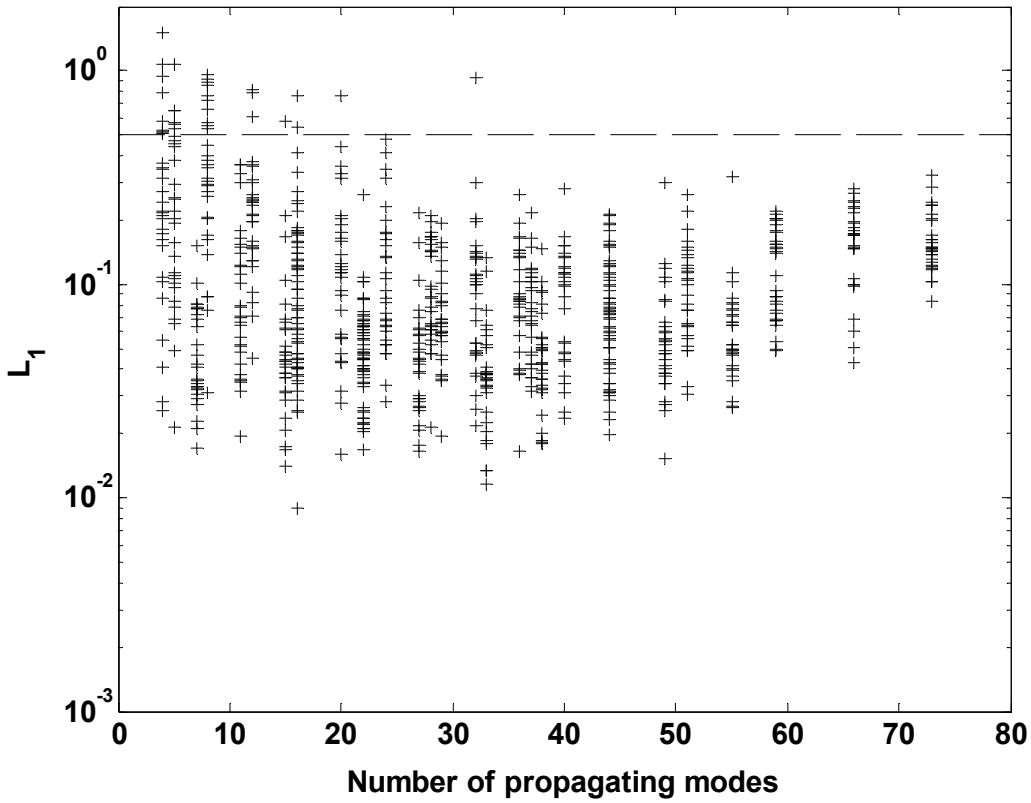

Figure 4.13. L_1 values for Field Shifting, 10 m/s sound speed uncertainty. The dashed line corresponds to an L_1 of 0.5.

For the cases in Figure 4.11, with a sound speed uncertainty of 1 m/s, 95% of the field shifting L_1 values fall below 0.10. As discussed in section III, there are higher values of L_1 which correspond to cases of low propagating mode number, where the assumption of linear shifts fails. There are also cases of higher L_1 at higher propagating mode number, which correspond to poor quality shifts. The lower accuracy of these latter cases is well predicted by the higher RMS error of the shift in the field shifting calculation.

For the 5 m/s standard deviation cases in Figure 4.12, 95% of the L_1 values fall below 0.24. In Figure 4.13, 95% of the L_1 values fall below 0.40. It is clear from this trend that in general, the accuracy of field shifting decreases with increasing uncertainty. Although this is the dominating trend, due to the nature of the sensitivity approximations and the definition of L_1 there are individual cases where the L_1 is actually lower at a higher value of uncertainty.

As seen in each of Figures 4.11 through 4.13, unlike the direct simulation approximation, the accuracy of field shifting does not always decrease as the complexity of the sensitivity curve increases due to a higher number of propagating modes, for the environments considered. At a fixed value of sound speed uncertainty, the lower and upper bounds of accuracy for the field shifting technique are fairly constant over a wide range of environmental inputs and frequencies.

Figure 4.14 plots the L_1 error of the field shifting technique vs. the L_1 error of the 21-point direct simulation approximation, for the 10 m/s uncertainty cases of Figures 4.10 and 4.13. The dashed lines correspond to an L_1 of 0.5 for each technique. The dotted line indicates the line of equivalent accuracy of the two techniques. Points to the left of the

dotted line correspond to cases for which the 21-point direct simulation approximation is more accurate than the field shifting approximation. Points to the right of the dotted line correspond to cases where the field shifting approximation is more accurate. Here, field shifting is more accurate in 50% of the 300 cases plotted, for just under 10% of the computational cost in terms of field calculations.

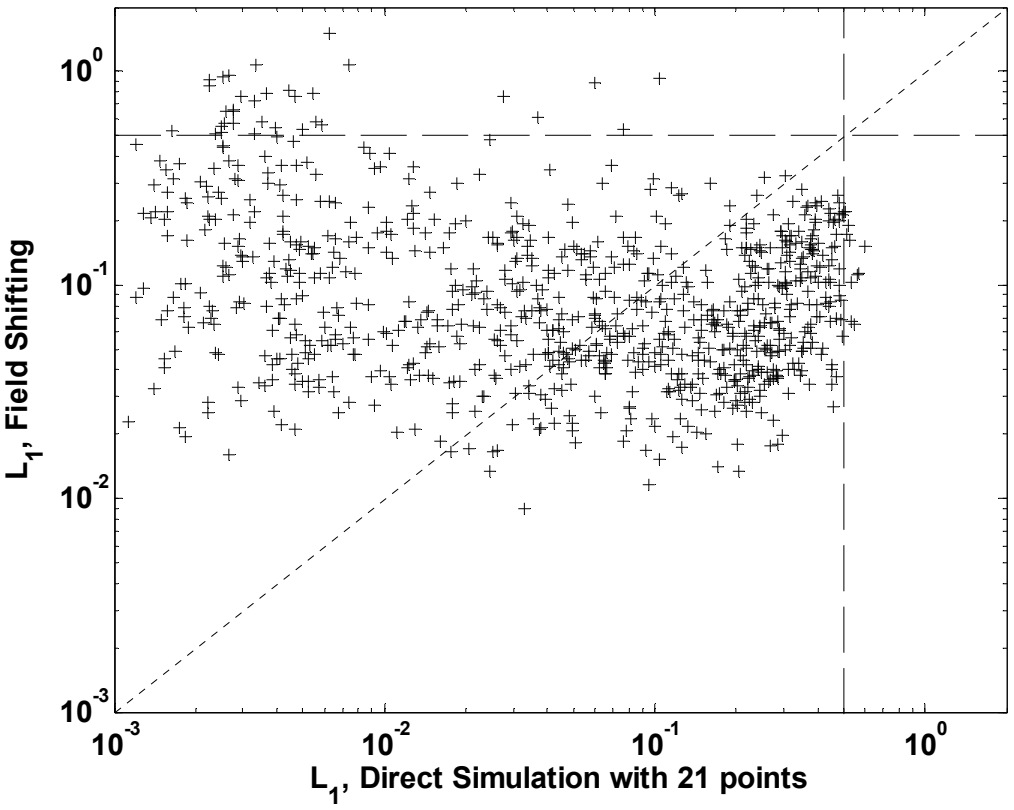

Figure 4.14. L_1 error of field shifting vs. L_1 error of 21-point direct simulation, for the case of 10 m/s sound speed uncertainty. The dashed lines correspond to an L_1 of 0.5 for each technique. The dotted line indicates equal accuracy of the two techniques.

As discussed in section IV, the accuracy of the polynomial chaos approximation is highly dependent on the choice of truncation order, Q. In addition, for the case of a single uncertain variable, Q directly corresponds to the number of field calculations required to obtain a PDF approximation. If the accuracy of the 21-point direct simulation approximation (shown in Figures 4.8-4.10) is considered sufficient for an acoustic prediction application, then the computational cost of an alternative approximation technique must be lower than this to have greater utility. For comparison, Figures 4.15 through 4.17 provide the L_1 errors of the polynomial chaos approximation when Q is fixed at 21.

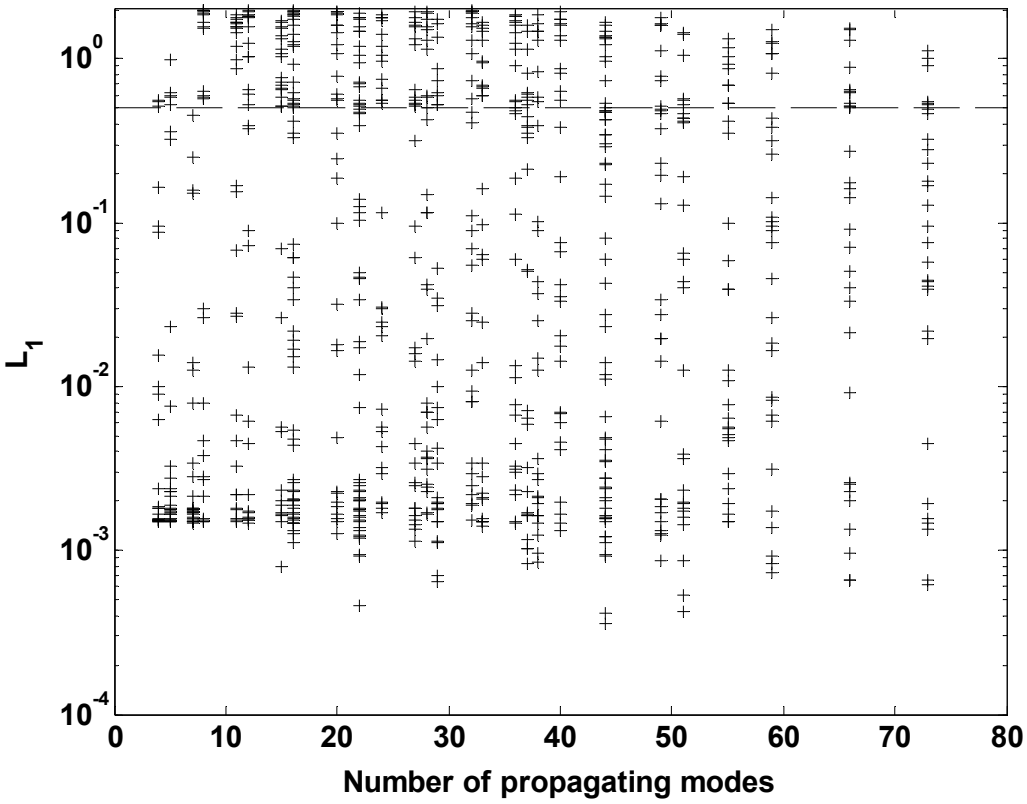

Figure 4.15. L_1 values for polynomial chaos at 1 m/s uncertainty in sound speed, when Q is fixed at 21.

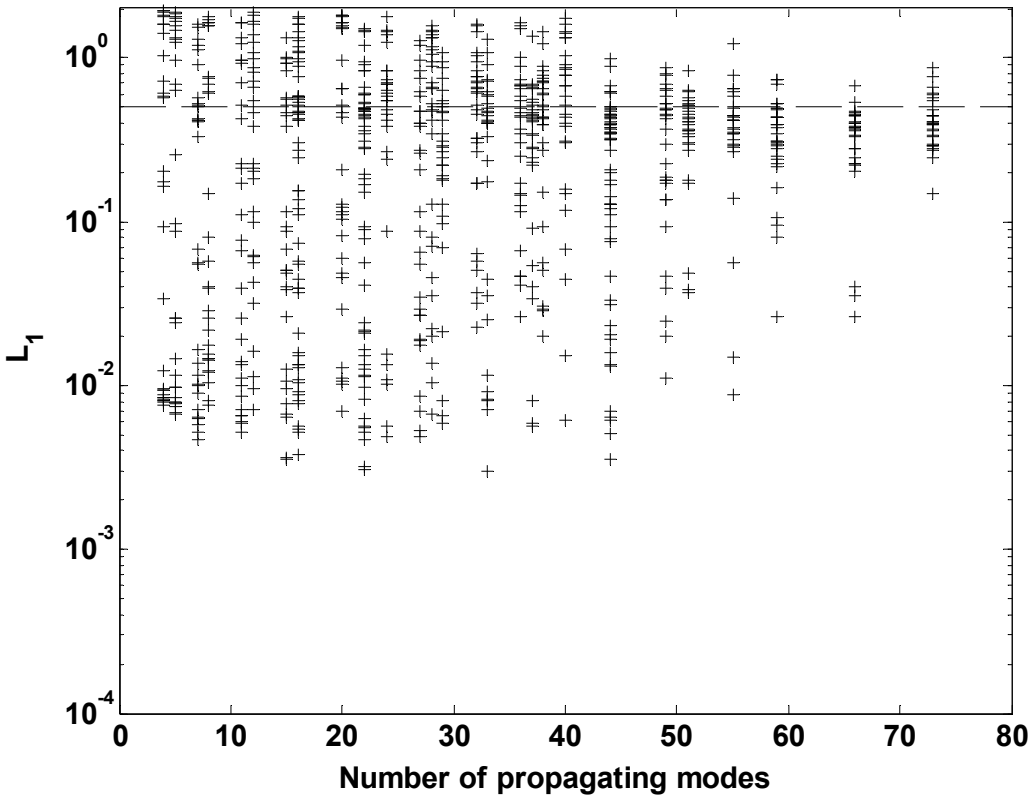

Figure 4.16. L_1 values for polynomial chaos at 5 m/s uncertainty in sound speed, when Q is fixed at 21.

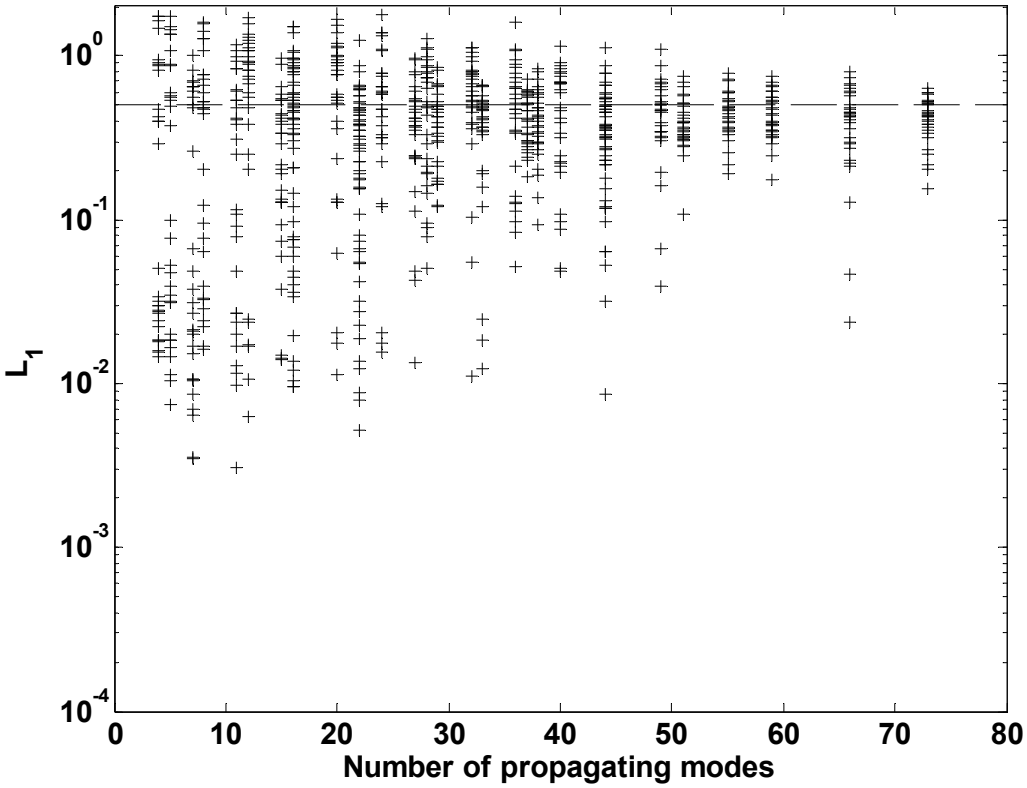

Figure 4.17. L_1 values for polynomial chaos at 10 m/s uncertainty in sound speed, when Q is fixed at 21.

When compared to Figs. 4.8-4.10 for direct simulations and 4.11-4.13 for field shifting, Figures 4.15-4.17 show that for a simple Perkeris waveguide a blanket choice of Q = 21 in the polynomial chaos expansion technique produces worse results that either of the other techniques. This point is further illustrated in Figure 4.18 which presents the L_1 values for the polynomial chaos approximation (with Q=21) vs. the L_1 values for the 21-point direct simulation approximation at a sound speed uncertainty of 10 m/s, analogous to Figure 4.14 for field shifting. For the case of a single uncertain variable, these two approximations have the same computational cost in terms of field calculations (though polynomial chaos involves additional computational operations, these are considered to be much less computationally expensive than the field calculation steps). For 87% of the cases plotted, the 21-point direct simulation approximation is more accurate than the polynomial chaos approximation with a fixed Q of 21.

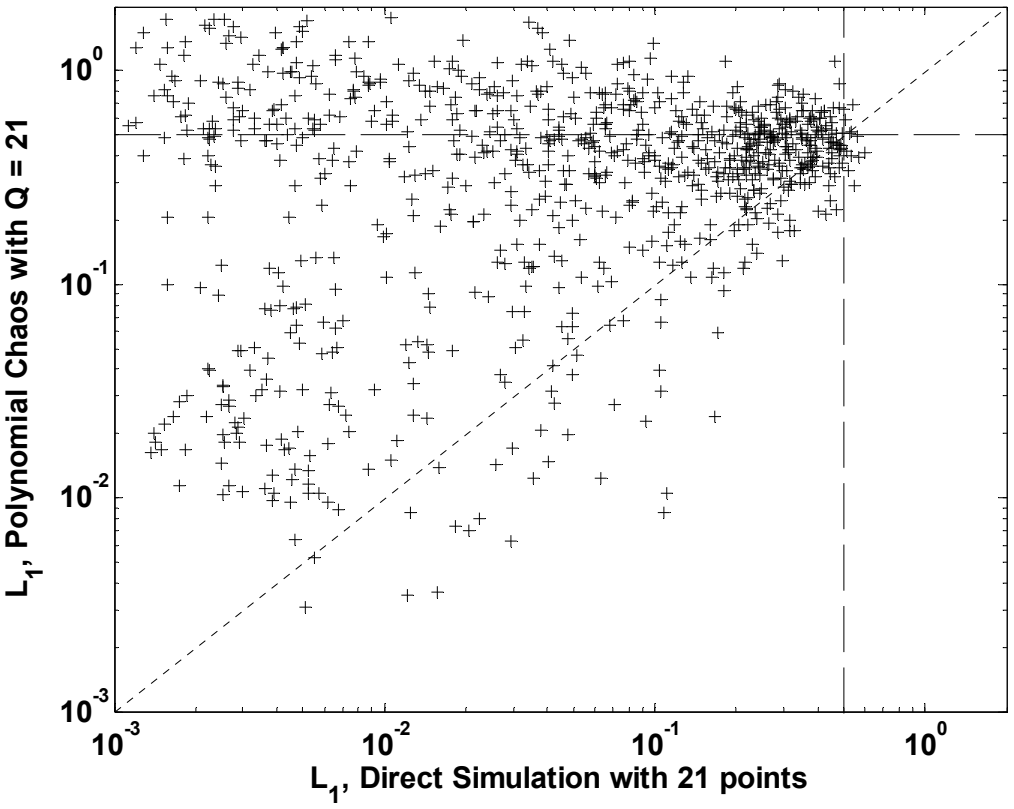

Figure 4.18. L_1 error of polynomial chaos with Q=21 vs. L_1 error of 21-point direct simulation, for the case of 10 m/s sound speed uncertainty. The dashed lines correspond to an L_1 of 0.5 for each technique. The dotted line indicates equal accuracy of the two techniques.

It is apparent from the large scatter in L_1 values in Figs. 4.15-18 that selecting a low, fixed value for Q does not result in accurate PCE uncertainty approximations for a wide range of environmental parameters. This is consistent with the results shown in Figure 4.7, where it is apparent that the accuracy of the polynomial chaos approximation (as predicted by the uncertainty coefficient ratio β) varies cyclically with truncation order Q. At a fixed value of Q, some environmental inputs or receiver locations will yield low values of β, and thus high accuracy, while others correspond to high values of β, and low approximation accuracy.

This is illustrated in Figure 4.19, which plots L_1 error vs. coefficient ratio β for the 10 m/s uncertainty cases in Figure 4.18. As β increases, the L_1 error of the corresponding approximation increases as well. The dashed line indicates a β of 3×10^{-3}. As approximations with β values below this threshold exhibit minimal truncation error, such a threshold can be used as a requirement for an accurate selection of Q.

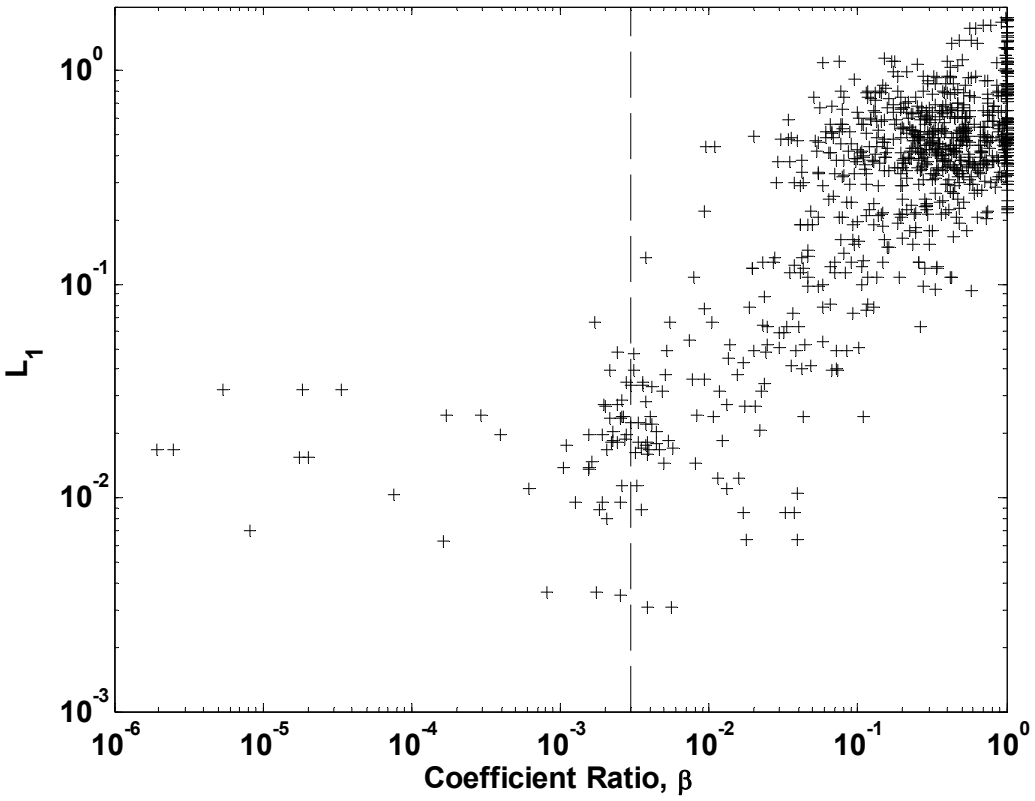

Figure 4.19. L_1 error vs. coefficient ratio β for the polynomial chaos approximation with $Q = 21$, at a 10 m/s sound speed uncertainty. The dashed line corresponds to a β of $3\text{x}10^{-3}$, a threshold below which truncation error can be considered small.

There are no existing techniques for predicting an accurate truncation order based on the values of environmental inputs and receiver locations, though these may arise from further research into polynomial chaos expansion. At present, any "optimum" value for Q must be found iteratively.

Figure 4.20 shows the L_1 values for the polynomial chaos technique when Q is chosen iteratively. For each of the cases plotted, Q is set at a starting value of 10, and the resulting coefficient ratio β calculated. If the resulting β is below the threshold $3\text{x}10^{-3}$, this Q corresponds to a low truncation error, and the calculation is terminated. If β is above this threshold, Q is increased by 1, and the calculation repeated as necessary. Thus, the value of Q used for each approximation in Figure 4.20 represents the lowest value of Q for which the coefficient ratio meets the required threshold.

Figure 4.21 shows the optimum values for Q corresponding to the approximations in Figure 4.20, determined through the iterative technique outlined above.

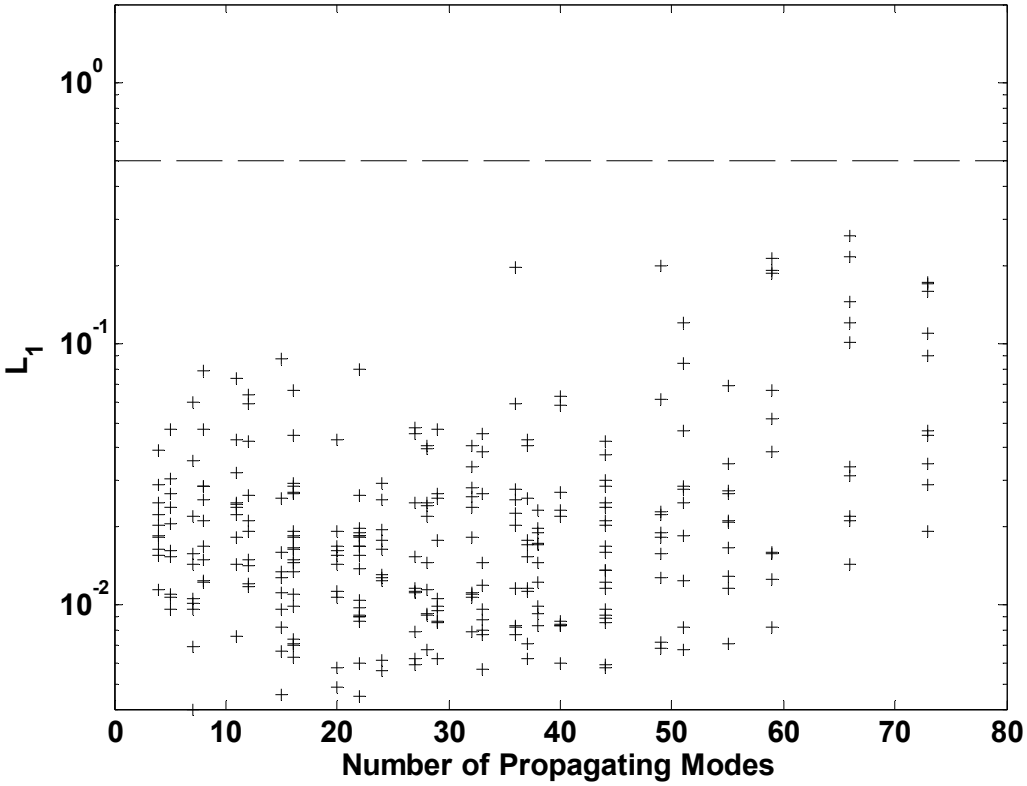

Figure 4.20. L_1 values for polynomial chaos when Q is chosen iteratively based on a maximum threshold for β. The sound speed uncertainty is 10 m/s. The dashed line corresponds to an L_1 value of 0.5.

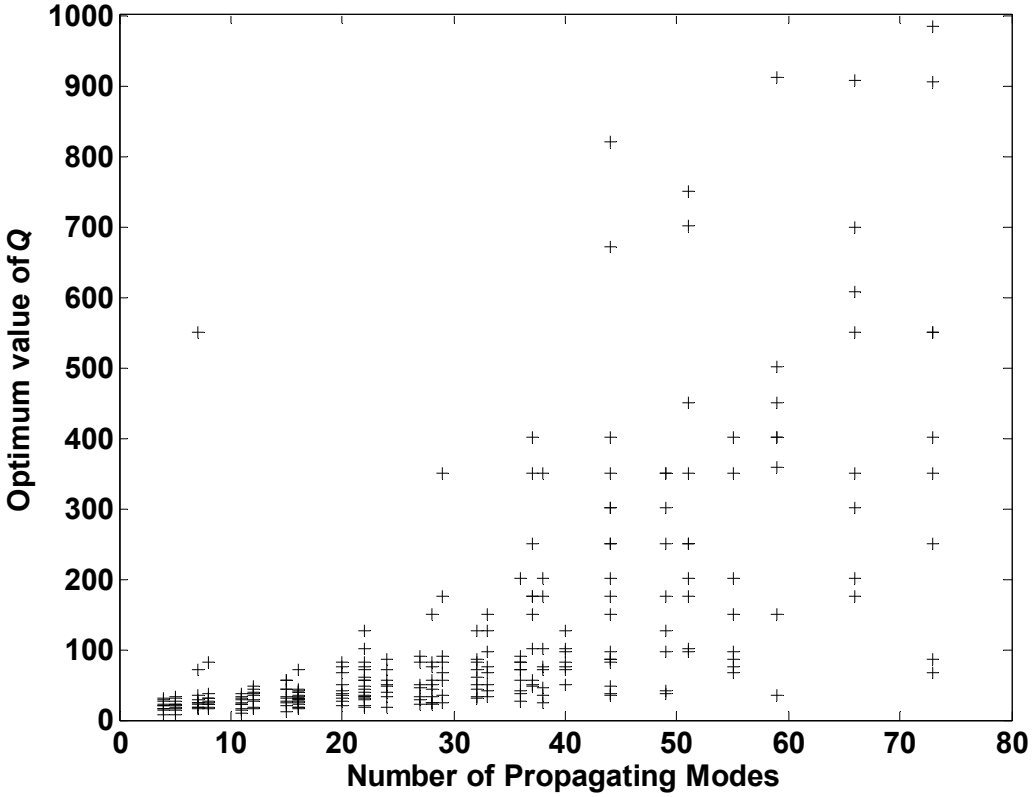

Figure 4.21. Optimum values for Q corresponding to the approximations in Figure 4.20.

Figure 4.22 shows the L_1 values for polynomial chaos with iteratively-selected Q vs. the L_1 values for field shifting, for the case of 10 m/s sound speed uncertainty. The polynomial chaos approximation is more accurate than field shifting for 97% of the cases shown, but each approximation requires a minimum of Q field calculations (with the values of Q shown in Figure 4.21), in contrast to the two field calculations for field shifting. In practice, iteratively determining Q may require up to $Q(Q + 1)/2$ field calculations.

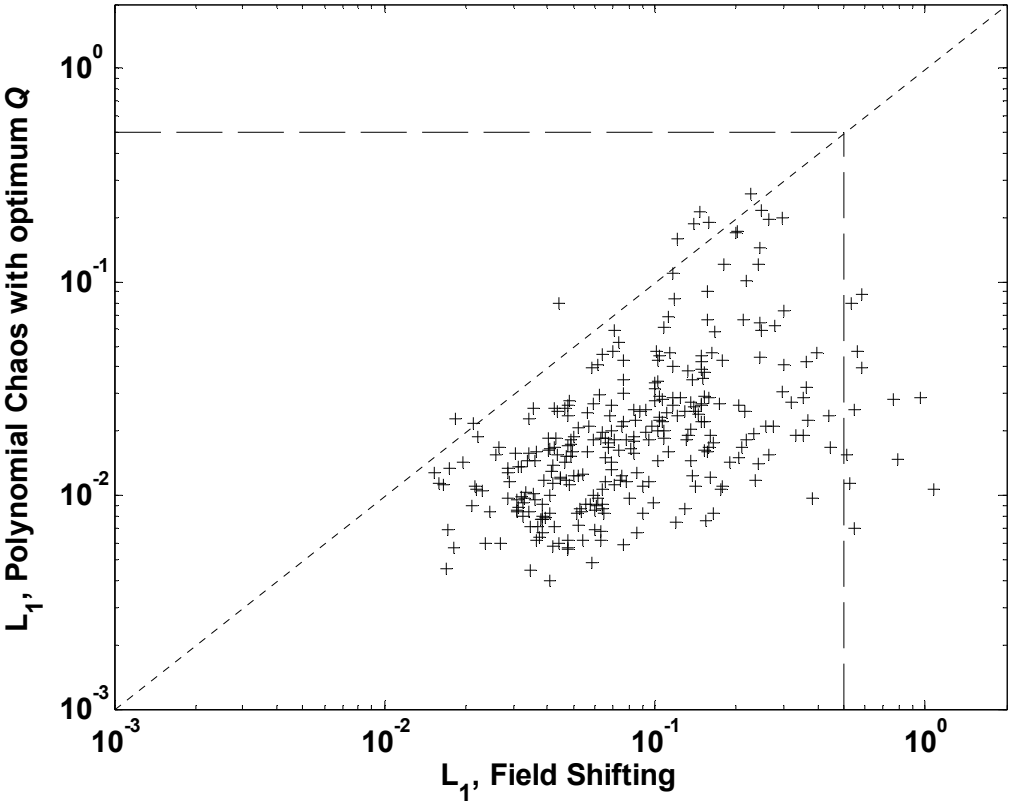

Figure 4.22. L_1 error of polynomial chaos vs. L_1 error of field shifting, when Q is selected iteratively. The sound speed uncertainty is 10 m/s. The dashed lines correspond to an L_1 of 0.5 for each technique. The dotted line indicates equal accuracy of the two techniques.

As seen in the figures above, when Q is chosen appropriately, the polynomial chaos approximation yields more accurate approximations than the field shifting technique in most cases. For fixed, low values of Q, however, the accuracy of individual approximations decreases dramatically, and the field shifting approximation becomes more accurate.

For the uncertainty problem outlined above, part of the computational effort of each technique consists of a certain number of wavenumber calculations (solutions to the transcendental equation 2), and a certain number of modal sums. In general, the computation of wavenumbers and mode shapes is the most expensive part of a modal solution, though in this idealized sound channel it can be performed relatively quickly. As discussed in section II, the direct simulation technique requires N_{DS} complete field calculations, where N_{DS}=101 in the reference results above, though significantly lower N_{DS} may provide acceptable approximations for many applications, as seen in the results in Figures 4.8-4.10 for N_{DS}=21.

For the field shifting technique, the modal wavenumbers and modes are only determined for 2 discrete values of sound speed. Thus, the most expensive part of the field calculation must only be performed twice, in contrast to N_{DS} times in the direct simulation solution. The additional computational effort of field shifting consists of performing modal sums for a grid of points in the region of interest, calculating the RMS error of each possible shift, and performing the final modal sum at each shifted field location.

For the polynomial chaos technique, it was shown that the calculation of each λ_l is equivalent performing a deterministic solution at $k_1 = \sqrt{\lambda_l}$. Thus, for a fixed truncation

order Q, the polynomial chaos technique involves Q complete field calculations. The additional computational effort of polynomial chaos consists of an eigenvalue computation for the tridiagonal coupling matrix of order Q, and a single sum of the Q uncertainty coefficients multiplied by the scaled Hermite polynomials. As discussed in section IV, this assumes an appropriate value for Q is known. If a sufficiently accurate choice of Q must be determined through iteration, the number of field calculations required increases by the same amount.

VI. Conclusions

It has been shown that both the field shifting and polynomial chaos expansion techniques for approximating acoustic uncertainty can be applied to the full-wave solution of the Pekeris waveguide, for the case of uncertain sound speed in the water column. Both of these techniques can be extended to cases of multiple uncertain variables (James and Dowling, 2008 and Finette, 2006), but it is important to note that conclusions drawn from the above results are limited to the case of a single uncertain sound speed.

The field shifting technique is seen to be acceptably accurate for many applications when its primary assumptions hold true in the sound channel of interest. Namely, that changes in the uncertain input approximately correspond to spatial shifts in the field, and that these spatial shifts are linear with respect to the uncertain input. The validity of the first assumption can be measured by the RMS value of the optimum spatial shift. The second assumption is found to be acceptably accurate in this sound channel, as 95% of the L_1 values of these cases fall below 0.3 in the results above. Cases with higher

values of L_1 correspond to a low number of propagating modes, or a high error in the RMS shift. A further advantage of field shifting is the small number of field calculations required to obtain an approximation – only 2 for the case of a single uncertain variable, and 1 additional field calculation for each additional uncertain variable of interest. As shown in Figure 4.14, direct simulation can require up to 21 field calculations to obtain similar accuracy for the environments and sound speed uncertainties examined. As discussed in Chapter 3, this number increases exponentially for each uncertain variable added.

The polynomial chaos technique can provide an extremely accurate approximation for the amplitude distribution, if the truncation order Q is chosen appropriately. There is a direct correspondence between the quantity β defined in equation 19 and the accuracy of the resulting distribution. For the 10 m/s uncertainty cases in Figure 4.20 where Q was chosen such that β was less than $3\text{x}10^{-3}$, 95% of the L_1 values fell below 0.09. For the case of a single uncertain variable, however, this comes at a relatively high computational cost. Polynomial chaos requires a minimum of Q field calculations, where Q is often considerably higher than the number of direct simulation calculations required to obtain comparable accuracy. The fact that Q must either be optimized by some form of iteration, or set acceptably high such that β is acceptable for all receiver locations and parameter values of interest, implies that in practice the number of field calculations required is much higher than this optimum value of Q. However, as stated above, the required number of field calculations for a direct simulation result of specified accuracy grows exponentially with the number of additional uncertain variables, while the required truncation order Q may not. Thus, polynomial chaos is

likely most useful as an efficient alternative to direct simulation for cases of more than one uncertain variable.

Chapter 5

Summary and Conclusions

I. Summary

This thesis research presented here addresses the problem of predicting the uncertainty in acoustic field calculations that arises from uncertainty in environmental parameters. In Chapter 1, established techniques for deterministic field prediction were discussed, as well as related research in the areas of randomness in acoustic fields, and prediction of uncertainty for specific acoustic decision aids.

Chapter 1 also introduced the existing standard for acoustic uncertainty calculation, direct simulation. This technique requires calculation of the field at many possible values of all uncertain inputs, and its computational expense is prohibitive for use in real-time applications. The goal of this thesis research was to explore and develop alternative techniques for uncertainty prediction which provide acceptable accuracy at drastically reduced computational cost.

Chapter 2 provided a derivation of governing equations for the propagation of probability distributions for an acoustic field. The published paper illustrates that boundary value problems can be formulated for field PDFs that can be explicitly solved

for acoustic wave propagation in a one-dimensional case. Unfortunately, solution of these boundary value problems for two-dimensional waveguide propagation requires models for conditional expectations, which do not presently exist for general cases.

Chapter 3 introduces a new alternative technique for predicting approximate probability distributions for an acoustic field, based on the assumption that small changes in environmental inputs correspond to local spatial shifts of the acoustic field.. This field shifting approximation was applied successfully – individually and simultaneously – to all eight environmental parameters specifying a range-independent sound channel with a depth-dependent sound speed profile and a fluid bottom.

Chapter 4 provides an extension of the polynomial chaos expansion work done by other researchers (Creamer, 2005 and Finette, 2006) and several detailed comparisons of DS, FS, and PCE for a single uncertain variable, water column sound speed, in a Pekeris waveguide. Here the PCE technique was modified to predict probability distributions for the field in a Pekeris waveguide, and the PCE wave propagation model was extended from the narrow-angle parabolic-approximation equation to the Helmholtz equation. The comparisons presented involved both accuracy and computational efficiency when the PCE technique was applied with both a fixed and an optimized truncation order.

II. Conclusions

The following conclusions can be drawn from the results of this research:

1. Direct Simulation is highly accurate, but computationally expensive

As discussed in Chapter 1, section V, and illustrated by Figures 4.8-4.10, direct simulation can provide an arbitrarily accurate picture of the probability in an uncertain acoustic field by increasing the number of field calculations, N_{DS}. The required number of field calculations to achieve a specified level of accuracy in environmental sensitivity calculations grows exponentially with the number of uncertain environmental inputs, making this technique's computational cost prohibitive for real-time applications. This limitation establishes the need for faster approximation techniques for acoustic uncertainty prediction. While this conclusion is supported by the results of this research, it is not unique to this thesis. The high accuracy and high computational cost of direct simulation are supported by existing research in underwater acoustics, such as Shorey et al. (1994) and Gerstoft and Mecklenbräuker (1998).

2. Boundary value problems can be written explicitly for the propagation of probability distributions.

Equation 25 in Chapter 2 provides a general evolution equation for pressure PDFs in two or more dimensions, analogous to the Helmholtz equation for deterministic pressure. With the boundary conditions set by the uncertainties in all environmental

parameters, this represents a boundary value problem for the uncertain distribution of acoustic pressure in a sound channel.

3. Closure models for conditional expectations are required to obtain solutions to the governing equations for pressure distributions.

As described on Chapter 2, section V, the governing equation for the propagation of probability in an acoustic field (Equation 25) contains terms that cannot be evaluated without exact or approximate knowledge of the relationship between pressure derivatives and uncertain parameters in the sound channel. Such relationships do not exist for realistic sound channels, thus further modeling would be required to obtain approximate solutions to these governing equations in non-trivial cases.

4. Field shifting is an accurate approximation technique in sound channels for which its assumptions are valid.

Figure 3.8 in Chapter 3 illustrates the relationship between the accuracy of the field shifting approximation for uncertain channel depth (measured by its L_1 value), and the validity of the local-shift assumption (measured by the RMS error of the optimum spatial shift). For this sound channel and uncertain parameter, when the RMS error of the shift is below 0.25, 95% of the field shifting approximations exhibited an L_1 value of less than 0.5, indicating acceptable accuracy for many applications.

5. Field shifting is computationally efficient compared to direct simulation techniques.

As discussed in Chapter 3, section II, when there are N uncertain parameters in a sound channel, field shifting requires $N + 1$ field calculations. Figure 3.12 in Chapter 3 illustrates distributions obtained from both field shifting and direct simulation for a case with 8 uncertain parameters. The solid direct simulation curve required 10^6 field calculations and Monte Carlo sampling, while the dashed field shifting curve required only 9. The tradeoff in accuracy for field shifting in this case is an L_1 error of only 0.12, which is proposed as acceptable for all envisioned applications of this research.

6. Polynomial chaos expansion provides highly accurate approximations for the case of uncertain sound speed in a Pekeris waveguide, when the truncation order is chosen appropriately.

As shown in Figure 4.20 in Chapter 4, the polynomial chaos expansion approximation yields L_1 values below 0.09 for 95% of the cases presented, when the truncation order Q is chosen according to the technique described in section V. Such L_1 values are proposed to represent a very high degree of accuracy acceptable for envisioned applications.

7. Polynomial chaos expansion has a relatively high computational cost in comparison to field shifting in a Pekeris waveguide with uncertain sound speed.

As discussed in section V of Chapter 4, appropriate values for the truncation order Q must be determined iteratively, or set sufficiently high based on knowledge of the sound channel. As a polynomial chaos expansion of order Q is directly analogous in computational effort to N_{DS} direct simulation calculations, the computational cost of the

polynomial chaos method is significantly higher than field shifting for the cases presented.

III. Future Work

This thesis research has introduced two new techniques for uncertainty approximation in acoustic field prediction: PDF propagation and field shifting. In addition, a third, existing approximation technique, polynomial chaos expansion, has been applied to the problem of a Pekeris waveguide and compared to both field shifting and direct simulation. Further research in all three of these methods may broaden the scope of their potential applications, as well as increase their accuracy and/or efficiency.

As discussed in Chapter 2, the PDF propagation technique yields boundary value problems for acoustic uncertainty which cannot be solved without further modeling of the terms containing conditional expectations. Further research in this area may yield approximate models for these conditional expectations for specific uncertainty problems, which would allow for the calculation of acoustic field uncertainty distributions from a given set of environmental parameter uncertainties. In addition, the theory behind the PDF propagation technique is not limited to underwater acoustic propagation. The same concepts may be applied to other forms of wave propagation, such as electromagnetics, for which the resulting conditional expectations may have tractable approximate models.

The field shifting technique introduced in Chapter 3 relies on two fundamental assumptions about the dependence of acoustic pressure on uncertain parameters: that small changes in an environment parameter correspond to spatial translation of the local field, and that such translations evolve linearly with changes in the environmental

parameter. In the most general case, the evolution of the acoustic field arising from variation in an environmental input can be described by a transformation matrix. For the simple field shifting technique introduced in Chapter 3, this transformation matrix is assumed to be a translation, but more generic transformations could also be applied. In addition, the evolution of this transformation matrix for arbitrary changes in the environmental input may be nonlinear. By assuming the evolution to be linear, the field shifting technique requires only two field calculations to fit the linear curve. By performing more field calculations, a nonlinear evolution of the transformation matrix could be approximated. Thus, the field shifting technique introduced in this thesis is a simplification of a more general concept better described as "field transformation." As shown by the results in Chapters 3 and 4, these assumptions of translation and linearity yield acceptably accurate approximations for many cases, at the minimum computational cost for the technique. However, application of these concepts to generic transformation matrices and nonlinear evolution may yield more accurate uncertainty approximations for some applications. Whether the increase in accuracy is high enough to justify the greater computational cost is a topic for further research.

Finally, the polynomial chaos expansion technique was applied in chapter 4 to an idealized sound channel with only one uncertain parameter. Further research in polynomial chaos expansion may apply the technique to more realistic sound channels, and more uncertain parameters. The conclusions drawn in Chapter 4 apply only to the implementation of this technique in the Pekeris waveguide with uncertain sound speed. While the application of polynomial chaos expansion to underwater acoustic prediction is a relatively new field of research, polynomial chaos research in other engineering fields

(Field, 2004) indicates that the efficiency of polynomial chaos compared to direct simulation may increase significantly in more complicated sound channels with more uncertain parameters.

References

Brekhovskikh, L.M., and Lysanov, Yu.P. (1991) *Fundamentals of Ocean Acoustics, 2nd Ed.* (Springer-Verlag, Berlin).

Brown, W.P Jr. (1972). "Moment equations for waves propagated in random media," Journal of the Optical Society of America 62. 45-54.

Buckingham, M.J., and Giddens, E.M. (2006), "On the acoustic field in a Pekeris waveguide with attenuation in the bottom half-space," J. Acoust. Soc. Am. 119, 123-142.

Colosi, J. A. and ATOC Group (1999). "A review of recent results on ocean acoustic wave propagation in random media: Basin scales," IEEE J. Oceanic Eng. 24, 138-155.

Creamer, D. B. (2006). "On using polynomial chaos for modeling uncertainty in acoustic propagation," J. Acoust. Soc. Am. 119, 1979-1994.

D'Spain, G. L. and Kuperman, W.A. (1999a) "Application of the waveguide invariants to analysis of spectrograms from shallow water environments that vary in range and azimuth," J. Acoust. Soc. Am. 106, 2454–2468.

D'Spain, G. L., Murray, J.J., Hodgkiss, W.S., Booth, N.O., and Schey, P.W. (1999b) "Mirages in shallow water matched field processing," J. Acoust. Soc. Am. 105, 3245–3265.

Dopazo, C. (1994) "Recent developments in PDF methods," in *Turbulent Reacting Flows*, Edited by P.A. Libby and F.A. Williams, (Academic Press, London), Ch. 7, pages 375-474.

Dosso, S. E. (2003). "Environmental uncertainty in ocean acoustic source localization," Inverse Problems 19, 419-431.

Dosso, S. E., Giles, P. M., Brooke, G. H., McCammon, D. F., Pecknold, S., and Hines, P. C. (2007a). "Linear and nonlinear measures of ocean acoustic environmental sensitivity," J. Acoust. Soc. Am. 121, 42-45.

Dosso, S.E., Morley, M.G., Giles, P.M., Brooke, G.H., McCammon, D.F., Pecknold, S., and Hines, P.C. (2007b) "Spatial field shifts in ocean acoustic environmental sensitivity analysis," J. Acoust. Soc. Am. Vol. 122, 2560-2570.

Field, R. V., and Grigoriu, M. (2004). "On the accuracy of the polynomial chaos approximation," Probab. Eng. Mech. 19, 65–80.

Finette, S. (2005). "Embedding uncertainty into ocean acoustic propagation models," J. Acoust. Soc. Am. 117, 997–1000.

Finette, S. (2006). “A stochastic representation of environmental uncertainty and its coupling to acoustic wave propagation in ocean waveguides,” J. Acoust. Soc. Am. 120, 2567-2579.

Flatté, S. M. (1983). “Wave propagation through random media: contributions from oceanic acoustics,” Proc. IEEE 71, 1267-1294.

Gerstoft, P., Mecklenbräuker , C. F. (1998). “Ocean acoustic inversion with estimation of a posteriori probability distributions,” J. Acoust. Soc. Am. 104, 808-819.

Gerstoft. P., Huang, C.-F., and Hodgkiss, W.S. (2006) “Estimation of transmisson loss in the presence of geoacoustic inversion uncertainty,” IEEE J. Ocean. Eng. Vol. 31, 299-307.

Haralabus, G., Premus, V., et. al. (1993). “Source localization in an uncertain acoustic scattering environment,” J. Acoust. Soc. Am. 94, 3379-3386.

Heaney, K. D., and Cox, H. (2006). “A tactical approach to environmental uncertainty and sensitivity,” IEEE J. Ocean. Eng. 31, 356–367.

Ishimaru, A. (1978). *Wave propagation and scattering in random media*, Vol II (Academic press, San Diego), Chap. 20.

James, K.R., and Dowling, D.R. 2005 “A probability density function method for acoustic field uncertainty analysis,” J. Acoust. Soc. Am. Vol. 118, 2802-2810.

James, K.R., and Dowling, D.R. 2008 “A method for approximating acoustic-field-amplitude uncertainty caused by environmental uncertainties,” J. Acoust. Soc. Am. Vol. 124, 1465-1476.

James, S., Zhu, J., and Anand, M.S. (2005) “Lagrangian PDF transport method for simulations of axisymmetric turbulent reacting flows,” AIAA Paper No. 2005-156.

Jensen, F., Kuperman, W., Porter, M., Schmidt, H. (1994). *Computational Ocean Acoustics*, (AIP Press, New York).

Kallistratova, M. A. (2002). “Acoustic waves in the turbulent atmosphere: A review,” J. Atmospheric and Oceanic Tech. 19, 1139-1150.

Kim, S., Kuperman, W.A., Hodgkiss, W.S., Song, H.C., Edelmann, G.F., and Akal, T. (2003) “Robust time reversal focusing in the ocean,” J. Acoust. Soc. Am. Vol. 114, 145-157.

Kinsler, L.E., Frey, A.R., Coppens, A.B., Sanders, J.V. (2000). *Fundamentals of Acoustics, 4th Ed.* (Wiley & Sons, New York), p. 261.

LePage, K. D., and McDonald, B. E. (2006). "Environmental effects of waveguide uncertainty on coherent aspects of propagation, scattering, and reverberation," IEEE J. Ocean. Eng. 31, 413–420.

Lin, Y.-T., Chen, C.-F., Lynch, J. F. (2006). "An equivalent transform method for evaluating the effect of water-column mismatch on geoacoustic inversion," IEEE J. Ocean. Eng. 31, 284-298.

Livingston. E.S., Goff, J.A., Finette, S., Abbot, P., Lynch, J.F. Hodgkiss, W.S. (2006) "Guest editorial capturing Uncertainty in the tactical ocean environment," IEEE J. Ocean. Eng. Vol. 31, 245-248.

Lou, H., and Miller, R.S. (2001) "On the scalar probability density function transport equation for binary mixing in isotropic turbulence at supercritical pressure," Physics of Fluids, Vol. 13, 3386-3399.

Lundgren, T.S. (1967) "Distribution functions in the statistical theory of turbulence," Phys. of Fluids, Vol. 10, 969-975.

Minier, J.P., and Peirano, E. (2001). "The pdf approach to turbulent polydispersed two-phase flows," Physics Report 352, 1–214.

Papoulis, A. (1965) *Probability, Random Variables, and Stochastic Processes* (McGraw Hill, New York), Ch. 5.

Pope, S. B. (2000) *Turbulent Flows* (Cambridge University Press, Cambridge, UK). Ch. 12, Appendix H.

Pope, S.B. (2004) "Advances in PDF methods for turbulent reacting flows," Proceedings of the 10th Conference on Turbulence, Paper No. 801, pages 1-8.

Porter, M., and Reiss, E.L. (1984) "A numerical method for ocean-acoustic normal modes," J. Acoust. Soc. Am. Vol. 76, 244-252.

Sha, L. and Nolte, L.W. (2005a) "Effects of environmental uncertainties on sonar detection performance prediction," J. Acoust. Soc. Am. Vol. 117, 1942-1953.

Sha, L. and Nolte, L.W. (2005b) "Bayesian sonar detection performance prediction in the presence of interference in uncertain environments," J. Acoust. Soc. Am. Vol. 117, 1954-1964.

Shang, E. C., and Wang, Y. Y. (1991). "Environmental mismatch effects on source localization processing in mode space," J. Acoust. Soc. Am. 89, 2285–2290.

Shorey, J.A., Nolte L. W., Krolic, J. L. (1994). "Computationally efficient Monte Carlo estimation algorithms for matched field processing in uncertain ocean environments," J. Comp. Acoust. 2, 285-314.

Sibul, L. H., Coviello, C. M., and Roan, M. J. (2004). "Detection of high frequency sources in random/uncertain media," in *High Frequency Ocean Acoustics*, edited by M. B. Porter, M. Siderious, and W. A. Kuperman (Am. Inst. Phys., Melville, NY), pp. 237–244.

Stone, L., and Osborne, B. (2004). "Effect of environmental prediction uncertainty on target detection and tracking," Proceedings of SPIE 5428, 58-69.

Tsai, K., Gillis, P. A., Sen, S., Fox, R. O. (2002). "A finite-mode PDF model for turbulent reacting flows," Transactions of the ASME. Journal of Fluids Engineering 124, 102-107.

Uscinski, B.J. (1977) *The elements of wave propagation in random media* (McGraw Hill, New York)

Waclawczyk, M., Pozorski, J., and Minier, J.-P. (2004) "Probability density function computation of turbulent flows with a new near-wall model," Physics of Fluids, Vol. 16, 1410-1422.

Wang, H., Yip, L., Yao K., Estrain, D. (2004). "Lower bounds of localization uncertainty in sensor networks," IEEE ICASSP.

Wang, L., Haworth, D. C., and Modest, M. F. (2005). "A PDF/photon Monte Carlo method for radiative heat transfer in turbulent flames," Proceedings of the ASME Summer Heat Transfer Conference, 741-745.

Witteveen, J. and Hester, B. (2008). "Efficient quantification of the effect of uncertainties in advection-diffusion problems using polynomial chaos," Numerical Heat Transfer, Part B: Fundamentals, v 53, n 5, p 437-465.

Xiu, D. and Karniadakis, G. (2002a) "The Wiener-Askey polynomial chaos for stochastic differential equations," SIAM J. Sci. Comput. USA 25, 619–644.

Xiu, D., Lucor, D., Su, C.H., and Karniadakis, G. (2002b). "Stochastic modeling of flow structure interactions using generalized polynomial chaos," ASME Trans. J. Fluids Eng. 124, 51–79.

Zhang, Z.Y., and Tindle, C.T. (1992). "Complex effective depth of the ocean bottom," J. Acoust. Soc. Am. Vol. 93, 205-213.